AN ABSTRACT OF THE THESIS OF

Nathaniel Granger Plant for the degree of Doctor of Philosophy in Oceanography presented on 17 April 1998.

Title: The Role of Morphologic Feedback in Surf Zone Sand Bar Response.

Redacted for privacy

Abstract approved: _____

Robert A. Holman

This study showed that, in spite of annual and intra-annual forcing, interannual frequencies explained over 70% of the temporal morphologic variability observed at a beach near Duck, NC. Dominant interannual variability is not consistent with most existing conceptual models, which predict morphologic response at the same time scale as the forcing. Forcing and response at the same time scale is hypothesized to result from a feedback mechanism which drives nearshore morphology toward an equilibrium state. This thesis evaluated this hypothesis and its application to prediction of the migration, growth, and decay of surf zone sand bars. The role that morphologic feedback played in governing sand bar response was described, focusing on the alongshore-uniform component of the nearshore morphology (i.e., cross-shore profiles), extracted from monthly bathymetric surveys. The alongshore-uniform component explained between 50 and 90% of the temporal variability of the surveyed bathymetry.

A model was formulated to predict changes in sand bar crest position. The model assumed that sand bars migrated toward a wave height dependent equilibrium position. Interannual variability was predicted to result from transient response if the bar response

time was long relative to the time scale of the forcing. Dependence of the bar response time on wave height enhanced the transient response, driving bars formed near the shore toward the outer extent of the surf zone. The model did not incorporate a mechanism for introducing transients. The model predictions of changes in bar crest positions were consistent with observations. The estimated equilibrium position suggested that bars migrated toward a break point. The response time, determined empirically, increased inversely with the wave height cubed.

Sediment transport patterns associated with bar migration and growth were estimated by modeling the observed, alongshore-averaged profiles with a simple morphologic model consisting of a plane beach and Gaussian-shaped bars. Sediment transport patterns responsible for changes in bar position and amplitude were related to hydrodynamic conditions at bar crests. The ratio of wave height to water depth at the bar crest (γ_{crest}) parameterized the hydrodynamic conditions. A value of γ_{crest} corresponding to the onset of wave breaking divided conditions associated with onshore migration from offshore migration. Bar migration tended to drive γ_{crest} toward the value associated with the onset of wave breaking, again suggesting an equilibrium bar position corresponding to a break point. Surprisingly, when the bar migration direction changed from onshore to offshore, the spatial variability of sediment transport over a bar length increased monotonically as γ_{crest} increased. Thus, the feedback mechanism associated with the observed bar response differed from the hypothesized mechanism, which was expected to drive transport to zero at equilibrium.

The Role of Morphologic Feedback in Surf Zone Sand Bar Response

by

Nathaniel Granger Plant

A Thesis

submitted to

Oregon State University

in partial fulfillment of
the requirements for the
degree of

Doctor of Philosophy

Completed 17 April 1998
Commencement June 1998

Doctor of Philosophy Thesis of Nathaniel Granger Plant presented on 17 April 1998

APPROVED:

Redacted for privacy

Major Professor, representing Oceanography

Redacted for privacy

Dean of College of Oceanic and Atmospheric Sciences

Redacted for privacy

Dean of Graduate School

I understand that my thesis will become part of the permanent collection of Oregon State University libraries. My signature below authorizes release of my thesis to any reader upon request.

Redacted for privacy

Nathaniel Granger Plant, Author

ACKNOWLEDGMENT

I have been inspired by many people here in Corvallis, some of whom were not even born when Sheila and I arrived. Through, the words and thoughts and actions of these friends, I learned to see many parts of the world that were invisible to me. Sheila taught more than anyone else, showing me how to see my future and embrace it. From the days before Corvallis to the final moments spent preparing this thesis (the final moments lasted 4 months), she encouraged my pursuit of oceanography. She added other flavors to my general education, including children, giving me much needed perspective on my work. This helped answer the occasional "Why am I doing this?", and pointed out that there were many things to do in the world. Thank you Sheila for being my best friend and for sharing so much fun with me.

The course that I have followed to become a nearshore geologist and oceanographer has been guided by a number of gurus. The first that I encountered was Gary Griggs, who taught "Coastal Geology", my first geology class at UCSC. Gary showed me the beach and encouraged me to study it. I started surveying beaches with Jim Tait, who explained things to me (or anyone) simply and clearly. While I was at UCSC, I took several courses from Ed Thornton at the Naval Post Graduate School. I remember feeling totally clueless at times. I learned that I had a lot to learn. It was good medicine; Ed delivered it humanely, and encouraged me to go on. Bruce Jaffe and Katie Scott were there too. They helped me along and convinced me that I was capable of earning a Ph.D. At UCSC, Bob Anderson exposed me to "self organization" and approaches to study it, which I have been trying to fit into my work ever since.

From UCSC I want to the USGS to work with John Dingler and Tom Reiss, where I realized that beaches were a career option. I wanted it. The fire was fueled by many conversations with Bruce Jaffe and Bruce Richmond as we commuted from the land of surf,

often late for work, wet, and salty. They helped me to gain a better understanding of some aspects of nearshore hydrodynamics, which were lost on me in Ed's class.

I remember two things about visiting Rob as a prospective student. First, he asked me to explain how I thought beaches worked. I gave a geological and useless (at that moment) explanation, and he pointed this out to me. Then, he presented this puzzle about a bubble in a bottle and whether it (the bubble) got bigger or smaller as it floated to the top. Sheila and I were in Redding (400 miles south of Corvallis) on our way home before we stopped talking about it. Gurus tend to answer questions with other questions. Rob has done this for me over and over -- some times it is the same question ("What are the conclusions?"). Other times, the questions were clearly "right-brain" products ("What is the temperature of a beach?"). To date, many of the questions have gone unanswered. In this way and in other ways, Rob has shared his wisdom with me generously. I hope that I will be able to do as much for others.

As frequently as I stepped into his office, Mike Freilich added clarity to my work. As I "wasted my time" in Mike's office, he showed me what the problem was that I was working on, which was usually harder to do than solving it. Perhaps most importantly, discussions with Mike (filled with an interesting mixture of philosophy, scientific rigor, humor, and expletives) helped me to define my role as a scientist.

Ron Guenther has given me the ability to comprehend mathematics. This did not come naturally to me, and much of what he taught continues to solidify as I encounter new problems. Before I was even born, Paul Komar wrote some papers on nearshore processes. I am indebted to his efforts to organize a confusing blend of geology and fluid dynamics. Similarly, Tony Bowen built the foundations upon which much of the work presented in this thesis stands. I am thankful for the advice and insight that he offered me, as I struggled to build higher.

The gurus asked tough questions and pointed in several directions at once when I asked them "which way?" My contemporaries went along those paths with me -- some times pushing with a sharp stick. Diane stuck with me the longest, after Todd bailed out (i.e., graduated). She became a close friend to me and Sheila, and, effectively, Aunt Diane to Kathryn. Diane, of course, had the sharpest stick, forcing me to take my exams and finish this thesis. Thanks. Todd took good care of me by offering really sound advice, being well organized, and knowing when to do something nice for Cindy and Sheila. This kept me out of all sorts of trouble. Mark read drafts of my papers and kept me in shape, either hauling rocks up steep cliffs or playing basket ball. I am thankful for the sanity that he and Vicki offered on sailing trips and barbecues. The 16 oz. sanity doses were especially helpful at times. Peter Ruggiero helped me survive Ron Guenther's courses and go surfing. These tasks were both important to my well being and Peter took them seriously. I hope that we can do more of both in the future. Kathelijne helped raise my caffeine tolerance, as we discussed new and interesting ways of thinking about sand bars. I look forward to more caffeine and discussions with her. I am thankful for Hilary and Kathy, who would lure me into new statistics problems just when my projects was seeming totally impossible. This kept me from enduring great frustration and made me feel useful and productive again. Perhaps my first colleague was John Stanley, who taught me how to program in C "elegantly", taught me how video cameras worked, and radio waves, and just about anything else that we plugged in. John deserves much credit for everything that I did using video images since he set up much of the Argus Program, wired things to run in the lab, and kept my files from disappearing. We had fun together in the lab or field, where I was shocked often that I got his jokes based on obscure references. He proved that you can't add too much humor to a Ph.D. program. Carrie Tasman helped many times, either by trapezing, baby sitting, partying, or even formatting a thesis the day before it was done.

My parents and Sheila's parents have been supportive of all that we have done. This has given me great peace of mind, even when things got stressful. I thank them for the

perspective that they shared, and for asking me questions about my work. Tom and Ann showed us the way to balance science careers and family. Josh has remained one of my few long distance friends. He managed to conjure up better-than-mediocre surf whenever he visited, and has done other things to help organize my priorities.

I was supported by the ONR AASSERT program (grant #N0042C) and ONR Coastal Dynamics program (grant #N0014-9610237). ONR, through Tom Kinder, also provided ultimately practical advice on carving a career in oceanography.

Finally, this thesis is dedicated to my children and my colleagues' children, who were born and grew up a bit while I was in graduate school. They have been very understanding, patient, and fun.

CONTRIBUTION OF AUTHORS

Chapters 2-5 have been published or will be submitted for publication. Chapter 2 was reprinted from Marine Geology (vol. 140, Plant, N. G. and R. A. Holman, Intertidal beach profile estimation using video images, pages 1-24, copyright 1997) with permission from Elsevier Science. Holman proposed the technique that was developed in that paper, and guided me through many stages of the development and analysis.

Chapter 3 was published in the proceedings of a conference on coastal engineering (N. G. Plant and R. A. Holman, Interannual shoreline variations at Duck, NC, USA, Proc. of the 25th Int. Conf. Coastal Eng., 3(272), 3521-3533., 1997, reproduced with permission of ASCE). Holman provided critical review of that material.

Chapter 4 and 5 will be submitted as two separate papers to the Journal of Geophysical Research. Rob Holman and Mike Freilich are co-authors on both papers. Both Rob and Mike have provided many critical reviews of the content in these chapters. Rob provided guidance on the scope of each paper, as well helping to drawn important inferences from the analysis results. Mike helped focus each paper on several well defined problems that could actually be addressed using the data that were in hand. In addition, he suggested many useful analysis tools and approaches. Chapter 4 is co-authored by Bill Birkemeier, of the Army Corps of Engineers' Field Research Facility. He is responsible for maintaining the data collection programs from which we have drawn the bathymetric and hydrodynamic data that were analyzed in both Chapter 4 and Chapter 5.

TABLE OF CONTENTS

TABLE OF CONTENTS, CONTINUED

TABLE OF CONTENTS, CONTINUED

LIST OF FIGURES

LIST OF FIGURES, CONTINUED

LIST OF FIGURES, CONTINUED

LIST OF FIGURES, CONTINUED

LIST OF TABLES

THE ROLE OF MORPHOLOGIC FEEDBACK IN SURF ZONE SAND BAR RESPONSE

CHAPTER I: THESIS INTRODUCTION

1. What are sand bars, surf zones, and morphologic feedback?

Much of the motivation for the work presented in this thesis came from video observations of nearshore morphology. On any given day, these observations reveal nearshore morphology having a variety of characteristic length scales. In the alongshore direction, short scale features such as beach cusps having a spacing of 10-50 m attract our attention, since they often result in striking spatial structures (see Chapter 3). These features appear and disappear with days. Over periods of several years to decades, however, changes in the nearshore morphology are dominated both long length and time scales. Much of this variability is alongshore-uniform and in spite of annual and intra-annual forcing, the alongshore-uniform component of morphology exhibits interannual variability. In particular, the movement of shore-parallel sand bars has been shown to be dominated by interannual variations. This seems to be at odds with conceptual models in which it is assumed that the form and position of bars is correlated to wave conditions. This discrepancy suggests that we more carefully analyze the relationship between changing wave conditions and bar response. Before plunging into how this problem is approached, some terminology is defined and explained. Then, a brief description of the particular observations that have motivated this study is presented. Finally, the thesis approach and goals are described, along with an outline of the contents of each chapter.

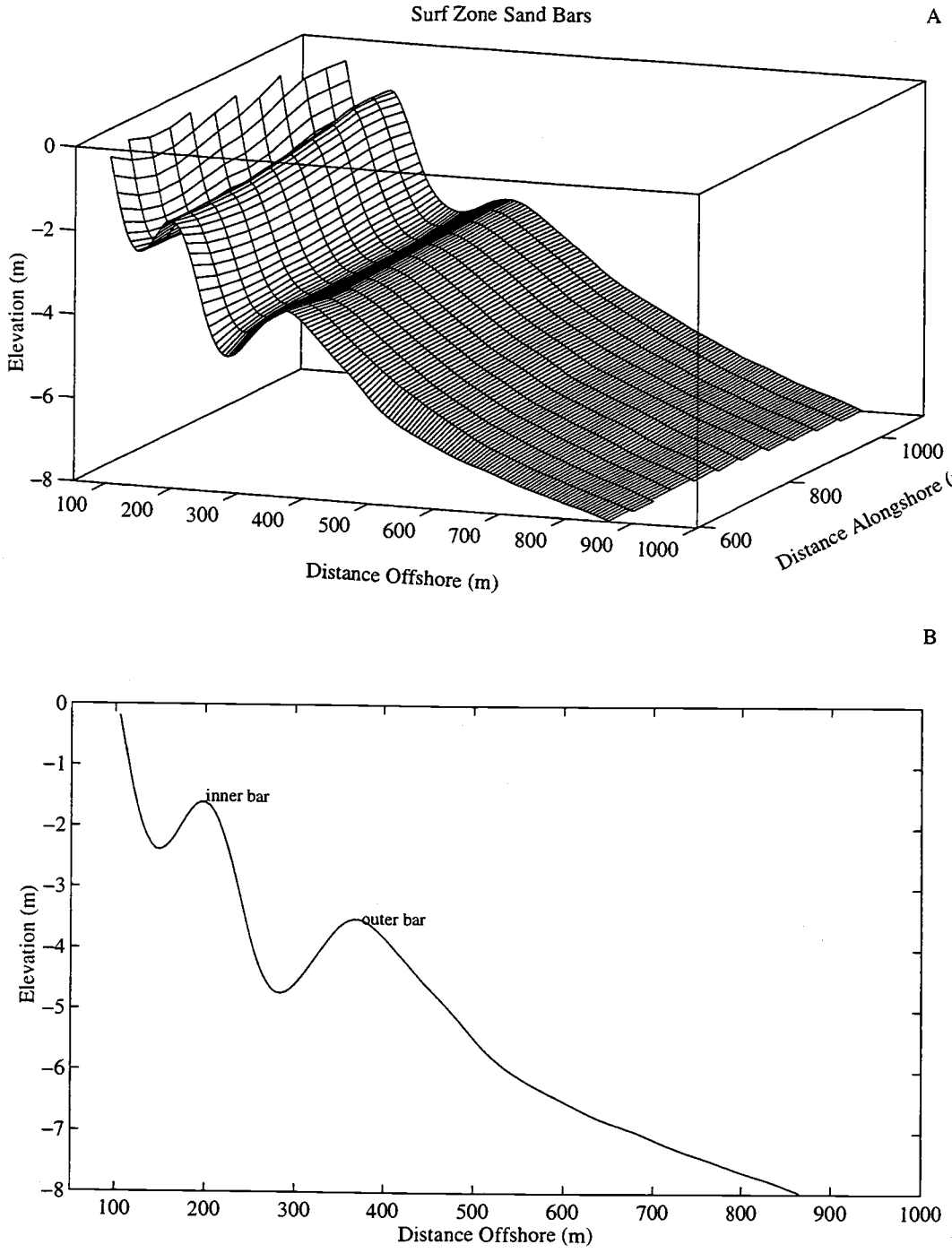

Figure I.1. Mesh-perspective view of typical shore-parallel sand bar bathymetry (A). Inner and outer bar crests are located approximately 200 m and 400 m from the shoreline (B). Bathymetry surveyed at the Army Corps of Engineers' Field Research Facility (FRF), 13 January 1983. Elevation datum is approximately mean sea level (National Geodetic Vertical Datum 1929)

1.1 Definition of a sand bar

In their simplest form, surf zone sand bars are shore parallel, subaqueous sand ridges (Figure I.1). The cross-shore length scale of surf zone sand bars (e.g., distance between a bar crest and the shoreline, or distance between adjacent bar crests on a multi-barred beach) is of order 100 m [*Bowen*, 1980] and the trough-to-crest height is of order 1 m. On beaches with multiple bars, the distance between bars tends to increase with distance offshore [*Bowen*, 1980; *Komar*, 1998]. A common characteristic of surf zone sand bars is their continual evolution, which comprises changes in plan form as well as cross-section. Perhaps most striking is the tendency for the sand bar plan form to oscillate between a relatively simple, shore-parallel structure and more complicated structures having irregular or rhythmic alongshore variability.

1.2 Classification of surf zones

The surf zone comprises the nearshore region between the shoreline and an offshore point where waves begin to break [*Komar*, 1998]. This definition, although based on the behavior of waves, depends on the beach shape. A fundamental description of beach shape is the cross-shore slope. On relatively steep beaches, waves do not break at all. On gently sloping beaches, waves break and drive a variety fluid motions including mean longshore currents and undertow. The "steepness" of a beach can be described by the ratio of the beach slope ($\tan\beta$) to wave steepness (H/L), forming a non-dimensional beach slope parameter (the Iribarren number)

$$\xi = \tan\beta / (2\pi H/g T^2)^{1/2}. \qquad (1)$$

H is a characteristic wave height and T is a characteristic wave period (related to the deep water wind wave length: $L = g T^2/2\pi$). Operationally, $\tan\beta$ is the average surf zone slope.

The Iribarren number defines hydrodynamic regimes ranging from dissipative to reflective. Incident wave energy is strongly dissipated via wave breaking if $\xi<0.25$ and waves are strongly reflected by the beach if $\xi>1$ [*Battjes*, 1974]. Hence, a surf zone exists if $\xi<1$. The surf zone width varies with temporal or spatial changes in both the incident wave conditions and beach slope.

1.3 Morphodynamic classification

Because of the relationship between morphology and hydrodynamics, beach shapes have been classified as belonging to several, broadly defined "morphodynamic" states. This classification approach recognizes observed correlations between ξ and beach plan form or cross-section. The simplest classification system recognized the correlation of barred profiles with dissipative ("storm" or "winter") conditions and the correlation of unbarred profiles with reflective ("calm" or "summer") conditions. Thus, beaches may be associated with one of two beach states, denoted "storm" or "calm" profiles [*Shepard*, 1948; *Komar*, 1998]. The storm-calm classification system was sufficient for organizing a collection of infrequently sampled (e.g., semi-annual) beach profiles [*Shepard*, 1948; *Bascom*, 1954], which were surveyed directly at low tide or quantified via bathymetric soundings. The most rapid fluctuations resolved by semi-annual observations were annual cycles of profile change.

A more sophisticated beach classification scheme was developed by *Short* [1975] and refined and summarized by *Wright and Short* [1984]. This scheme identified both changes in the alongshore structure of beaches (plan form), and the cross-section. Several years of daily, visual, surf zone observations were used to define 6 morphodynamic states (Figure I.2 shows three of them).

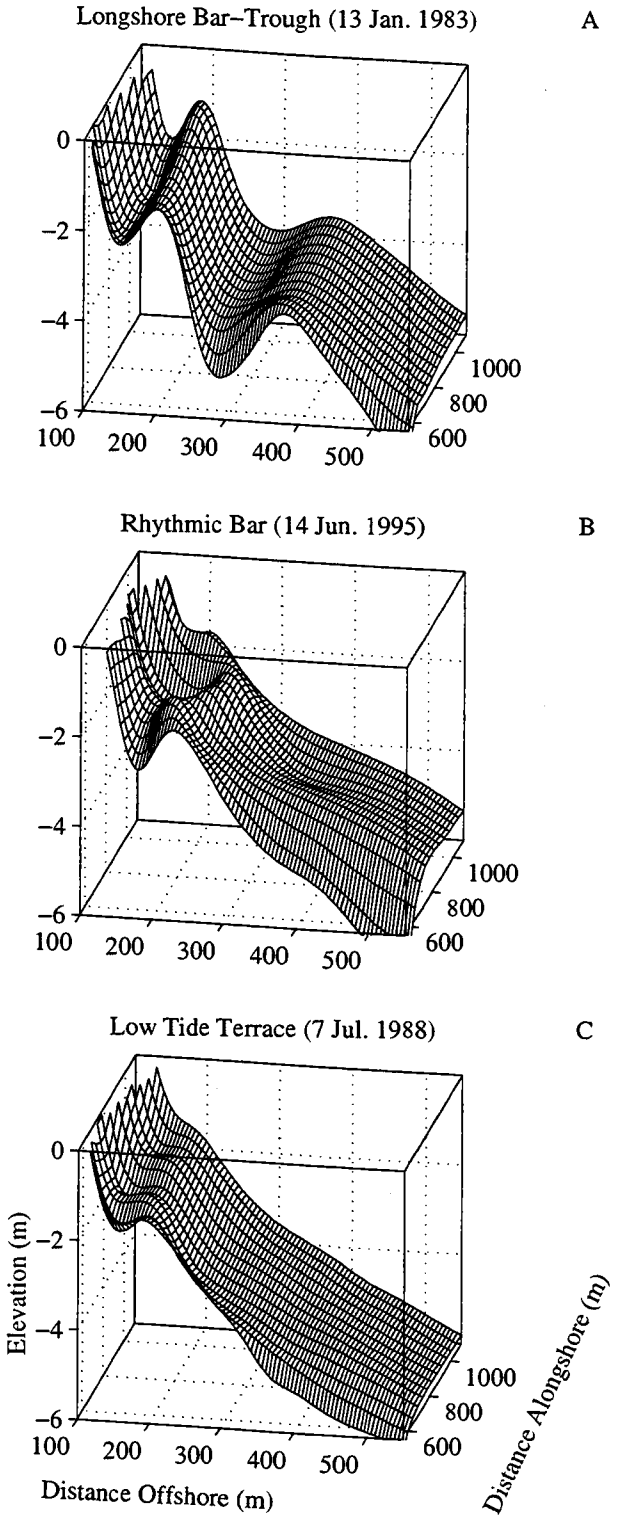

Figure I.2. Examples of barred bathymetry classified within *Wright and Short's* [1984] morphodynamic states. Data surveyed at the FRF. The Longshore Bar-Trough state (A) was the most dissipative state observed at this site. The Low Tide Terrace state (C) was the most reflective.

(S1) Dissipative ($\xi \leq 0.1$, alongshore-uniform, unbarred beach, gently sloping shoreline).

(S2) Longshore bar/trough ($0.1 < \xi \leq 0.25$, alongshore-uniform and barred beach, Figure I.2A).

(S3) Rhythmic bar/beach ($0.25 < \xi \leq 0.5$, alongshore-rhythmic shoreline and bar, Figure I.2B).

(S4) Transverse bar/rip ($0.5 < \xi \leq 0.75$, obliquely oriented, shore-attached bars and channels).

(S5) Low tide terrace ($0.5 < \xi < 1.5$, mostly alongshore-uniform attached bar and narrow channel, Figure I.2C).

(S6) Reflective ($\xi \geq 1.5$, alongshore-uniform, unbarred beach, steeply sloping shoreline).

The names given to the morphodynamic states range from descriptions of the fluid dynamics (e.g., dissipative and reflective) to descriptions of the beach shape alone (e.g., low tide terrace). One of the purposes of the classification system was to relate different fluid processes to different morphologic forms. The Iribarren number range associated with each state indicates an attempt to do this. This classification scheme has been refined further in an attempt to associate the length scales of sand bar patterns with either incident frequency wave motions ($f > 0.05$ s^{-1}) or infragravity wave motions ($f < 0.05$ s^{-1}) [*Lippmann and Holman*, 1990].

1.4 Beach equilibrium and morphologic feedback

A fundamental hypothesis drawn from the morphodynamic classification schemes is that the morphodynamic states represent stable equilibrium states. That is, for steady incident (i.e., offshore of the surfzone) wave conditions, the nearshore morphology and fluid motions may evolve toward a particular morphodynamic state. The implication is that if the incident wave conditions are known, then the evolution of the beach morphology is predictable [*Aubrey, et al.*, 1980; *Wright, et al.*, 1985].

It is plausible that equilibrium morphologic states exist for beaches. Beaches could achieve this equilibrium if competing sediment transport mechanisms balance one another, such that the transport, averaged over many wave periods, vanishes. Using simple formulations for sediment transport beneath waves, *Bowen* [1980] demonstrated that a balance between down slope transport (driven by oscillatory currents and gravity) and the tendency for waves to transport sediment in the up-slope direction could be achieved. Others have employed Bowen's approach to determine equilibrium morphologies (see review by *Bowen and Huntley* [1984]) associated with more complicated fluid motions, for example, infragravity waves [*Holman and Bowen*, 1982] and longshore currents [*Howd, et al.*, 1992].

Morphologic feedback is required to drive beach morphology toward an equilibrium state. The term "morphologic feedback" refers to the coupled morphologic and hydrodynamic evolution of surf zones: (1) Sediment transport depends on fluid motions and bottom slopes. (2) Sediment transport changes the morphology. (3) morphologic changes alter the transport patterns (back to 1). The term "morphologic feedback" emphasizes a perspective that focuses on understanding how the morphology at any time affects morphologic evolution.

For instance, it has been suggested that morphologic feedback drives sand bars toward an equilibrium position that depends on wave height. If a bar is seaward of the equilibrium position, it migrates onshore. If it is too far onshore, it migrates offshore. This is an example of negative feedback, since perturbations about the equilibrium position tend to decay. Other forms of feedback are common in geomorphic systems. For example, ripple bed forms in rivers [*Smith*, 1970; *McLean*, 1990], river meanders [*Nelson*, 1990], large scale, O(1 km), nearshore sand waves [*Hulscher*, 1993] and sand ridges [*Trowbridge*,

1995] can be explained via instability mechanisms where perturbations about an equilibrium state grow and continue to evolve indefinitely. The nature of the feedback mechanisms associated with sand bars has not been well defined. This issue is confounded by the continual change in incident wave conditions.

1.5 Relevant sediment properties

The shape of beaches depends strongly on the constituent sand grains. Beaches with coarse grains tend to be relatively steep, while beaches exposed to the same wave conditions but having finer grains tend to be more gently sloping [*Bascom*, 1954]. This relationship tends to affect geographic variations in ξ, which depends on beach slope. A non-dimensional parameter that describes the effect of grain size on sediment transport processes is the ratio of the wave velocity magnitude (U_{wave}) to the sediment settling velocity (w_s),

$$\Omega = U_{wave}/w_s \sim H/(T\, w_s), \tag{2}$$

where w_s is the settling velocity, and U_{wave} is the wave orbital velocity magnitude. Ω is commonly called the Dean parameter [*Dean*, 1973], and can be used to identify the mode of sediment transport. Transport occurs as bed load if $\Omega<10$ (roughly) and suspended load dominates for $\Omega>15$-20 [*Bowen*, 1980]. Also, sediment transport will be susceptible to unlimited suspension (autosuspension) if $\Omega \tan\beta>1$, resulting in turbidity flows [*Bagnold*, 1963]. Typically, sand bars exist in environments with alternating (temporally and spatially) bed load and suspended load dominance [*Thornton, et al.*, 1995].

2. Motivation

Significant changes in the incident wave height occur with individual storms (time scale of days), or over an annual cycle. Most attempts to predict the evolution of beach morphology have focused on response at these time scales. Recently, however, observations over periods of years to decades indicate that interannual variability may be a significant or even dominant component of beach response [*Birkemeier*, 1985; *Lippmann, et al.*, 1993; *Ruessink and Kroon*, 1994; *Wijnberg and Terwindt*, 1995]. For example, *Ruessink and Kroon* [1994] identified patterns of interannual sand bar variability in annual bathymetric surveys along the Dutch Coast. The surveys were sampled over a 30 year period and had extensive alongshore coverage (spanning many kilometers), but did not resolve the scale of alongshore variability typically considered relevant to morphodynamic classification: O(100 m). Perhaps fortuitously, the profile response was coherent across many alongshore sample locations. The observed sand bar behavior consisted of bar formation near the shoreline, subsequent seaward migration, followed by eventual bar decay in the outer region of the surfzone. Individual bars completed a bar cycle (formation to decay) in approximately 15 years. The net seaward migration of bars occurred without net offshore sediment transport (sediment was conserved). The cross-shore profile typically contained 3 bars, and an inner bar formed only after an outer bar decayed (the number of bars was conserved).

An analysis of the bathymetric variability along the entire Dutch Coast [*Wijnberg and Terwindt*, 1995] showed that interannual, cyclic bar behavior was typical. Bar cycle duration, however, varied across abrupt geographic boundaries. These boundaries coincided with jetties, which, surprisingly, did not divide the coast into regions with different morphodynamic properties. These observations suggest that, under some conditions, morphology and morphologic changes are uncorrelated to changes in the hydrodynamic

regime. To date, predictive morphodynamic models are based on observed correlations between changes in morphologic state and changes in wave conditions. This correlation is assumed to result because the morphologic state strives towards equilibrium that depends on wave conditions. In light of the observed dominance of interannual morphologic response at some locations, this assumptions needs to be re-evaluated.

3. Thesis goals and approach

The goals of this thesis are to (1) quantify the relative importance of interannual and intra-annual sand bar variations at a particular field site, (2) evaluate the assumption that morphologic feedback associated with sand bar response is negative, driving bars toward an equilibrium state, and (3) suggest processes and feedback mechanisms that are responsible for observed sand bar response. These goals are achieved through analysis of bathymetric changes observed at the FRF site, near Duck, NC, USA.

The approach used in this thesis is to describe observed bathymetric variability with a small number of parameters. Then, temporal changes in these parameters are related to simple parameterizations of the wave conditions and to the morphologic parameters themselves, exposing some aspects of morphologic feedback. The advantage of this approach is that morphologic feedback is described explicitly. A disadvantage of this approach is that the role played by specific processes is not evaluated directly. This approach does, however, point to different suites of processes, whose relative importance is interpreted using the hydrodynamic parameterizations.

4. Outline

The thesis is divided into 5 chapters, in addition to this introduction. In Chapter 2, ***Intertidal beach profile estimation using video images***, a remote sensing tool is developed to quantify nearshore morphology. In Chapter 3, ***Interannual shoreline variations at Duck, NC, USA***, the technique developed in Chapter 2 is used to quantify the spatial and temporal scales of morphologic variability near the shoreline. The observed evolution of coherent shoreline patterns is related to variations in the incident wave conditions. In Chapter 4, ***Observations of long-term sandbar behavior at Duck: how relevant is equilibrium thinking?***, quantifies the spatial and temporal variability captured in a 16-year time series of conventional bathymetric surveys. Sand bars are identified in this time series and observed bar migration is compared to a simple, 2-parameter model. The model includes a mechanism for generating interannual variability consistent with observations. The model assumptions are evaluated. In Chapter 5, ***The role of morphologic feedback in surf zone sand bar response***, a more sophisticated morphologic model is used, which allows an examination of the sediment transport patterns responsible for sand bar response. This model exposes the relationship between morphology and transport patterns (a piece of the feedback loop). Bar response is related to a parameterization of the wave conditions and this relationship is used to describe the role of morphologic feedback. Chapter 6 synthesizes the contributions that this thesis has made towards understanding nearshore morphologic evolution.

CHAPTER II: INTERTIDAL BEACH PROFILE ESTIMATION USING VIDEO IMAGES

1. Abstract

In this paper, we present a technique suitable for measurement of intertidal bathymetry over a broad range of length scales (10^1 to 10^3 m) and time scales (days to decades). A series of time-averaged images of the swash zone are used to map contour lines of the beach surface. In each image, contours are identified using bands of maximum brightness associated with breaking waves at the shoreline. By mapping the location of these bands in a sequence of images collected over one tidal cycle, contour maps of the intertidal bathymetry are generated. We expect this technique to work best (smallest absolute error) under waves which are nearly reflective at the shoreline, but break enough to be observed visually. This is typical of a barred beach since the wave height at the shoreline is limited by wave breaking over the bar crest.

The ability of the measurements made with this technique to resolve actual beach elevation variation depends on the ratio of the measurement error variance to the true beach elevation variance. Thus, large measurement errors may be compensated by either large tidal ranges or large temporal changes of the beach itself. In a comparison to bathymetry surveyed using a Differential Global Positioning System (DGPS) during the Duck94 experiment, in Duck, N.C., the image-based elevation estimates were well correlated with the actual bathymetry. The deviations (image-based vs. DGPS measurements) may be partially attributed to effects scaled by wave height at the shoreline, wave induced setup, and wave height saturation over the sand bar. In particular, setup was important during dissipative conditions. The rms deviation (vertical) between the DGPS and image-based bathymetry was reduced from 0.24 m to 0.06 m by correcting for the systematic deviations due to variations in setup and wave height saturation. Further improvement of the elevation

estimates resulted from parameterizing the actual bathymetry with a simple plane beach surface, which reduced random (or unresolvable) measurement errors. This led to estimates of the beach slope that were accurate to within 10% of the actual slope and estimates of the cross-shore location of the mean sea level line accurate to about 0.50 m.

2. Introduction

Variation of beach morphology occurs over a wide range of spatial and temporal scales. Near the shoreline, for example, beach elevation fluctuations of O(1 m) typically occur over periods of weeks to months [*Winant, et al.*, 1975; *Aubrey*, 1979; *Aubrey, et al.*, 1980; *Wright, et al.*, 1982], while low amplitude, O(0.1 m), fluctuations can take place within minutes [*Sallenger and Richmond*, 1984; *Howd and Holman*, 1987]. Alongshore, spatial variations include beach cusps with alongshore wavelengths of O(10 m) and megacusps, O(100 to 1000 m). Measurements of nearshore morphology typically resolve variations within narrow wavenumber and frequency bands, limited by the spatial extent and duration of sampling. For example, conventional beach profiling techniques usually require a person to traverse the entire region of interest within several hours of a low tide. The resulting sampling pattern may not resolve variability at all important scales. Video-based techniques, which have become increasingly useful in many fluid and sediment processes studies, have been used to make quantitative measurements of sediment transport [*Drake*, 1988], measurements of wave runup [*Holman*, 1984; *Holman and Sallenger*, 1986; *Holland, et al.*, 1991; *Holland and Holman*, 1993; *Holland, et al.*, 1995], the position of the shoreline and sand bars [*Lippmann and Holman*, 1989; *Lippmann and Holman*, 1990; *Lippmann, et al.*, 1993], and beach profiles [*Holman, et al.*, 1991]. We will extend these video capabilities to measure intertidal beach elevations that span alongshore distances up to 1-2 km, sampling daily over long sample periods.

Our approach is to map contours of beach elevation using a visible line corresponding to the tidal elevation. In the absence of waves, a visible contour is the still water level intersection with the beach surface, or the still water level shoreline (SWLS). As the tide rises and falls, the SWLS moves onshore and offshore, and marks contours at different tidal elevations. Thus, by delineating the SWLS repeatedly over a tidal cycle, one could generate a contour map of the intertidal foreshore. To apply this idea using video images, we must identify a visual representation of the shoreline and map its location in the image to meaningful field coordinates. In the presence of waves, the SWLS is obscured by swash motions and breaking waves (Figure 1a). So, we turn to video time exposure images of the surf zone (Figure 1b), which reveal a proxy for the SWLS ([*Lippmann and Holman*, 1989] -- hereafter denoted LH89). The time exposures used here are digital images obtained by averaging a sequence of image frames (or snapshots) using a computer-based image processor. A time exposure of the surf zone shows patterns in which white areas correspond to sand bars and the shoreline (Figure 1c) where breaking waves consistently produce foam. In deeper water, waves break less frequently, producing less foam, and these regions are relatively dark in an image. We will call the light intensity feature that corresponds to the shoreline the shoreline intensity maximum (SLIM) line (Figure 1c), and use it in place of the SWLS. We need to know when the SLIM can be used effectively to estimate beach elevations.

Many complications arise from using the SLIM as a proxy for the SWLS. Of particular importance is the relationship of the SLIM location to the SWLS, which depends on the local (swash zone) morphology and wave conditions, as well as nonlocal processes such as waves breaking over a sand bar. Our approach in this paper is to first understand the nature of the complications that affect this technique by using some simple models based on wave dynamics. From a conceptual understanding of the SLIM-SWLS relationship, we outline the expected, systematic behavior of errors that may be encountered

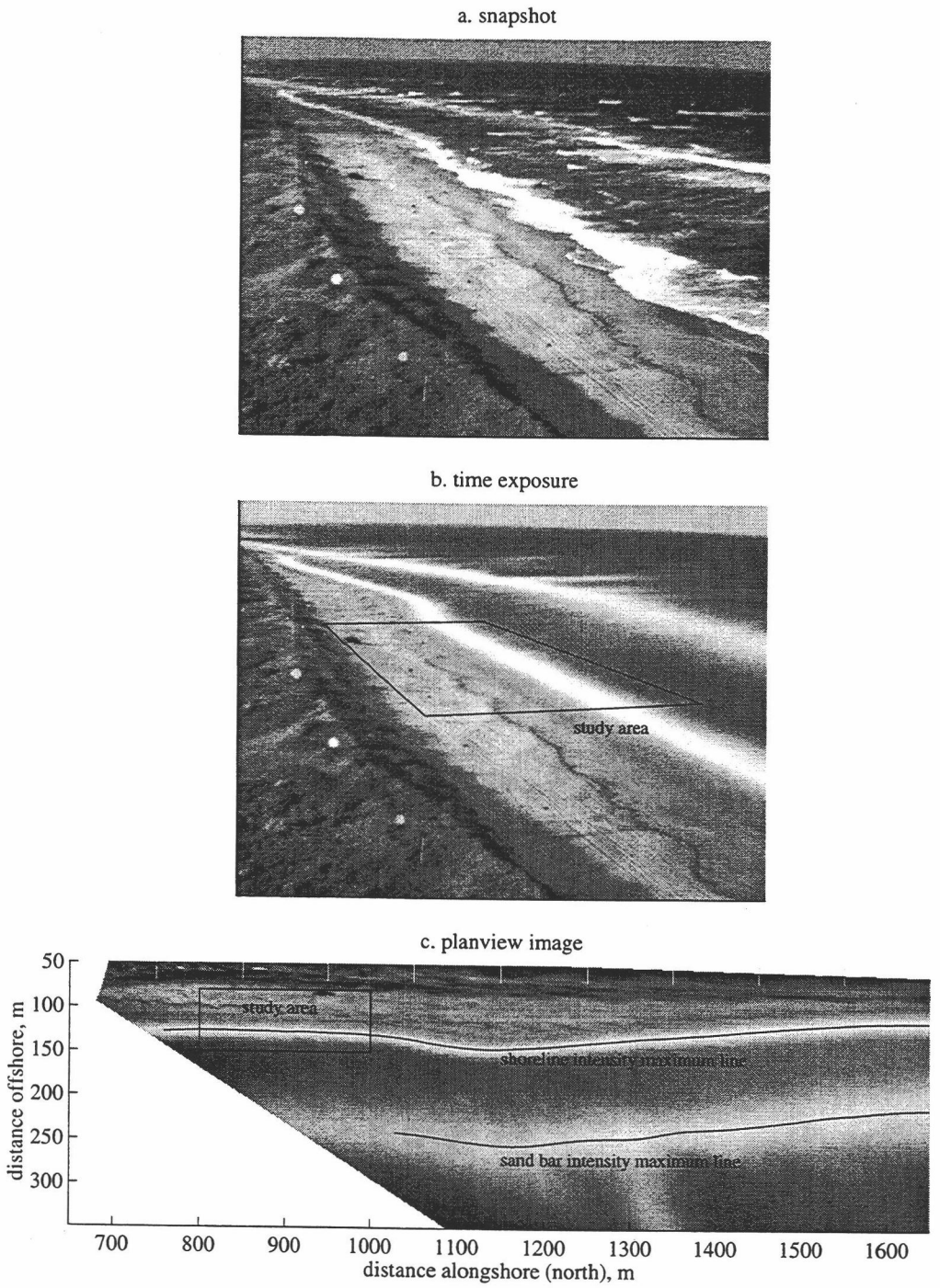

Figure II.1. Video images of the Duck, North Carolina field site on 11 Oct. 1994. The camera is aimed towards the north-east with a wide field of view. Waves breaking preferentially over a sand bar and at the shoreline can be seen in a snapshot (a). In the time exposure (b), we see the intensity patterns (maxima) corresponding to both the sand bar and shoreline. The region where video-based estimates and surveyed bathymetry were compared is marked in both the time exposure and in the planview projection of the time exposure (c).

when using this surveying technique in a variety of beach settings. Next, using a field comparison between accurately surveyed bathymetry and SLIM estimates, we test our understanding of the processes that contribute to these systematic measurement errors. Then, we develop some empirical methods to remove both systematic and random measurement errors. Finally, we discuss how the errors inherent in this technique will affect attempts at recovering time series of morphological variability from different beach settings.

3. Theory

3.1. Qualitative description of SLIM behavior using dissipation theory

Since breaking waves result in wave energy dissipation, it is reasonable to assume that the presence of time-exposure intensity maxima, such as the SLIM, require dissipative conditions. LH89 showed that image intensity patterns were qualitatively similar to expected patterns of time-averaged, energy dissipation rates of a breaking, random, wave field, based on a model described by *Thornton and Guza* [1983] -- hereafter denoted TG83. In the absence of a sand bar (e.g. on a plane beach), this model predicts a single dissipation maximum (Figure 2a) located in a water depth that is proportional to the rms wave height. The dissipation maximum on a plane beach shifts offshore indefinitely as the wave height increases. On a barred beach, however, the TG83 model predicts that the rate of energy dissipation can reach a maximum over a sand bar and then another maximum as the depth decreases again towards the shoreline (Figure 2b). It is relevant to our intended use of the SLIM to note that a sand bar tends to maintain a narrow dissipation peak that is always positioned near the shoreline, even over large variations of the offshore wave height.

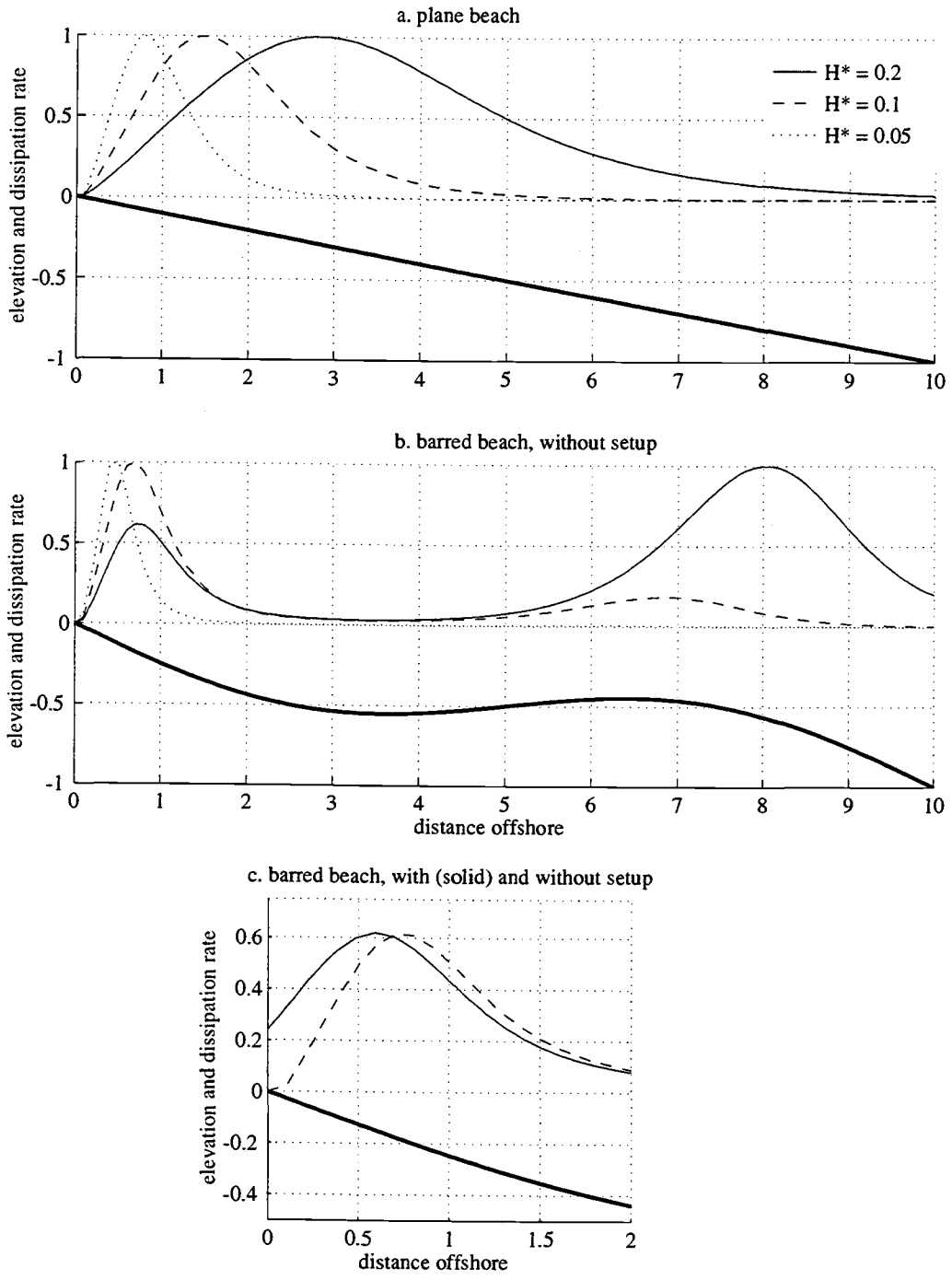

Figure II.2. (a) Example of expected (using TG83 model) wave energy dissipation rates (normalized by the maximum dissipation) on a plane beach. The beach elevation (heavy line) is normalized by the maximum depth. The similarly normalized wave heights in the example are H* = 0.05 (dot-dash), 0.1 (dash), and 0.2 (solid). (b) A synthetic, barred beach was generated by subtracting a sinusoidal elevation with amplitude of 0.25 and wavelength of 10, and the same sequence of wave heights were used to calculate dissipation. Setup was neglected in the previous two examples. (c) The effect of setup is shown for H* = 0.2, focusing on the shoreline region.

There are, of course, reasons to suspect that the TG83 model will be of limited practical use, even if it were an accurate description of the dissipation process and resulting time-averaged intensities. For example, as Figure 2b shows, the SLIM location depends on the usually unknown location and elevation of the sand bar. Furthermore, the spatial patterns of dissipation are modulated by the tide level, as the water depth over the bar changes. Also, there are processes that were neglected in the TG83 model, such as wave-induced setup and swash oscillations (runup). The effects of setup tend to compensate the effects of increasing wave height by shifting the dissipation maximum onshore (Figure 2c). Even on reflective beaches, swash tends to produce some foam and, hence, produces a SLIM that may behave differently than dissipation in the TG83 model. Swash motions can be dominated by infragravity frequency motions, which might smear the SLIM over a much wider cross-shore region. Also, some bathymetric features may not yield a simple mapping between the SLIM position and bathymetry. One example is a beach step near the shoreline, which tends to fix the location of maximum breaking intensity. Finally, alongshore bathymetric variations such as beach cusps and crescentic sand bars or rip current channels, may lead to a great deal of alongshore nonuniformity in the relationship between the SLIM and the SWLS locations.

In spite of the possible difficulties that may be encountered in an application of the SLIM bathymetry estimator, we can at least classify the behavior of the SLIM-SWLS relationship as a function of different morphodynamic settings. Two factors are important. First, the morphological setting controls the range of effects acting on the SLIM. Possible extremes include barred beaches under high waves (most complicated) vs. a plane beach under small waves (relatively simple). The second factor is the reflectivity of the shoreline, which ought to govern the local behavior of the SLIM. Under the most dissipative conditions the SLIM will be displaced far from the SWL shoreline (on a nonbarred profile), while it may be nonexistent under the most reflective conditions. We will use the Irribaren

number, $\xi = \beta \left(\frac{H_o}{L_o}\right)^{-1/2}$, to differentiate regimes. Here, β is the beach slope in the vicinity of the SLIM; L_o and H_o are the deep water wave length and height. In general, $\xi<1$ (relatively flat beach slopes) corresponds to dissipative dynamics (breaking waves at the shoreline) and $\xi>1$ (relatively steep beach slopes) corresponds to reflective conditions [*Battjes*, 1974].

3.2. Quantification of SLIM relationships to bathymetry

We turn now to the task of quantifying the relationship between the SLIM estimates and the true bathymetry of the beach surface, z_{bed}. The general situation at a particular time t_o and at the horizontal coordinates (x_o,y_o) of the SLIM is

$$z_{bed}(x_o,y_o,t_o) = z_{tide}(t_o) + \bar{\eta}(x_o,y_o,t_o) - d_{slim}(x_o,y_o,t_o), \qquad (1)$$

where z_{tide} is the measured tide level and $\bar{\eta}$ is the total setup at the location of the SLIM. Here, setup is the elevation of the mean water level above the measured (known) tidal level, averaged over a time exposure period, and d_{slim} is the mean water depth at the SLIM coordinates (Figure II.3). Of the terms on the right hand side of equation 1, we expect that only z_{tide} is measured directly. Since we wish to apply this technique in situations with minimal field support (or retroactively on an increasingly vast collection of nearshore images), we may need to either estimate $\bar{\eta}$ and d_{slim} from, say, offshore wave gage data, or accept their contribution to measurement error. Determining setup is a fluid dynamics problem, which has been addressed theoretically, in the laboratory, and in field experiments [*Bowen, et al.*, 1968; *Guza and Thornton*, 1981; *Holman and Sallenger*, 1985]. On the other hand, the SLIM depth depends on the relationship between light intensity statistics and nearshore fluid processes.

If effects of setup or the SLIM depth cannot be neglected in an application of this beach contouring technique, two approaches to estimating these parameters are:

1) Model $\tilde{\eta}$ and d_{slim} from a fluid dynamical process point of view.

2) Model $\tilde{\eta}$ and d_{slim} using empirical methods.

The first approach is attractive since we can derive some physics-based expectations for the behavior of the unknown parameters. The disadvantages, as noted above, lie in the number of parameters needed as input to models (such as the offshore bathymetry), which may not be readily available in most applications of the technique. The second approach is attractive in that good performance may be obtained with a limited number of inputs. The second approach, however, will likely yield a site-specific calibration, which may require some site-specific ground truth testing. We will use the results of a field comparison between SLIM bathymetry estimates and accurately surveyed bathymetry to compare simple, process-based models with empirical models. This comparison will at least test our expectations of the qualitative behavior of the SLIM's relationship to water depth.

4. Field test

Our technique was tested using data from the Duck94 experiment, which was conducted at the Army Corps of Engineers Field Research Facility (FRF), Duck, North Carolina in August and October 1994. This beach had a well developed sand bar that was initially ~100 m seaward of the shoreline, but moved up to 100 m seaward over the study period. The beach slope was steep (mean $\beta = 0.08$) at the shoreline. The average significant wave height (measured directly offshore in 8 m water depth) was about 1 m, and the peak wave period was typically about 7 s. The wave height and period were measured in 2 m water depth as well (Figure 4). The maximum tide range during this study period was 1.6 m, and the mean level was 0.35 m (above NGVD29). Tide elevations were recorded every 6 minutes at the end of the FRF pier in about 6 m water depth (mostly outside of the

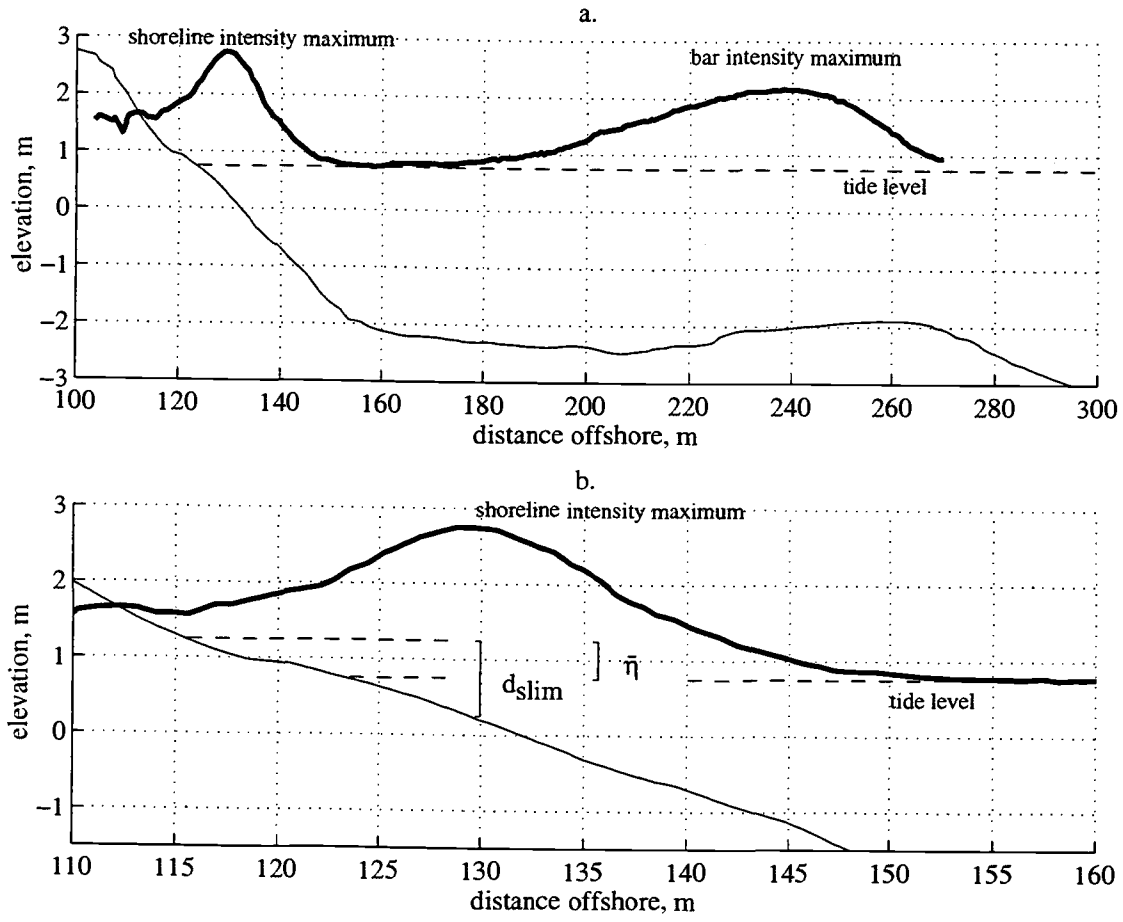

Figure II.3. (a) Comparison of a cross-shore beach profile (thin solid line) and an intensity profile (bold line, arbitrary scale) on 11 Oct. 1994 along y=950 m. The intensity maxima corresponding to the shoreline (x~130 m) and sand bar (x~240 m) are obvious. (b) Definition sketch of terms in equation 1, showing the inner portion of the intensity and beach profiles.

surfzone) with a NOAA operated tide gage. Note the strong tidal signal in the wave height record from the gage located in 2 m mean water depth (inside the bar crest) -- a result of wave height limitation due to breaking over the bar.

Ten minute long, time-averaged video images were digitized at half hour intervals during the daylight hours of 9-19 August and 3-21 October 1994. At this study site the maximum tidal variation over 10 minutes could be up to 0.10 m at a mid tide stage, but was

usually much less. We used a camera which focused narrowly on the 200 m long study area (Figure 5). The camera choice minimized errors due to digitization and photogrammetric uncertainty. Ground-truth bathymetry were surveyed daily at low tide using a Differential Global Positioning System (Trimble 4000), which was accurate to several centimeters in the vertical (rms error ~ 0.01 m; Plant and Holman, in preparation). These surveys ran along roughly shore-parallel lines, between elevations ranging from -0.50 to +3.5 m NGVD29, with samples separated by ~5 m alongshore and as close as 2 m in the cross-shore direction. Since these data were not synchronous or co-located with the image-based estimates, the DGPS data were interpolated temporally and spatially using linear interpolation in time, and an inverse distance scheme in space to the horizontal coordinates of the image data. The bathymetry was also surveyed to 4 m depths with the Coastal Research Amphibious Buggy (CRAB, a 10 m high surveying vehicle) along transects separated by 15 m alongshore. These data were used to quantify the bathymetry over the bar.

Standard photogrammetric techniques (LH89) were used to map video image (2-D) to field (3-D) coordinates. The horizontal resolution in field coordinates depends on the pixel (picture element) footprint dimensions, which ranged from 0.10 (cross-shore) by 0.30 m (alongshore) nearest the camera to 0.25 by 1.00 m at a point farthest from the camera. The pixel footprint is the projection of one pixel on the mapped surface. We generated planview images (Figure 1c) with 0.25 m horizontal resolution, which was the maximum cross-shore pixel footprint dimension. The projection of the cross-shore pixel footprint on the beach slope yielded a vertical component of error of about 0.025 m, which is small by most standards of beach surveying.

To locate the field coordinates corresponding to the SLIM, intensity, I(x,y), was scanned along cross-shore oriented lines for a maximum. Figure 1c shows a typical SLIM

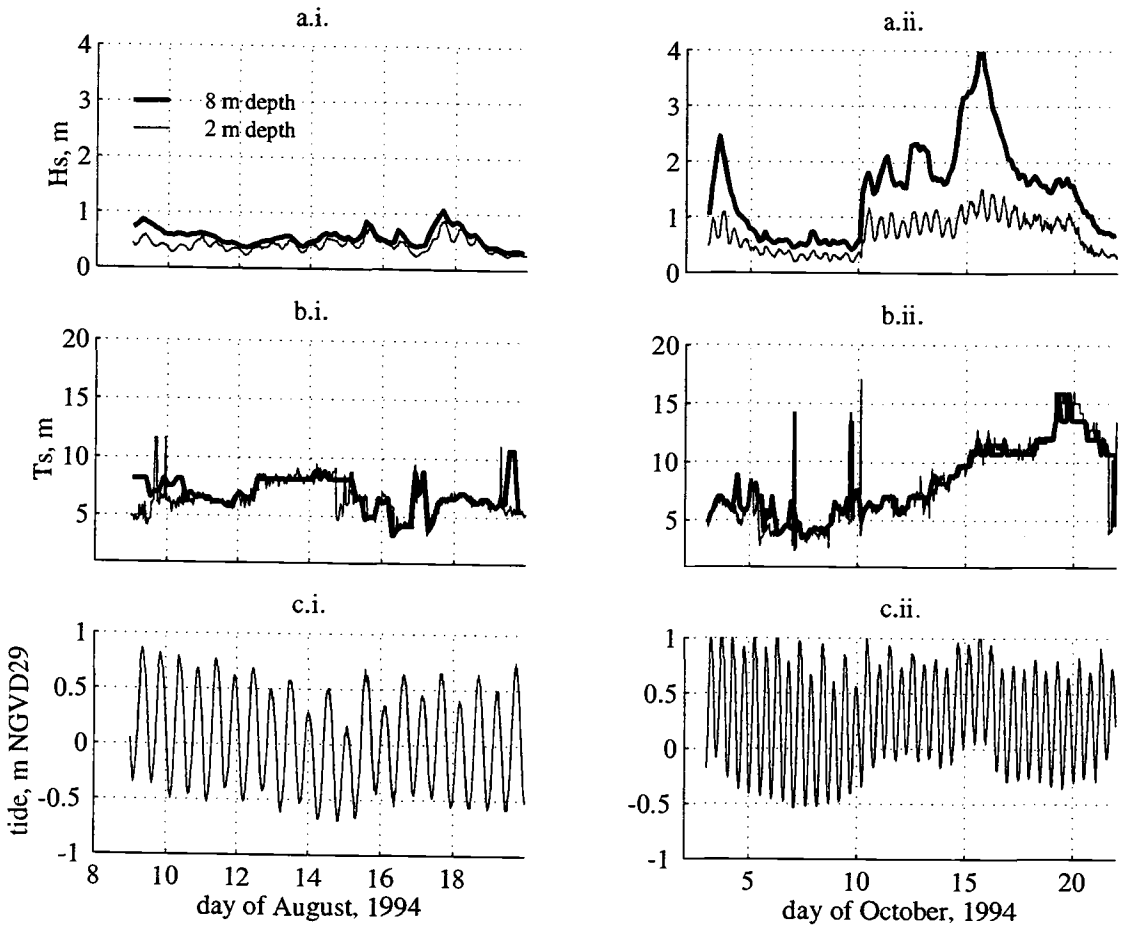

Figure II.4. Time series sampled during (i) 9-19 Aug. and (ii) 3-21 Oct. 1994 of (a) significant wave heights and (b) peak periods from *p3111* (heavy lines) and *p641*, and (c) tides from the FRF pier.

line, plotted on the planview image from which it was extracted. Since the shape of intensity profiles varied somewhat, we tested the performance of several SLIM definitions. The best SLIM position algorithm minimized the variance of the error between the SLIM position and the SWLS position. Of the several methods tested, the best algorithm consisted of the following steps:

(1) Select a segment of an intensity profile within a 25 m wide window (broader than the typical swash zone) centered about an initial guess at the cross shore position of the SLIM.

(2) Normalize the observed intensities, I, to $\tilde{I}$ such that $0 \leq \tilde{I} \leq 1$.

(3) Select a centered subwindow width based on the area, $A=\sum \tilde{I}$, under the normalized intensity curve, which was narrow enough to exclude intensity signals that were far from the maximum, such as those which correspond to the dry beach. A width of $\frac{A}{2}$ was used.

(4) Fit the normalized intensity profile within the subwindow with a quadratic polynomial, whose maximum location was used as the SLIM location. This step eliminated spurious effects due to narrow local maxima (spikes).

(5) Repeat steps (1-4) for all alongshore sample coordinates in the field of view, tracking the SLIM line alongshore by using each result to begin the next search.

Data extracted from an image were excluded from this analysis if (a) the curvature of the intensity, $\frac{\partial^2 \tilde{I}}{\partial x^2}$, along a particular cross-shore profile fell below 3 standard deviations of the mean of all the curvatures within that image (i.e. reject cases with flat intensity profiles); (b) the shoreline region was obscured, or (c) the estimated SLIM strayed from the actual intensity maximum line (checked manually). This last check was needed when equipment involved in the Duck94 experiment or tire tracks on the beach attracted the SLIM search algorithm by forming local intensity ridges. A total of 426 (out of 547) images yielded acceptable SLIM positions. Some samples were not analyzed if they corresponded to beach elevations below the elevation for which surveyed data were available, typically about -0.50 m NGVD29 (60 images had no data in this range). A total of 366 images were retained for comparison to surveyed bathymetry.

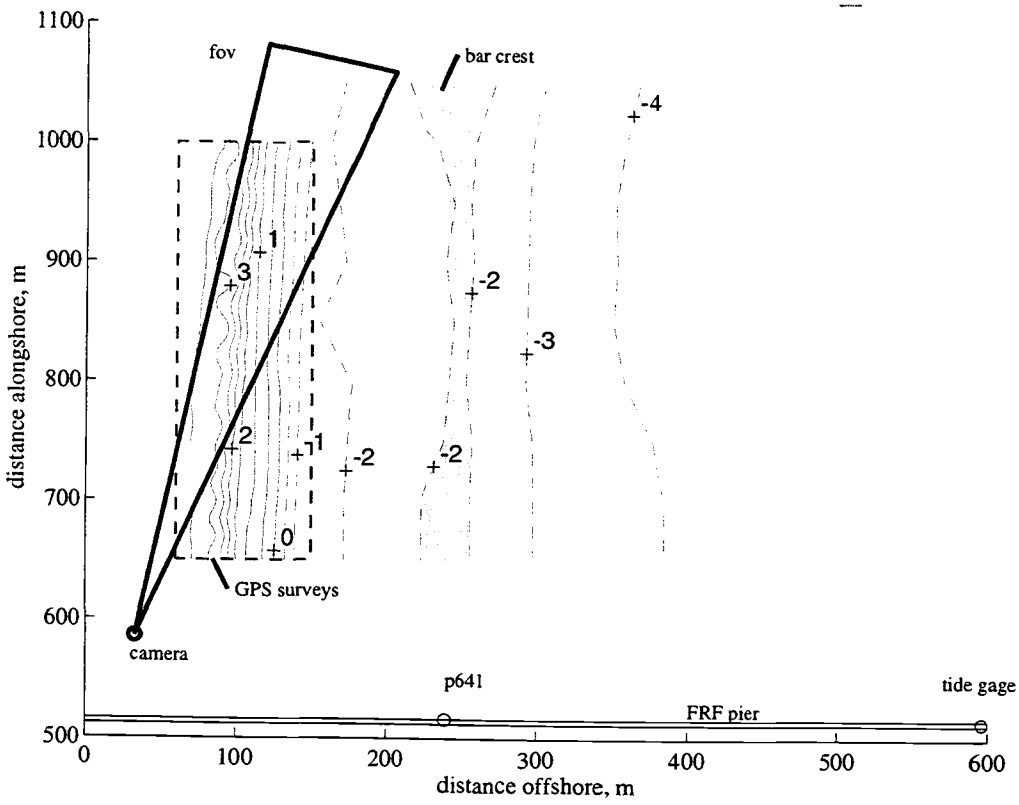

Figure II.5. Location map of the Duck, N.C, field site. Pressure gages are *p641* (at 2 m depth), and *p3111* (not shown, located at 8 m depth; x=914; y=825). Contours (for 11 Oct.) of the beach elevation below -1.0 m were estimated from data surveyed by the FRF CRAB. Contours above -0.5 m were estimated from data surveyed with the DGPS system. The field of view (fov) of the camera used in this study is outlined in bold and the bar crest region is shaded.

5. Results

Rough estimates of the bathymetry are easily obtained by neglecting setup and the actual water depth at the SLIM location in equation 1. This is equivalent to assuming that the true beach elevation at the horizontal coordinates of the SLIM is equal to the tidal elevation. Comparing these raw SLIM estimates to the DGPS bathymetry allows us to assess the importance of the other two terms in equation 1 as well as test our understanding of those terms.

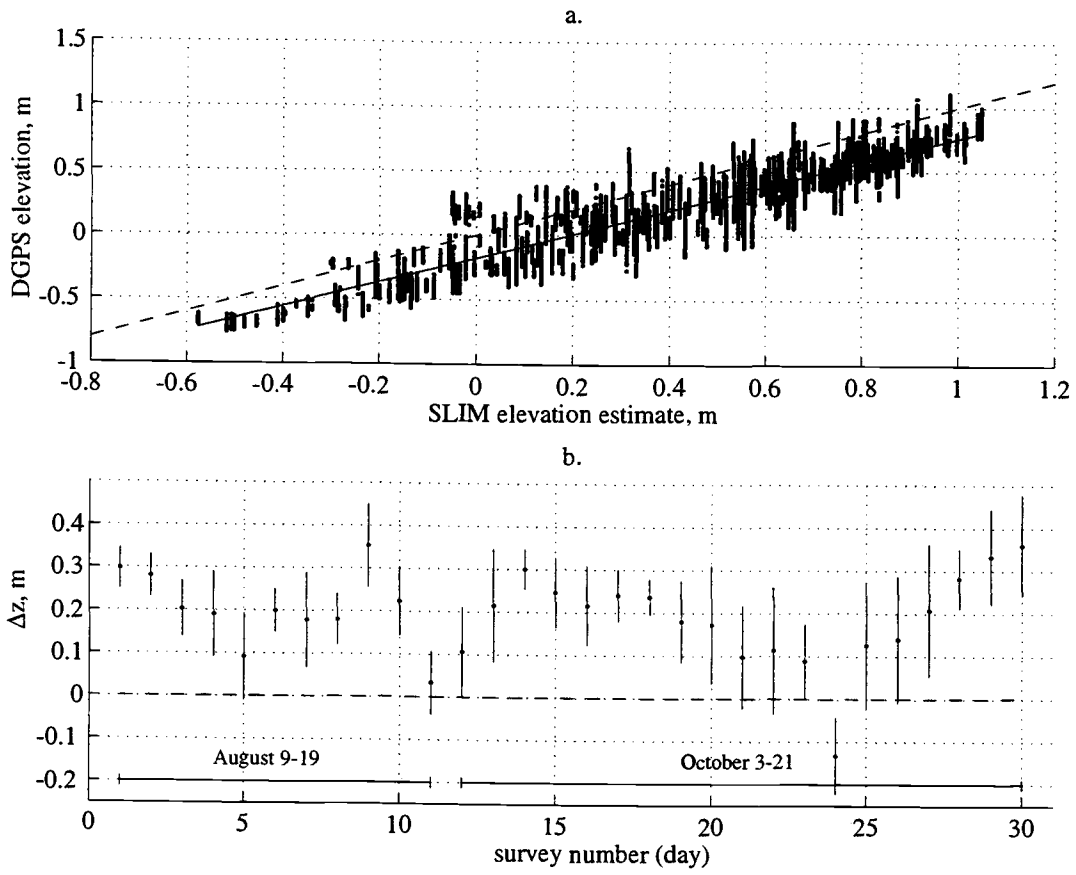

Figure II.6. (a) Regression (solid line) of the surveyed beach elevations (data co-located with the SLIM positions) vs. the corresponding SLIM estimates (= tide level). The regression model, $z_{dgps}(t) = \alpha_o + \alpha_{tide}\, z_{tide}(t) + \varepsilon(t)$, explained 88% of the surveyed elevation variance (R^2=0.88, α_o=-0.17±0.02 m, α_{tide}=0.94±0.04). The dashed diagonal line lies along the 1:1 relationship. (b) Time series of daily mean elevation differences. The error bars are standard deviations.

5.1. Beach elevation estimates

Plotted in Figure II.6a are the DGPS bathymetry (z_{dgps}) estimates vs. the SLIM-estimated beach elevations, which, in this case, simply equal the tide level (z_{tide}) at any SLIM location. The variation of the SLIM bathymetry estimates were well correlated to the DGPS bathymetry (R^2 = 0.88). Thus, 88% of the beach elevation variance within the inter-tidal region was recovered at the study site using the SLIM technique. However, as

expected, the SLIM typically lay seaward of the SWL shoreline and the raw estimates included an elevation offset. The mean difference between these SLIM-estimated and DGPS elevations ($\Delta z = z_{tide} - z_{dgps}$) averaged over all samples was 0.20 m, and the standard deviation about this difference was 0.14 m. Mean elevation differences averaged over single images (i.e. alongshore averaged) ranged between 0.58 and -0.29 m. The standard deviations about these alongshore-averaged differences ranged from 0.01 to 0.22 m.

Figure II.6b illustrates that the scatter observed about the regression line in Figure 6a tends to be due to two components. One component is the scatter about a mean offset on a particular day. This scatter accounted for approximately 40% of the total error variance, and may be due to tidally modulated processes or alongshore variations. The second component is the slow (relative to the daily sample interval) variation of daily mean elevation differences, which accounted for 60% of the total error variance. The slow component of variability may be due to variation in the wave climate or changes in the beach morphology itself.

5.2. Beach profile characteristics

We can see how well the beach surface is described by the raw SLIM data by comparing, for example, cross-shore profiles. Figure 7 gives an example of both DGPS and raw, SLIM beach profiles extracted from the same alongshore range (y = 950 m) for each day of this study. Because DGPS surveys were conducted only once daily, the range in the surveyed profiles from the day before to the day after each date are shaded. At times, actual beach change (which can occur within hours or even minutes) has corrupted our error estimates by an unknown amount. Since the spatial coverage of surveys varied from day to day, only the portions of the profile where DGPS and SLIM data overlapped were used in

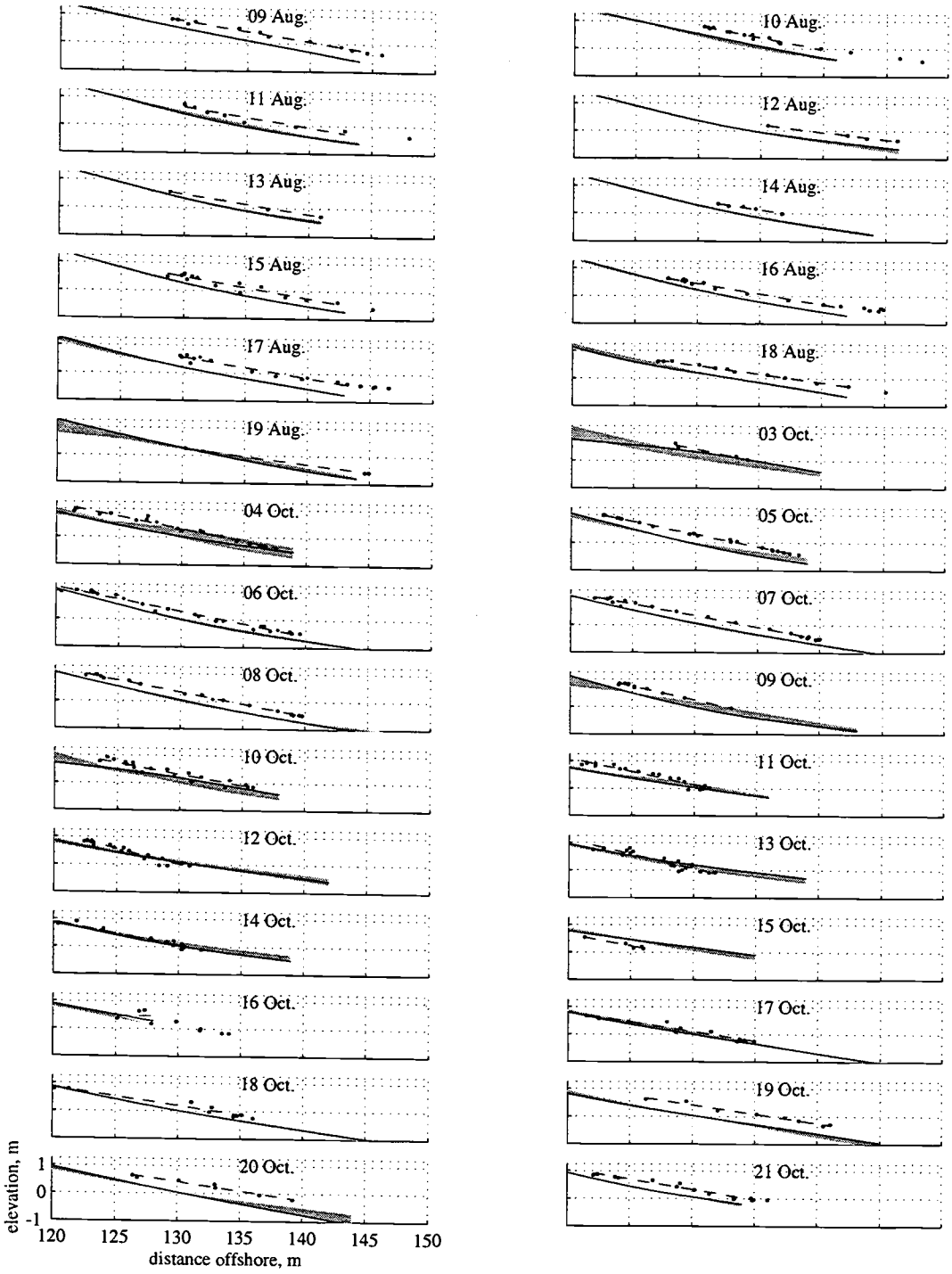

Figure II.7. Cross-shore profiles of raw, SLIM elevation estimate (•) and corresponding DGPS-surveyed profile (solid line). The best linear fit to the SLIM data (dashed line) is Figure II.6b shows a time series of the daily-averaged elevation differences. The error bars indicate variation of the estimate error over each day (i.e. averaged over both a tidal cycle and alongshore).

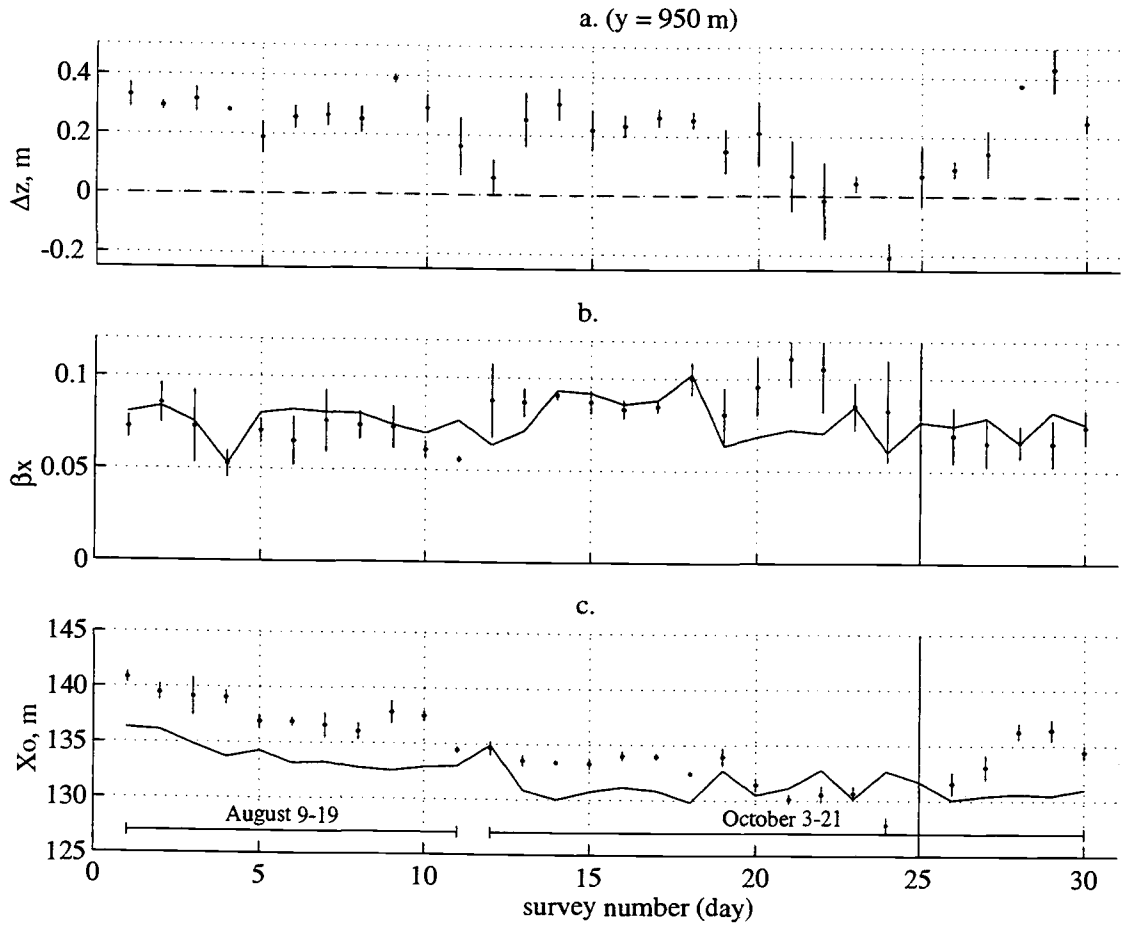

Figure II.8. (a) Time series of daily mean elevation difference between a plane beach profile (fit to SLIM elevations) and DGPS elevations at y=950 m. Time series of cross-shore slope (b) and MSL intercept (c) are estimated from both DGPS data (solid lines) and SLIM data (dots). 95% confidence limits are shown about SLIM data.

the comparison. It is clear that there are systematic errors in the estimated profiles. The error appears as a mean offset, a slope discrepancy, and random error.

Figure II.8a shows the daily mean elevation differences, with standard deviations of the error presented as error bars. The beach slopes estimated using the SLIM technique (β_{slim}) and the surveyed slope (β_{dgps}) were determined with a linear regression. Systematic errors in the estimated slope (Figure 8b) tend to vary slowly over several day periods,

similar to the daily averaged offsets. Along the particular profile shown in Figure 7, the mean difference between estimated and surveyed slopes (averaged over the entire study period) was negligible ($\overline{\beta_{slim}-\beta_{dgps}} = 0.002$). The standard deviation of the differences was 0.015 (or about 10% of the mean slope). In Figure 8c, the daily time series of the position of the MWL intersection with the beach surface (X_o) is displayed. The SLIM-estimated position is, on average, seaward of the true position (by 2.49 m) due to the elevation offset. Significant differences between the estimated and true slopes result from systematic variation of the SLIM-DGPS elevation offset over a tidal cycle. Possible causes include tidal modulation of swash zone processes such as changing intertidal slope (concave beach profiles) and/or tidal modulation of the wave field (e.g. the amount of breaking over the sand bar).

6. Error analysis

Before addressing further the capability of this technique to resolve daily variations in bathymetry (including the beach slope), we would like to determine to what degree systematic deviations between the raw SLIM estimates and DGPS surveyed bathymetry were due to changing hydrodynamic settings. We expect that the deviations are related to the local (swash zone) wave conditions as well as nonlocal dynamics such as setup (a quantity that is integrated over the surfzone) and tidally modulated wave height limitation over the sand bar. To this end, the inter-comparisons between the DGPS surveyed and SLIM bathymetry estimates can be divided into dynamically similar situations, which fall between the extremes of reflective (no setup and minimal breaking) and dissipative beach faces (lots of setup and breaking) with respect to the incident wave field and the intertidal beach slope. The field comparison spans some of the environments between these extremes.

Table II.1. Setup observations made in the field.

reference	$\frac{\bar{\eta}}{H_b}$	γ	$(h+\bar{\eta})_{obs}$	beach type
Guza and Thornton, 1981	0.24	0.42	0.03 m	plane
Holman and Sallenger, 1985	0.14 to 2.8	0.28 to 0.54[a]	0.005 m	barred
Holland et al., 1995	0.35 to 0.70	0.42[b]	≤0.02 m	plane
Holland et al., 1995	0.07 to 0.14	0.42[b]	0.25 m	plane

a. Values are from Sallenger and Holman, 1985.
b. Value are from Guza and Thornton, 1981.

The Irribaren number, $\xi = \beta \left(\frac{H_o}{L_o}\right)^{-1/2}$, was used to differentiate hydrodynamic regimes (reflective if $\xi >> 1$ and dissipative if $\xi << 1$) during our study of a barred beach system. For the calculations made here, β is the beach slope at each SLIM coordinate (averaged over a 4x4 m (horizontal) window, using the DGPS data), L_o is the deep water wave length ($L_o = \frac{g T^2}{2\pi}$, where T is the peak wave period), and H_o is the deep water (rms) wave height. This definition of the Irribaren number was only consistent for describing reflective conditions, since the swash zone remained dynamically reflective over most tide and wave conditions as a result of wave height limitation over the sand bar. Thus, we will use the presence or absence of breaking over the bar as another distinguishing criteria. In the comparisons that follow, the breaking wave height H_b is also used, since it ought to be the relevant wave height to scale wave-breaking dependent processes, such as setup. It is estimated as the linearly shoaled rms wave height that satisfies [*Komar*, 1974].

$$H_b = \gamma h_b, \qquad (2)$$

where h_b is the water depth at the break point. In all cases, γ was set to $\frac{1}{2}$, which is consistent with values found in field studies at Duck (Table II.1).

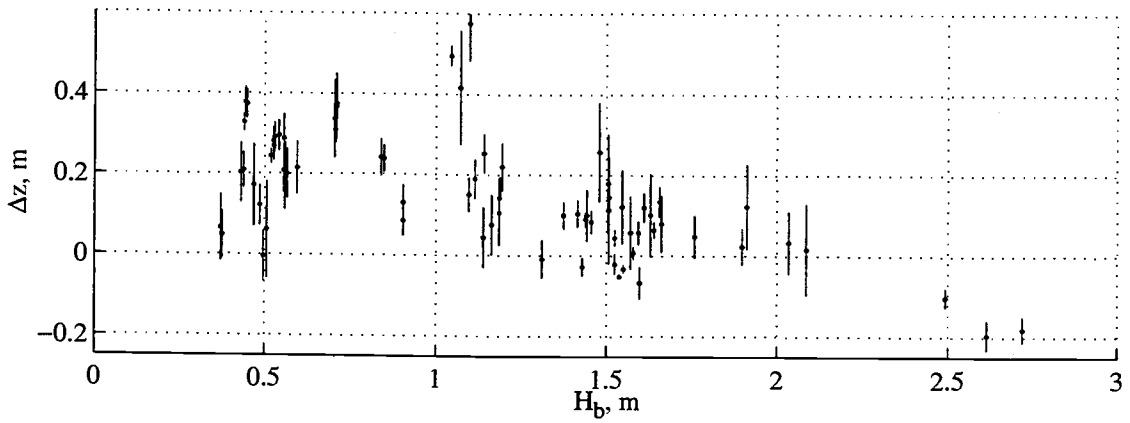

Figure II.9. The alongshore-averaged elevation difference (z_{tide} -z_{dgps}, error bars represent standard deviations) as a function of breaking wave height.

Figure II.9 shows how systematic elevation errors were related to wave height. Here, Δz are the alongshore averaged elevation differences between z_{tide} and z_{dgps} at the slim locations. The pattern is that of initially increasing (positive) error as wave height increases up to a critical wave height (about 1 m, likely corresponding to breaking over the sand bar). As wave height increases further, the mean error actually decreases. In Figures 9 and 10 (to follow), only a subset of the observations have been included. Of the available data where $\xi>1$ (reflective), data were omitted if breaking was observed over the offshore sand bars. Thus, these data correspond to a simple, plane beach under mostly reflective conditions. Where $\xi<1$, data were omitted if breaking was not observed over sand bars, so that conditions of dissipation over a barred profile were represented. The nearshore system often fell somewhere between these two operational end members and a total of only 76 of 366 images were examined here. Figure 10a shows the error normalized by H_b as a function of ξ. Two groupings, one at high ξ and one at low ξ, are apparent. For $\xi<1$ (dissipative conditions), $\frac{\Delta z}{H_b}$ is small or negative (less than about $\frac{1}{5}$); while, for $\xi>1$ (reflective) $\frac{\Delta z}{H_b}$ is larger (about $\frac{1}{2}$). These differences are likely due to setup and wave

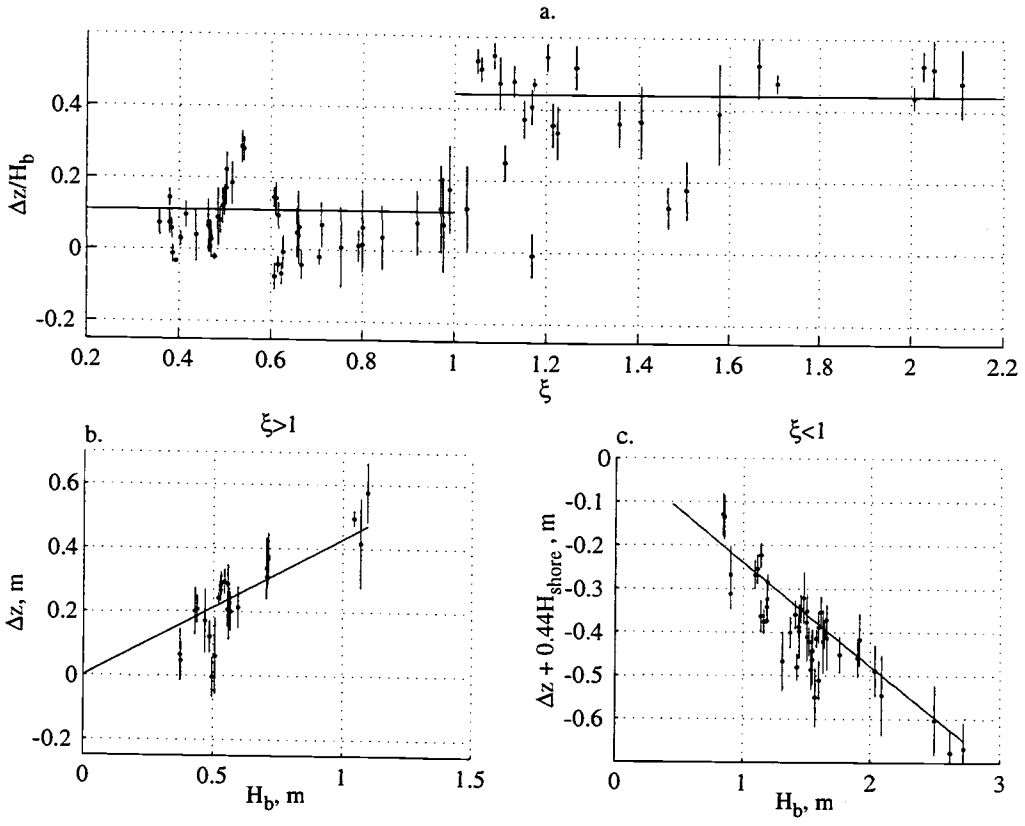

Figure II.10. (a) Alongshore-averaged elevation difference as a function of Irribaren number. (b) For reflective conditions ($\xi>1$), the deviations increase with increasing wave height (solid line is $\Delta z = 0.44\ H_b$). (c) When breaking occurs over the bar and the surfzone is dissipative ($\xi<1$ over the bar), the deviations (corrected for Case I) decrease with increasing wave height (solid line is $\Delta z = -0.24\ H_b$).

height saturation over the bar, which are important only after the onset of breaking. We examine the two dynamical conditions in detail below.

6.1. Plane reflective beach

Although the beach at Duck is barred, under low wave height conditions (relative to the water depth over the bar) the bar does not affect the waves climate at the shoreline. Under these conditions, we can treat the SLIM bathymetry estimation problem as that of a

plane beach. We ignore for the moment the slight concavity of the intertidal profiles and expect a simple relationship between the elevation offset and breaking wave height. Figure 10b shows that Δz scales as about $\frac{1}{2} H_b$ for reflective conditions. Setup should be negligible, and we might expect that $\Delta z = d_{slim}$ (equation 1). For this dynamical condition, the best linear relationship between Δz and H_b can be determined using the empirical model

$$\Delta z(t) = \alpha_b H_b(t) + \varepsilon(t), \qquad (3)$$

where α_b is a coefficient (determined via linear regression) and ε is assumed to be random error. This model was significant at the 95% level (R^2=0.7, R^2_{crit}=0.2, α_b=0.43±0.26). Although equation 3 constrained the estimates to pass through the origin, when using the two parameter model ($\Delta z(t) = \alpha_o + \alpha_b H_b(t) + \varepsilon(t)$), the intercept did not differ significantly from zero. For this site and under these conditions, wave height variations explain 70% of the alongshore-averaged SLIM measurement error variance.

6.2. Dissipative barred beach

The effects to be examined in this case are those due to setup and wave height limitation over the bar crest. We have selected those conditions when waves are breaking over the bar, and we expect significant nonlocal effects to affect the swash zone dynamics. Since setup is a well studied phenomena, we present a brief review of theoretical and observed relationships, against which we can compare our observations. Next, we parameterize the depth limitation process over the sand bar, so that knowledge about the sand bar in this particular field test can be included in the error analysis. Then, we test a simple empirical model to determine if the bathymetry estimation errors are consistent with our qualitative expectations.

6.2.1. Setup

To estimate setup, *Bowen et al.* [1968] used the surf-zone momentum balance equation, and assumed wave height saturation inside the break point:

$$H = \gamma (h + \bar{\eta}), \text{ for } 0 \le (h + \bar{\eta}) \le \frac{H_b}{\gamma}. \quad (4)$$

H is the spatially varying wave height; h is the spatially varying still water depth; γ is the (constant) ratio of the wave height to water depth, and H_b is the wave height at the break point. Assuming a plane sloping beach and integrating from the break point to the shoreline, the total setup at the still water level shoreline is

$$\bar{\eta}_{swl} \sim \frac{3}{8} \gamma H_b. \quad (5)$$

Numerous experiments have tested this result. *Bowen et al.*'s laboratory experiments verified these relationships under conditions that closely met the assumptions. However, they and other researchers [*Holman and Sallenger*, 1985; *Holland, et al.*, 1995] have found that setup is greater than predicted as the value of $(h + \bar{\eta})$ becomes small. Also, the wave height saturation parameter, γ, depends strongly on other parameters (e.g. the beach slope: [*Sallenger and Holman*, 1985; *Sallenger and Howd*, 1989; *Haines and Sallenger*, 1994]). Not surprisingly, observed values of γ as well as $\frac{\bar{\eta}}{H_b}$ from published field experiments vary widely. Table II.1 cites some of the published values, as well as the effective observation depth ($(h + \bar{\eta})_{obs}$), and the general form of the beach (barred or planar). In all cases presented in Table II.1, H_b is actually the rms wave height observed at nearby wave gages (converted when the significant wave height, H_s, was published via $H_b = \frac{H_s}{\sqrt{2}}$). Only *Holland et al.* [1995] report the swash zone variation of $\bar{\eta}$ in the field.

6.2.2. Breaking waves over a sand bar

On a plane beach, the depth of maximum dissipation increases indefinitely as the incident wave height increases. However, on a barred beach, the incident wave height near the shoreline tends to be limited by breaking over the bar. The relevant wave height at the shoreline is that which survives past the bar. Assuming depth saturation of the wave height over the bar crest, we expect that wave heights at the shore are limited to

$$H_{shore}(t) = \begin{cases} \gamma\, h_{bar}(t); & \text{for } H_b(t) \geq \gamma\, h_{bar}(t) \\ H_b(t); & \text{otherwise} \end{cases}, \qquad (6)$$

where h_{bar} is the water depth over the bar, which varies over the tidal cycle or when the bar crest moves onshore or offshore. Thus, the wave height seen at or near the shoreline should have a strong tidal signal on a barred beach. This is not the case on a plane beach.

6.2.3. Consistency test

For this particular part of the field comparison, the swash motions under the limited wave height near the shore likely remain reflective (i.e. $\xi > 1$, if ξ were defined using a wave height shoreward of the bar). We would expect that equation 3 (reflective model) would still hold locally, as long as we could supply the correct local wave height, which is H_{shore}. If the setup term can be modeled as a function of the breaking wave height, then both these effects are combined in the following model:

$$\Delta z(t) = \alpha_o + \alpha_{shore}\, H_{shore}(t) + \alpha_b\, H_b(t) + \varepsilon(t). \qquad (7)$$

Inspection of equation 6, noting that $h_{bar} = z_{tide} - z_{bar}$, indicates that the equivalent equation with the tide level and sand bar crest elevation as parameters is

$$\Delta z(t) = c_o + c_1 z_{tide}(t) + c_2 z_{bar}(t) + c_3 H_b(t) + \varepsilon(t). \quad (8)$$

The coefficients in equation 7 are related to those in equation 8 as follows:

$$\alpha_o = c_o, \quad (9)$$

$$\alpha_{shore} = \frac{c_1}{\gamma} = \frac{-c_2}{\gamma}, \quad (10)$$

and

$$\alpha_b = c_3. \quad (11)$$

Equation 8 allows us to test whether all of the measured variables (H_b, z_{tide}, z_{bar}) contribute to the observed deviations. We expect that α_o is negligible, while equation 10 provides a compatibility constraint (i.e. if $c_1 \neq -c_2$, the variables are involved in ways that we had not expected). Including bar crest elevations estimated from daily CRAB surveys, we estimated the coefficients in equation 8 using a linear regression, which was significant at the 95% level (R^2=0.8, R^2_{crit}=0.16, c_o=0.02±0.47, c_1=0.25±0.18, c_2=-0.19±0.17, c_3=-0.24±0.06). Further, we verified that all of the observed variables contributed significantly to a stepwise regression, by adding successive variables to the regression and checking that the increase in skill (R^2) of the model was greater than the corresponding increase due to an uncorrelated random variable. Casting the results as terms in equation 7, α_{shore}=0.44±0.34 ($\gamma = \frac{1}{2}$), α_b=-0.24±0.06, and α_o is negligible. This relationship is shown in Figure 10c. Additionally, we used the data from the 2 m pressure gage (inner

surfzone) to characterize H_{shore} for the dissipative regime. The linear regression (equation 7) results (R^2=0.7, R^2_{crit}=0.14, α_{shore}=0.40±0.30, and α_b=-0.29±0.08) are consistent with the above analysis, and equation 10 is compatible within the confidence limits on the regression parameters.

In summary, on a barred beach the role of H_{shore} in the $\xi<1$ case is apparently identical to the role of H_b in the $\xi>1$ case. During dissipative conditions, Δz is actually limited by the compensating effects of setup. Apparently, the factors controlling the SLIM position are fundamentally different at the onset of breaking over the bar. We conclude that the observed behavior of the SLIM bathymetry estimator is consistent with our expectations.

6.3. Beach cusps

A further sub-division of the data was made to investigate the effect of beach cusps. Figure 11a shows an example of a SLIM line that has the same alongshore rhythmicity as the beach cusp field, but the displacement sense is opposite to that of the beach contours. The magnitude of the cusp-scale variations of this estimated contour is also exaggerated relative to the measured contours. Thus, cusp presence is easily identified in the displacement of the SLIM line, but the relationship to the bathymetry is complicated. The cusp bathymetry interacts with the incident waves, influencing the intensity patterns [*Holland, et al.*, 1995]. This sort of complication is beyond the scope of consideration in this paper.

6.4. Other alongshore trends

There were several examples where the bathymetry estimate errors were related to alongshore variation of the bathymetry when cusps were not present. Figure 11b shows an example of this. In this case, the SLIM line descended from y=850 to y=1000 as the swash zone bathymetry flattened from north to south. Note that the alongshore variation of beach slope was reversed above the 1 m contour (near an erosional scarp) compared to below the 1 m contour. This complicated shoreline bathymetry co-existed with alongshore variations in the cross-shore position of the sand bar.

7. Error correction and reduction

7.1. Spatial averaging

The fact that short scale, alongshore variations of the intertidal bathymetry are not well resolved with this technique (Figure 11a) suggested that the SLIM bathymetry estimator can only resolve an alongshore-smoothed version of the true bathymetry. Also, Figure 7 shows that there is considerable scatter of the raw bathymetry estimates about the best-fit linear profile. As a result of these two error sources, a more reliable estimator of the true bathymetry results if the data are used to constrain a simple beach surface model. For example, we can model the SLIM bathymetry estimates, z_{slim}, as:

$$z_{slim}(x,y) = \beta_X (x - X_O) + \beta_Y (y - \overline{y}) + \varepsilon(x,y). \qquad (12)$$

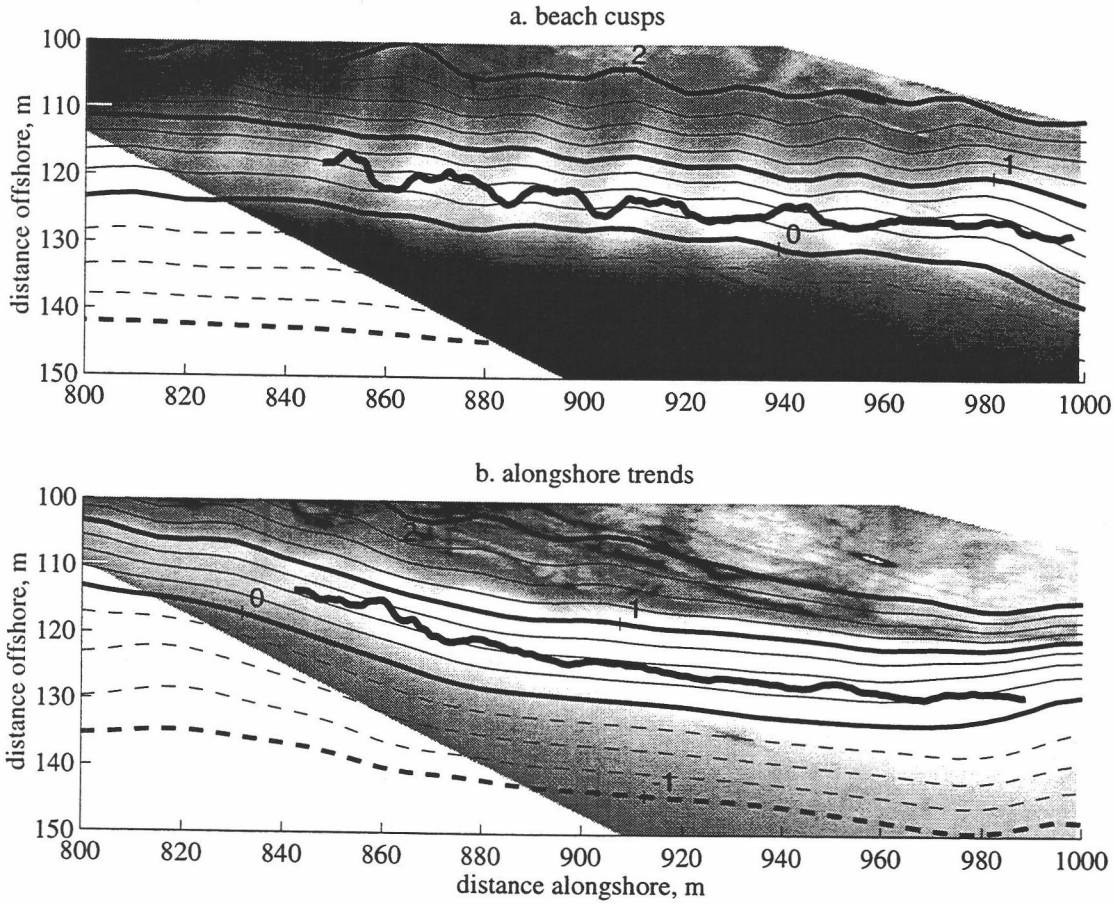

Figure II.11. Two planview images with superimposed beach elevation contours show (a) deviations related to beach cusps (on 21 October) and (b) deviations due to alongshore trends in the bathymetry (on 18 August). The heavy line is the SLIM line identified for each image. The contour interval is 0.25 m and negative contours are dashed.

The cross-shore and alongshore beach slope components, β_x, β_y, and mean sea level (MSL) intercept , X_o, describe the estimated beach surface on each day. The mean alongshore position, $\overline{y}$, does not change given uniform sampling.

A simple analysis of the length scale of alongshore variability of the SLIM position (or variability of time-averaged intensity along the SLIM line) determined an appropriate smoothing scale for this field study to be at least 50 m. As an example, the model

parameters (β_X, β_y, X_O) were estimated with a linear regression within a region bounded by $900 \leq y \leq 950$ m, and $-1 \leq z \leq 1$. The model elevations were then calculated at the same horizontal locations as the original DGPS data and compared to these control data (the control data were not interpolated). The daily mean deviations between the model and control data are shown in Figure 12a. The mean deviation over all days was 0.20 m, which is unchanged from the deviation of the individual data. The standard deviation of the model error was 0.10 m (compared to 0.14 for a single profile). The variability of the model deviations calculated over each day show the most reduction in error -- the daily standard deviation of the elevation differences was 0.08 m, on average.

The DGPS survey data were then used to constrain the model parameters so that estimates of beach slopes made by the two surveying methods could be compared. The daily SLIM-based cross-shore slope estimates tended to underestimate the DGPS beach slopes by 10%, on average (Figure II.12b), and the average 95% confidence intervals about the slope were ±0.01 (also reduced relative to a single profile) or about 10% of the mean slope. The alongshore slope component (Figure 12c) was almost always accurately estimated (confidence intervals were ±0.003). The difference between the MSL intercepts estimated by the two techniques (Figure 12d) was 2.78 m on average, which was significant (due to the systematic offset) compared to average confidence intervals of ±1.01 m.

In the 50 m wide (alongshore) sub-area the number of SLIM observations (up to 8000 per day) were always several orders of magnitude higher than the number of DGPS samples (~ 40 per day) and the SLIM observations were not necessarily independent, since we sampled every 0.25 m alongshore. To estimate the confidence intervals about the regression parameters, the number of independent estimates (degrees of freedom) was assumed to equal the number of DGPS observations. The confidence intervals about the estimated model parameters depend only on the regression quality; therefore, they provide

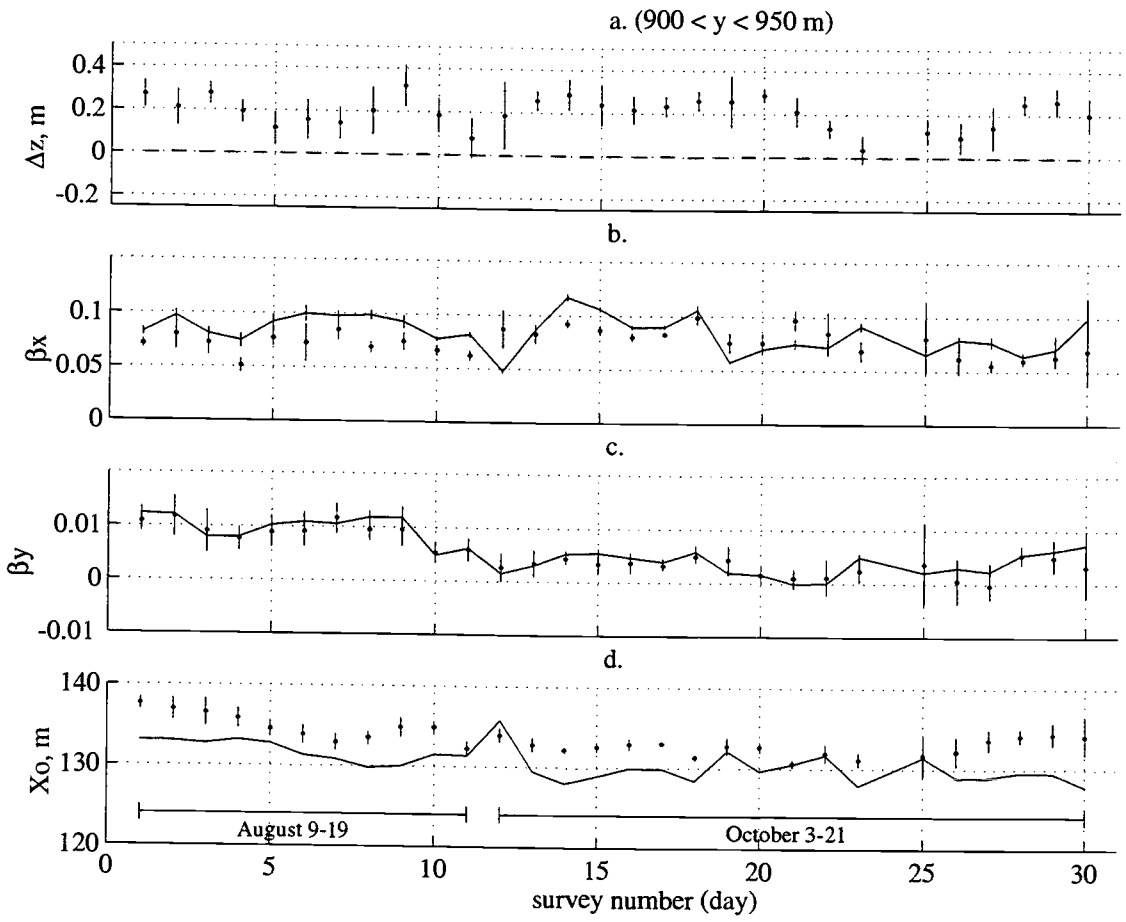

Figure II.12. (a) Time series of daily mean elevation difference between plane beach model (equation 12 constrained with corrected SLIM elevations) and DGPS elevations, averaged over each day and over 50 m alongshore. Error bars are standard deviations. Cross-shore (b) and alongshore (c) slope parameters and MSL intercept (d) are estimated from both DGPS data (solid lines) and raw SLIM data. 95% confidence limits are plotted as error bars about SLIM estimates.

an assessment of the data quality (precision, not accuracy) that is independent of the surveyed control data. In Figure 12, data were plotted only if the estimated cross-shore beach slopes differed significantly from zero slope. In general, increasing wave height led to increasing confidence intervals.

7.2. Temporal averaging

There is very simple statistical formulation for error reduction based on the difference between the morphological response time and the wave field response time. Averaging, for example, daily estimates of the beach slope over a time period with considerable variation of the wave height, but little morphological response will reduce the measurement error due rapid fluctuations in the wave field, as long as the true temporal variance of the beach is much less than the "noise" variance. As an example, the beach slope varied little over the study period and the average SLIM estimate was not different (at the 95% level) from the averaged DGPS-surveyed beach slope.

7.3. Dynamics-based, ground-truthed correction

It is possible that at some sites there may be enough supporting data to calibrate a correction model based on the dynamics discussed earlier. For example, at Duck there are permanent, multiple wave gages across the surf zone and bi-weekly beach surveys. Then, the video technique could be used to increase the bathymetric survey frequency and spatial resolution. Here, we present SLIM bathymetry estimates that have been empirically corrected. The corrections to the SLIM data used equations 3 and 7, where absence/presence of breaking over the bar (easily identified in time exposures) was used to identify data consistent with Case I or Case II. Since this is a barred beach, we assumed that the swash zone was always reflective. This correction reduced the rms error over all of the data from 0.24 m to 0.11 m. Less than one quarter of the data were used in the calibrations (equations 3 and 7) yet the corrected estimates do well on nearly all data.

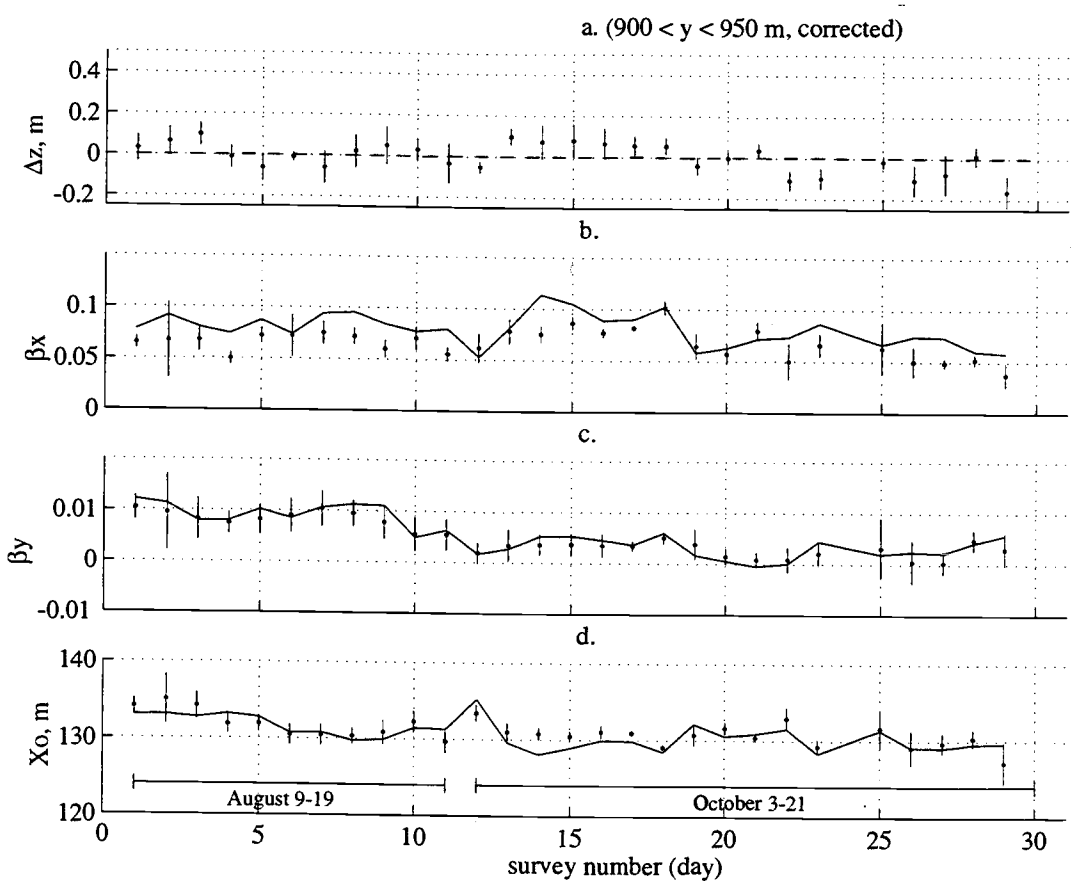

Figure II.13. Same as Figure II.12, but corrected (equations 3 and 7) SLIM elevations were used.

Again, the model parameters (βx, βy, X_O) were estimated with a linear regression within a region bounded by $900 \leq y \leq 950$ m, and $-1 \leq z \leq 1$. The rms model deviation (Figure 13a) over all days was 0.06 m, which is comparable to the DGPS control data variability (0.05 m)! Still, the daily SLIM cross-shore slope estimates tended to underestimate the DGPS beach slopes by 10%, on average (Figure 13b), and the average 95% confidence intervals about the slope were ± 0.01 or about 10% of the mean slope. Again, the alongshore slope component (Figure 13c) was accurately estimated. The difference between the MSL intercepts estimated by the two techniques (Figure 13d) was 0.4 m on average, which was not significant compared to average confidence intervals of

±1.3 m. The SLIM- and DGPS-based time series (β_x, β_y, X_o) were significantly correlated over the study period (R^2 values were 0.5, 0.9, and 0.6, where $R^2_{crit} = 0.2$ at the 95% level, using 28 observations). This type of empirical correction improved the cross-shore slope estimates considerably by reducing the systematic errors.

7.4. Normalized error magnitudes

In our field comparison, 88% of the spatial and temporal variance of the beach elevation was recovered (Figure 6a) even if the systematic errors were ignored. However, estimates of the beach slope using the raw SLIM data resolved a small percentage of the time variability of the true slope. Our ability to estimate bathymetry, or its variance, depends on the ratio of measurement error variance to the true variance. If the error variance is relatively small, we stand a good chance of recovering much of the true bathymetric variability. Since we now have some ability to predict the estimation errors, we can easily determine the minimum level of "signal" that can be resolved above the "noise" level.

We treat the problem of estimating the beach slope assuming that all errors are random and the error variance is known. Then, confidence intervals about estimated parameters indicate the "noise" level of the observations. For example, it is possible to resolve the beach slope (distinguish it from zero slope) if $\frac{\beta}{\beta_{ci}} > 1$. Here, β_{ci} is the confidence interval on the cross-shore slope estimates using a plane beach model. At the 95% level, $\beta_{ci} \sim \frac{\sigma_\varepsilon \beta\, 2.5}{\sigma_{tide} \sqrt{N}}$ [*Jenkins and Watts*, 1969] where σ^2_ε is the error variance of the plane beach model, β is the beach slope, σ^2_{tide} is the tidal elevation variance, and N is the number of (independent) estimates. Typical values for this study of, say, σ_ε=0.1, σ_{tide}=1, and N=16 (2 samples per hour over an 8 our period), yield $\frac{\beta}{\beta_{ci}} = 16$. Even if measurement

errors at a site are large, they can be compensated by an increased tidal variance, increased sample rate, or decreased beach slope.

8. Discussion

The aim of this paper was to describe and test a seemingly simple method of measuring bathymetry and bathymetric change within the intertidal region of any beach that could be viewed with a camera. The factors which contributed to measurement errors include the nearshore morphology (e.g. plane beach or barred beach) and resulting nearshore dynamics. The ability of the technique to make useful measurements of intertidal bathymetry depends on the ratio of the measurement errors to the spatial or temporal variability of the beach itself. In a field comparison, the behavior of the measurement errors was consistent with simple theoretical models, which included the effects of wave energy dissipation at the shoreline and over sand bars and setup. However, neither setup nor swash heights were measured directly. It is possible that other mechanisms could yield similar relationships to those considered in this paper. For instance, the depth at the SLIM location could be related to infragravity oscillations, which can dominate the swash spectrum during high energy conditions [*Guza and Thornton*, 1985]. An extreme example of this type of error might occur at sites with large tidal ranges. Over the period required to obtain a time exposure, the tidal level could change enough to smear an otherwise narrow region of shore break (this effect was not significant at Duck). Other potential sources of error that we neglected to include were rapid changes in the actual bathymetry (SLIM and DGPS control data were not collected synchronously), persistent foam (a problem noted by LH89), wind-induced setup, errors in the photogrammetry (e.g. random errors increase with range from the camera), and complicated cross-shore structure of the intertidal beach profile. The relevant parameters needed to test these other systematic error sources were not measured and their effects can not be evaluated here. Clearly, more attempts at modeling the

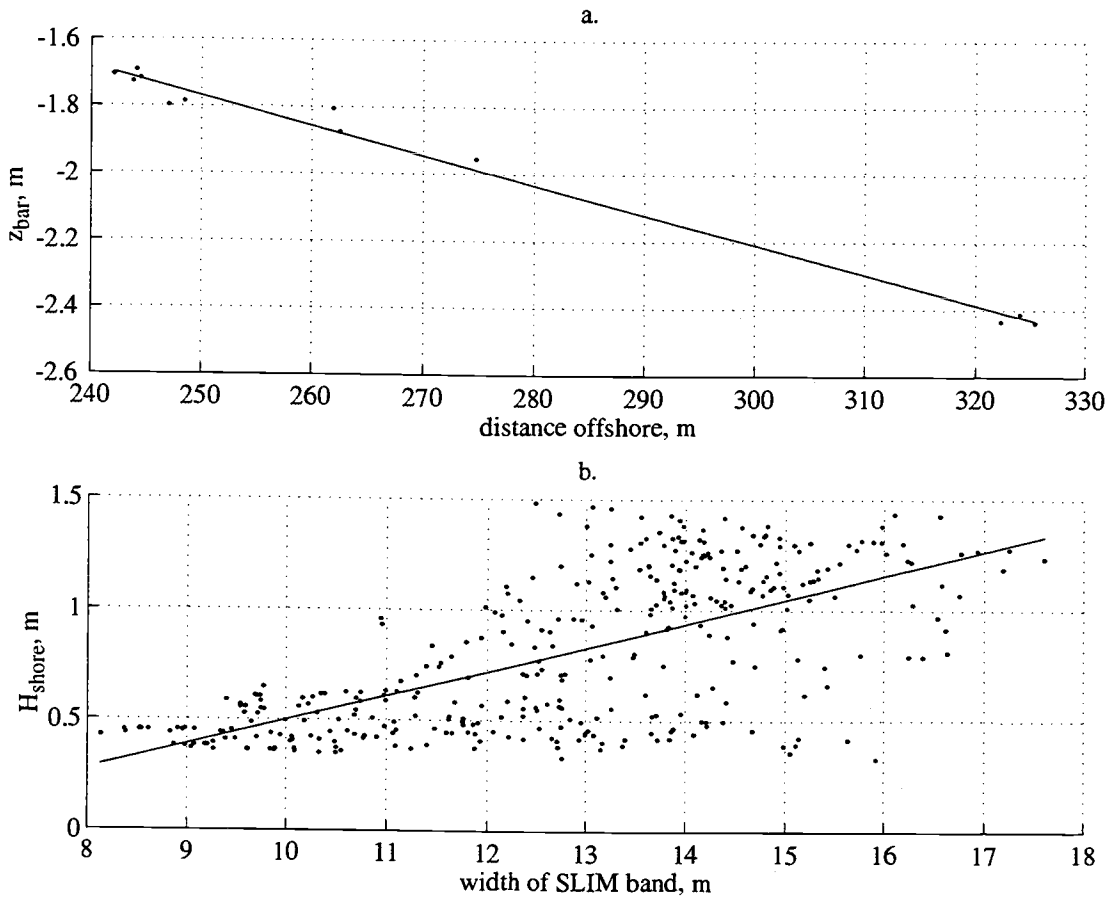

Figure II.14. (a) The measured sand bar crest elevation is linearly related to the bar crest's cross-shore position, along a single profile (y=950 m) surveyed by the CRAB. (b) The width of the shoreline intensity maximum band is related to the wave height near the shore.

relationships between fluid processes and the observed time-averaged intensities must be done before we can better tease apart the contribution of each process to observation errors.

We found that the presence of sand bars had a positive effect on this technique. Because wave heights at the shoreline tend to be limited by the water depth over the sand bar, a shoreline intensity maximum will always exist fairly near to the actual SWL shoreline. In contrast, on a plane beach the intensity maximum would continue to move to water depths that are proportional to the incident wave height (a result predicted by the dissipation model,

even including setup). Unless a particular beach is truly planar, the SLIM bathymetry estimates will tend to be increasingly uncorrelated to the SWL bathymetry. If faced with this situation, an obvious means of limiting the error magnitude would be to limit the analysis to images corresponding to relatively low wave heights.

On barred beaches, the elevation of the inner most bar crest or the wave height shoreward of this sand bar was strongly correlated to the systematic deviations encountered with the SLIM bathymetry estimates. We can suggest two methods to obtain this information remotely so that it could be used in an empirical correction scheme. One method is to develop statistics that relate the elevation of the sand bar crest to its cross-shore position, which can be located in time exposures (LH89). Figure 14a shows this relationship for the time period of this study, where variations of the bar crest elevation were proportional to 0.01 ($\pm$0.005, $R^2 = 0.99$) times the variations in the bar crest position.

Another approach is based on the relative width of the SLIM band, which is likely proportional to the swash excursion and, thus, swash height. Figure 14b shows the dependence of H_{shore} (equation 6) on the SLIM width. Either (or both) of these image-based parameters could be incorporated into the present technique. It is also likely that the wave height at the shore could be estimated from an intensity profile extending to the seaward most break point. Assuming that the reduction in wave height from its offshore value is related to the integral of the intensity (consistent with the dissipation argument of LH89), the wave height near the shore could be estimated. We did not investigate this approach.

The SLIM bathymetry estimator error (bias) depends both on the wave climate as well as the morphological features of a particular beach. What happens if the morphology changes significantly, as is the situation for all beaches that we wish to study? A particular example is a seasonally-barred beach, which may be a nearly plane beach in the summer

months and barred in the winter. If there are no supplementary data with which one could tune an empirical correction scheme, large, seasonal variations in the estimate errors would get mapped into actual seasonal variation of the beach itself. Again, a solution to this problem would be to limit the error magnitude simply by analyzing images only when the expected errors are relatively small, probably corresponding to relatively low wave heights.

9. Conclusions

We have presented a technique using time exposure images and tidal elevation measurements to estimate beach bathymetry in the intertidal zone. This technique relies on simple photogrammetric relationships to map proxies for the still water level shoreline from digital images to beach elevation contours. The proxy that we used (the shoreline intensity maximum) does not correspond exactly to the still water level. However, a field comparison between estimated elevations and accurately surveyed beach elevations showed that discrepancies are dependent on the dynamic conditions at the shoreline and, at least qualitatively, the relationships are predictable. The parameters that determine the behavior of estimate errors are also related to the morphologic setting. The simplest situation was that of a relatively reflective, plane beach profile since the discrepancy between the estimated and true bathymetry simply scaled with wave height. Although a barred profile introduces many complications, wave height limitation due to breaking over the minimum water depth of the bar crest tends to limit the maximum error between the location of the shoreline intensity maximum and the still water level shoreline. Thus, on barred beaches, reasonably planar intertidal profiles are estimated well over a range of wave heights. For all types of bathymetry, the smallest errors result from wave heights which break just enough to be visually observed.

Video-based bathymetry data were used very effectively to constrain a plane beach surface model that damped cusp-scale variations. This approach provided a simple method to suppress short scale, alongshore variability, which was not resolved well with this technique. Conveniently, at large ranges from the camera location, short scale variability is suppressed by the coarsening of image pixel resolution.

The advantages of the present "surveying" technique are that it samples a wide variety of alongshore length scales over long sample periods, sampled daily. The sampling is done objectively, using an image processing system and a straightforward feature recognition algorithm. The measurement error for individual shoreline estimates on the steeply sloping beach used in a field comparison was about 0.10 m (in the vertical). Estimates of the cross-shore component of the beach slope were made accurately to within 10% of the mean slope and the cross-shore position of the mean water level could be estimated to within 1 m, on average. Thus, this technique is appropriate for sampling over time periods where changes in the beach surface exceed these error levels. For instance, beach elevation changes on the order of a meter (equal to the tidal range) are resolved well. This video-based sampling technique will be used to collect long time series of intertidal beach surface variations from remotely operated cameras currently located on the U.S. coasts of Oregon, North Carolina, Hawaii, California, and the Great Lakes as well as in the Netherlands, Australia, and the United Kingdom. These observations will certainly reveal unique and interesting beach behavior.

CHAPTER III: INTERANNUAL SHORELINE VARIATIONS AT DUCK, NC, USA

1. Abstract

We have analyzed 3 years of daily observations of the shoreline position along a 2 km segment of the coast at Duck, NC. Shoreline variations were found to be dominated by length scales of order 1 kilometer, with an amplitude that was modulated by a seasonal cycle, and a spatial structure that progressed alongshore at an average rate of 1 m/day. Surprisingly, the alongshore-averaged shoreline position did not display an annual cycle. Instead, the most pronounced alongshore-averaged shoreline changes occurred over several years. The dominance of large spatial and temporal scales suggests that short scale studies at Duck (typical duration < 1 month and lengths < 500 m) seriously under-resolve an important component of shoreline variability.

2. Introduction

To describe general beach behavior, we have often referred to a "summer-winter" conceptual model [*Komar*, 1974], in which beaches erode and sand bars form or move offshore during large storms (winter), followed by beach accretion and onshore bar movement during calm periods (summer). Recently, however, observations of nearshore bathymetry have revealed interannual and decadal morphologic behavior, which are not described by a seasonal model. Examples include offshore progressive sand bars at Duck, NC, USA [*Birkemeier*, 1985; *Lippmann and Holman*, 1990; *Larson and Kraus*, 1992] and along the Holland Coast [*Ruessink and Kroon*, 1994; *Wijnberg and Terwindt*, 1995] over periods of several years to over a decade. In addition, there is evidence that beach response over these long time periods is not alongshore-uniform. *Wijnberg and Terwindt* [1995] showed examples of alongshore progressive variations at the shoreline, with an alongshore

wavelength of about 2 km and periodicity matching that of the bars. It is appears likely that, with increasing time scales, beach variability may be dominated by large length scales. Quantifying the contribution of various alongshore length scales to beach variability, and determining characteristic time scales associated with each length scale are clearly important to understanding (or simply describing) the long term behavior of beaches.

In this paper, we focus on the behavior of a particular beach elevation contour near the shoreline at Duck, NC. One reason to focus on the shoreline is that it delineates the width of the subaerial beach, which is of practical significance to those who live on or visit the beach. Also, the shoreline is a morphologically active (and therefore interesting) region of the beach, which responds to variations in wave conditions, tides, and (perhaps) interannual forcing. We seek to determine the relative contribution of different length scales to shoreline variability, and to describe the relationships between length and time scales. First, we will describe observations of the cross-shore position of a particular shoreline contour, obtained from analysis of video images. Then, we will present an analysis of the spatial and temporal variability of this data set. Since the dominant variability is associated with large length scales, we quantify this variability by focusing on two scales: (1) the alongshore-averaged shoreline position and (2) variability with a wavelength of about 1 km. The observed variability is partitioned into amplitude time series for both scales, as well as a time series of the spatial phase shift of the 1 km scale, which describes alongshore propagation. Finally, we describe the correlation between the shoreline variability and the wave field.

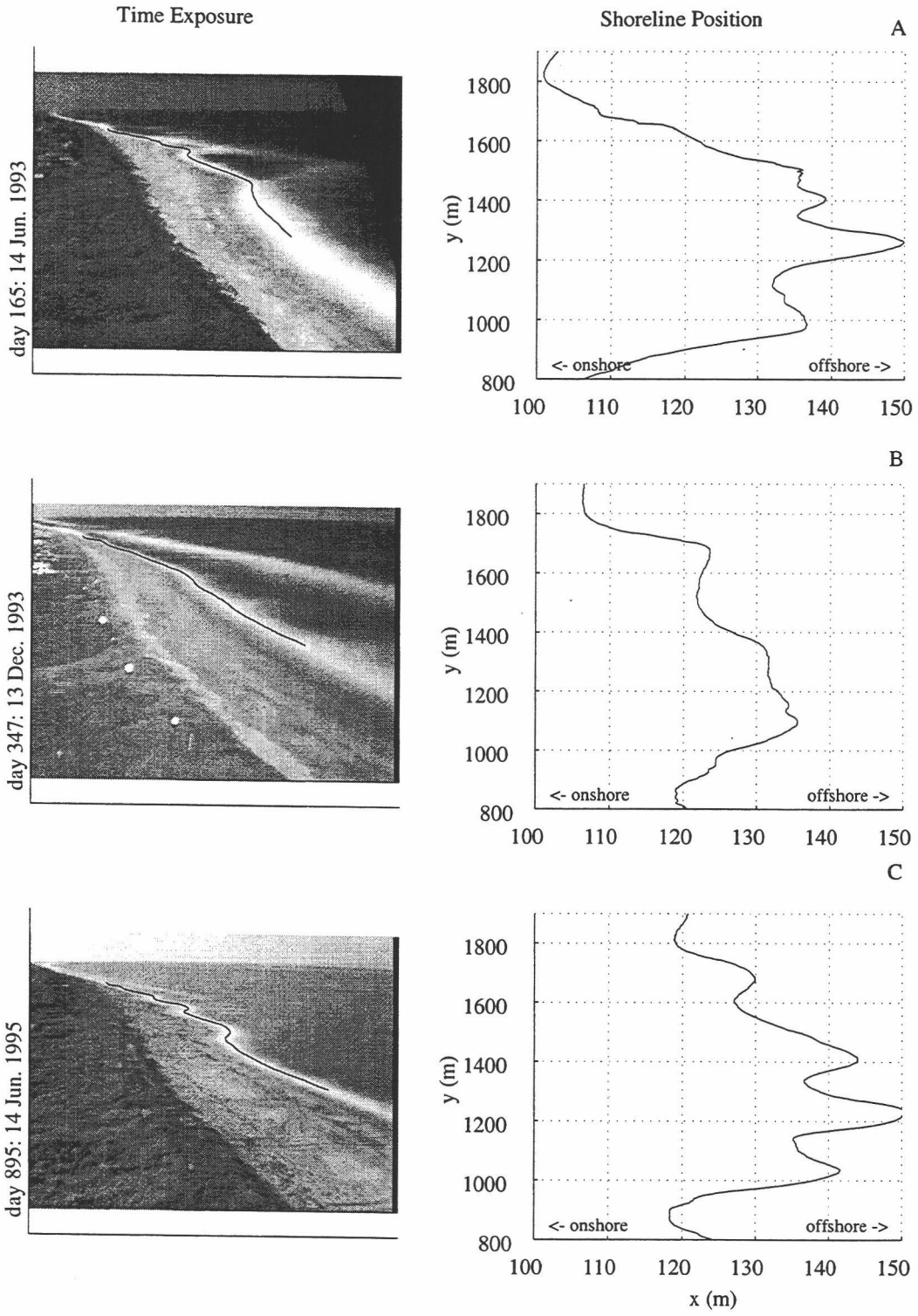

Figure III.1. Examples of time exposure images, from Duck, NC. The location of the shoreline intensity maximum (SLIM) line is identified on each image and the map projection of that line is shown adjacent to each image. On the map projection, the ordinate is the alongshore range; positive is to the north (away from the camera). The cross-shore scale is exaggerated.

3. Data collection

Video images of the surf zone at Duck, NC have been collected since 1986. Originally, the images were obtained once per day; however, they have been obtained every hour since 1993. The type of images that we will use in this study are time exposures [*Lippmann and Holman*, 1989; *Lippmann and Holman*, 1990]. A time exposure (Figure III.1) represents the average image brightness over, in this case, a 10 minute period. In relatively shallow regions where waves tend to break (e.g. over sand bars and at the shoreline), the average brightness is relatively high (white) due to the persistent production of foam, hence, morphologic features are often easily identified. At Duck, time exposures have been used successfully to locate the position of sand bars as well as the shoreline [*Lippmann and Holman*, 1989; *Lippmann and Holman*, 1990].

Plant and Holman [1997] described the methods that we used to locate and map the shoreline position. To summarize: we assumed that the shore-parallel band of high image intensity at the shoreline, also called the shoreline intensity maximum (SLIM), visually marked the still water level shoreline. The SLIM was identified in each image and its cross-shore position at a series of alongshore sample locations was determined from simple photogrammetric relationships [*Lippmann and Holman*, 1989]. Since the cross-shore position of the SLIM varied with tidal elevation, we selected images corresponding to tidal elevations within 0.25 m of the 0.50 m level. We attempted to locate the shoreline once per day, within a 2 km long region, sampling every 2 m. The shoreline position is overlain on each image in Figure III.1, and is plotted in map coordinates on the adjacent panels.

This shoreline estimation technique ought to be most accurate when applied to simple intertidal bathymetry (i.e. slowly varying in both alongshore and cross-shore directions) and when the wave height is low, so that the SLIM is a narrow band located near

to the still water shoreline. The beach slope and wave height at the shoreline scale the errors in the estimates of the cross-shore position of the shoreline. For a barred beach, the error is approximately $\frac{1}{2}\frac{H}{\beta}$, where H is the (potentially depth-limited) rms wave height shoreward of the sand bar and β is the beach slope at the shoreline. The intertidal beach slope at Duck is typically about 0.1 and the shoreline wave height is limited by breaking over the bar to 1.0 m, resulting in a maximum error of about 5 m. Finite resolution of the digital images also contributed to measurement errors that ranged from 0.50 m nearest to the camera to 2.0 m farthest from the camera. The alongshore resolution of the shoreline position estimates varied from 1 m to 50 m .

4. Results

Of the 980 days in the study period, 748 images fell within the desired tidal level range ($0.25 \leq \text{tide} \leq 0.75$). Due to problems with image quality (rain on the lens, fog, equipment failure, and very small wave heights that did not produce a SLIM), only 578 images yielded shoreline positions. Of these, some shoreline position estimates did not cover the entire 2 km sample region. Only 336 images yielded data fully spanning a 1 km subset of the sample region ($900 \text{ m} \leq y \leq 1900 \text{ m}$). This subregion was sampled at an average rate of about 1 sample/3 days. We will focus much of the analysis on the 1 km sub region.

4.1 Shoreline mean and variance

Over the 3 year study period, the observed shoreline position varied by as much as 45 m. The spatial structures of the shoreline and its variability are summarized by plots of the mean and standard deviation as a function of alongshore location, shown in Figure III.2. The mean shoreline position was not straight, but curved smoothly through the entire study

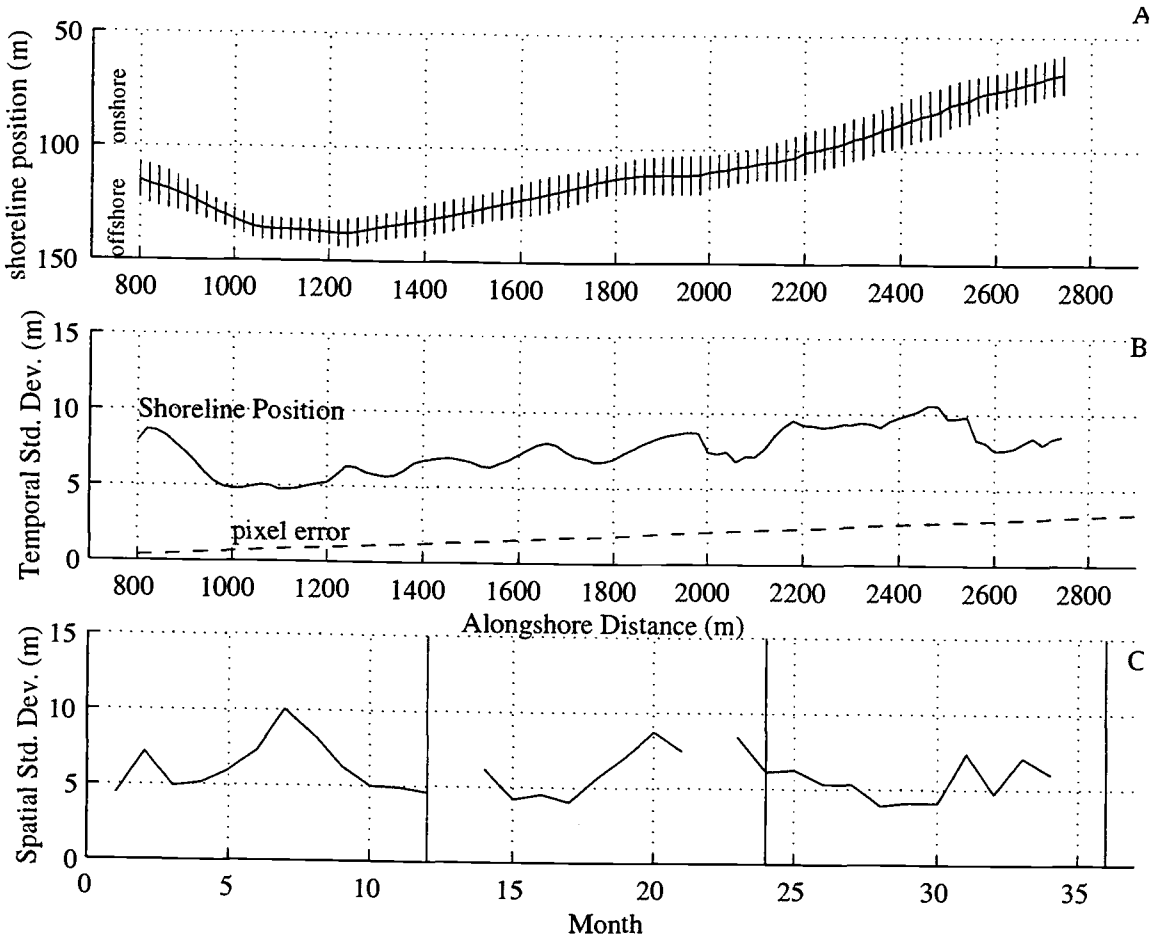

Figure III.2. Mean and standard deviation of the shoreline position. The time-averaged shoreline position is shown in the upper panel (A), where error bars are standard deviations. In the second panel (B), the standard deviation is plotted again, along with the cross-shore error due to the pixel footprint dimensions (dashed line). The third panel (C) shows monthly-averaged spatial variability. January of each year is marked by a vertical line.

area. The bend in the mean shoreline likely stems from geologic constraints. The temporal variability of the shoreline, indicated by its standard deviation, was not uniform either. The minimum variance occurred near the most seaward protrusion of the mean shoreline (y = 1100). The observed shoreline variance increased with distance from the camera, which may be due, in part, to the increasing size of the pixel footprint. The expected cross-shore pixel error is plotted for reference. Our choice of coordinate system was not shore-normal everywhere, which also contributed to increased apparent variability.

Time series of shoreline deviations were obtained by subtracting the mean shoreline position from each observation, at each alongshore location. The final panel in Figure III.2 shows the monthly-averaged, spatial variation from the mean shoreline position, as a function of time. In order to visualize the variation of the Duck shoreline, Figure III.3 displays low-pass-filtered deviations of the shoreline position at each alongshore location and each time. Positive deviations (light shades) indicate that the shoreline was seaward of its mean position. The low pass filter [*Ooyama*, 1987] damped variations with time scales less than 1-2 months, and interpolated missing data if the time gaps were shorter than the filter cutoff. The remaining missing data values are filled with hatching.

In Figure III.3, the most striking features are lineations that generally trend obliquely from the lower right towards the upper left (traveling toward the south) and have length scales of about 1 km. The behavior of these large scale features was not always characterized by simple southward propagation. For example, their direction reversed at times (e.g. day 200 to day 300). Also, shorter scales contributed to prominent coherent behavior. For example, between days 850 to 900, megacusps with approximately 200 m wavelengths were well developed. The megacusps appeared to propagate at the same speed as the large scale features. An annual cycle is not particularly apparent in Figure III.3. We turn now to quantitative descriptions of these shoreline deviations, partitioned into an alongshore-averaged component and a component with an alongshore length scale of 1 km.

4.2 Length scales

The contribution of different length scales to the observed shoreline variability was quantified using wavenumber spectra of the shoreline deviations. A discrete spectrum was estimated on each day, using data within the 1 km subregion, $900 \leq y \leq 1900$ m. Spectral

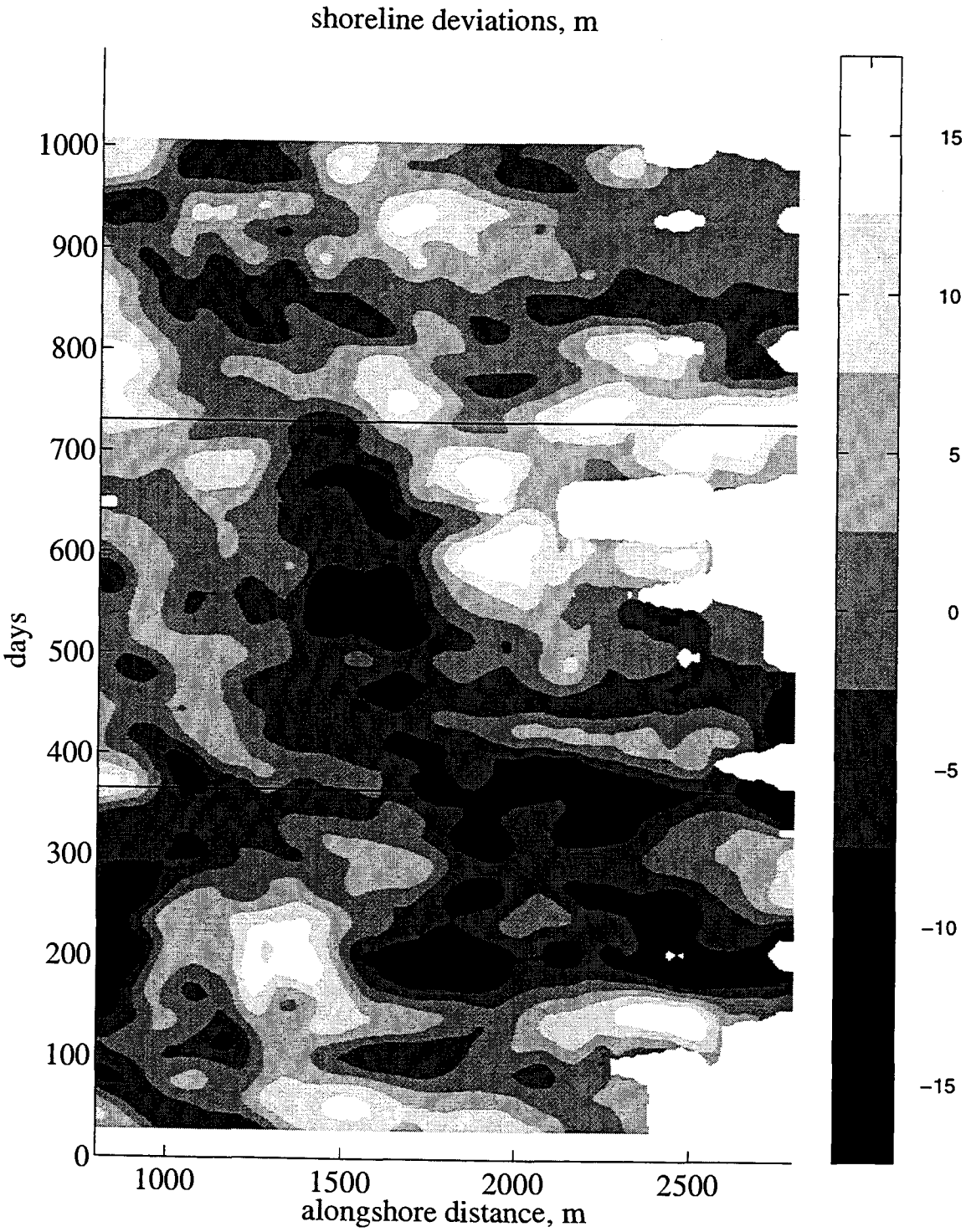

Figure III.3. Gray scale plot of shoreline deviations. The scale bar is in meters. Positive deviations (whiter) correspond to displacement of the shoreline seaward of it mean position. Missing data are filled by hatching, and January 01 of each year is marked by a horizontal line.

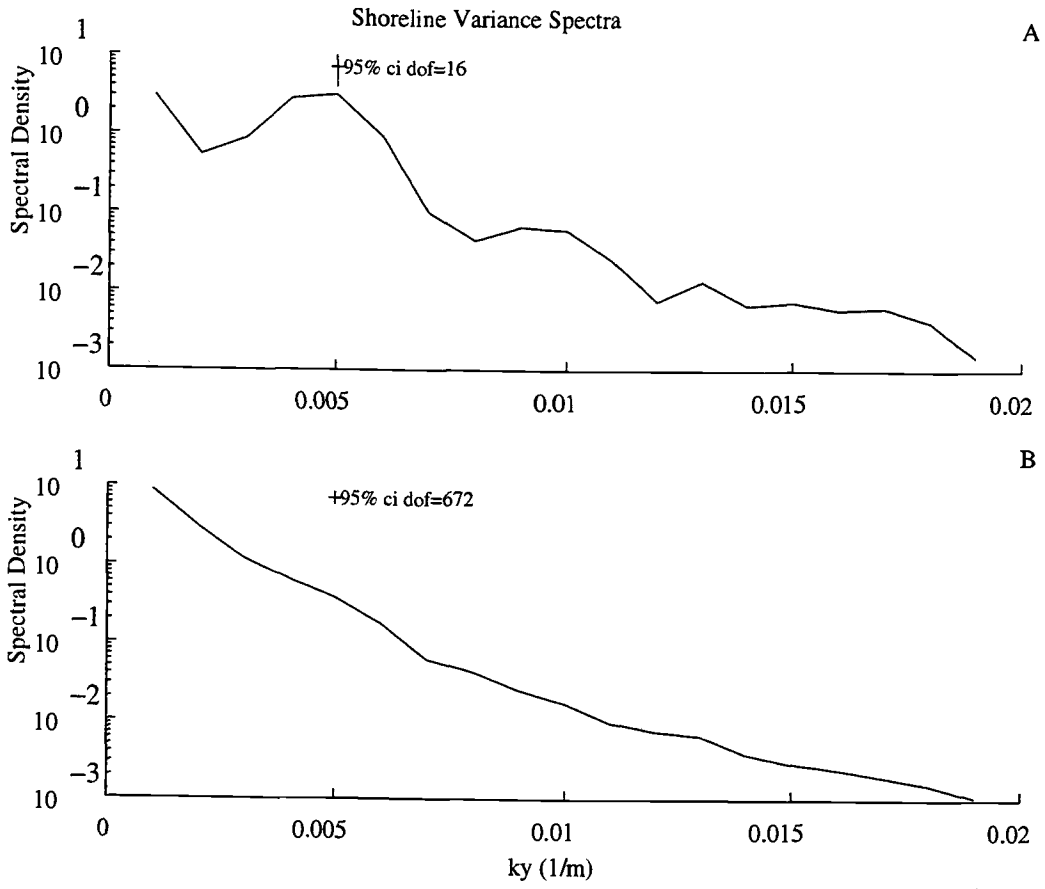

Figure III.4. Shoreline variance spectra as a function of alongshore wavenumber. The upper (A) panel shows sample spectral estimates averaged over a 34 day period (only 8 images) when megacusps were present with 200 m wavelengths. The lower panel (B) is the spectrum averaged over the entire 3 year study period.

estimates corresponded to the Fourier wavenumbers, $k_y = 0, \pm\frac{1}{1000}, \pm\frac{2}{1000}, \ldots,$ and $\frac{250}{1000}$ (m^{-1}). The alongshore-averaged shoreline position was removed at each time before estimating the spectra, and was the estimate of the first component, $k_y = 0$. The variance spectrum, $S(k_y)$, on any particular day describes the contribution of each length scale to the spatial variability on that day. As an example, we show several spectra, averaged over time to improve the reliability of the spectral estimates (Figure III.4). For instance, megacusps, which were obvious in the space-time map of deviations (days 850 to 900), also appeared as a well defined and significant spectral peak. However, the dominance of large length scales

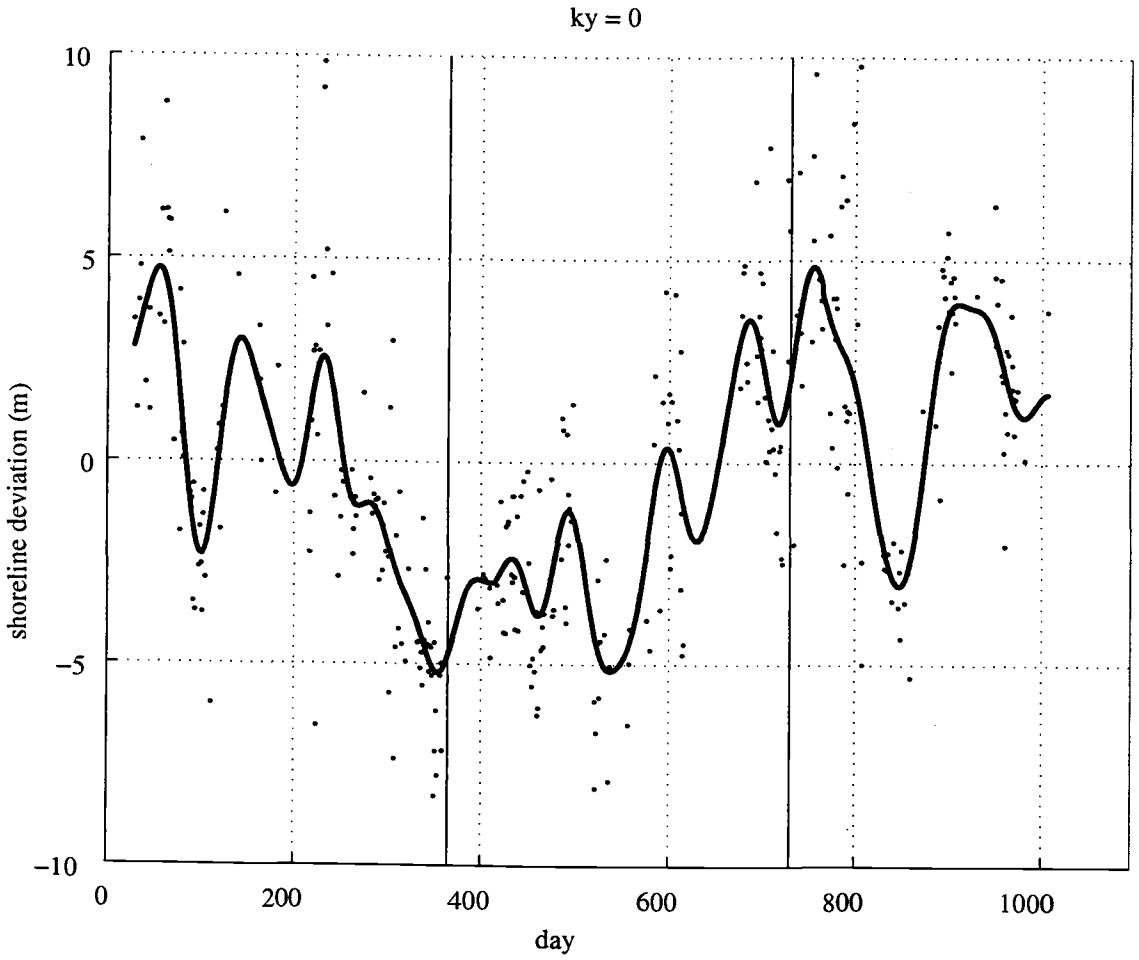

Figure III.5. Time series of the alongshore-averaged shoreline position over the 1 km subregion (900 m ≤ y ≤ 1900 m). The dots correspond to the actual samples, while the solid line is the filtered time series. January 01 is of each year is marked by a vertical line.

(low wavenumbers) was the most typical characteristic of these spectra. The spectrum averaged over the entire 3 year study period (Figure III.4B) emphasizes this point. In fact, the first two Fourier components, which are the alongshore-averaged shoreline position ($k_y = 0$) and the 1 km wavelength ($k_y = \frac{1}{1000}$ m^{-1}), explain nearly 80% of the total shoreline variance. We will focus the remaining analysis on these two components.

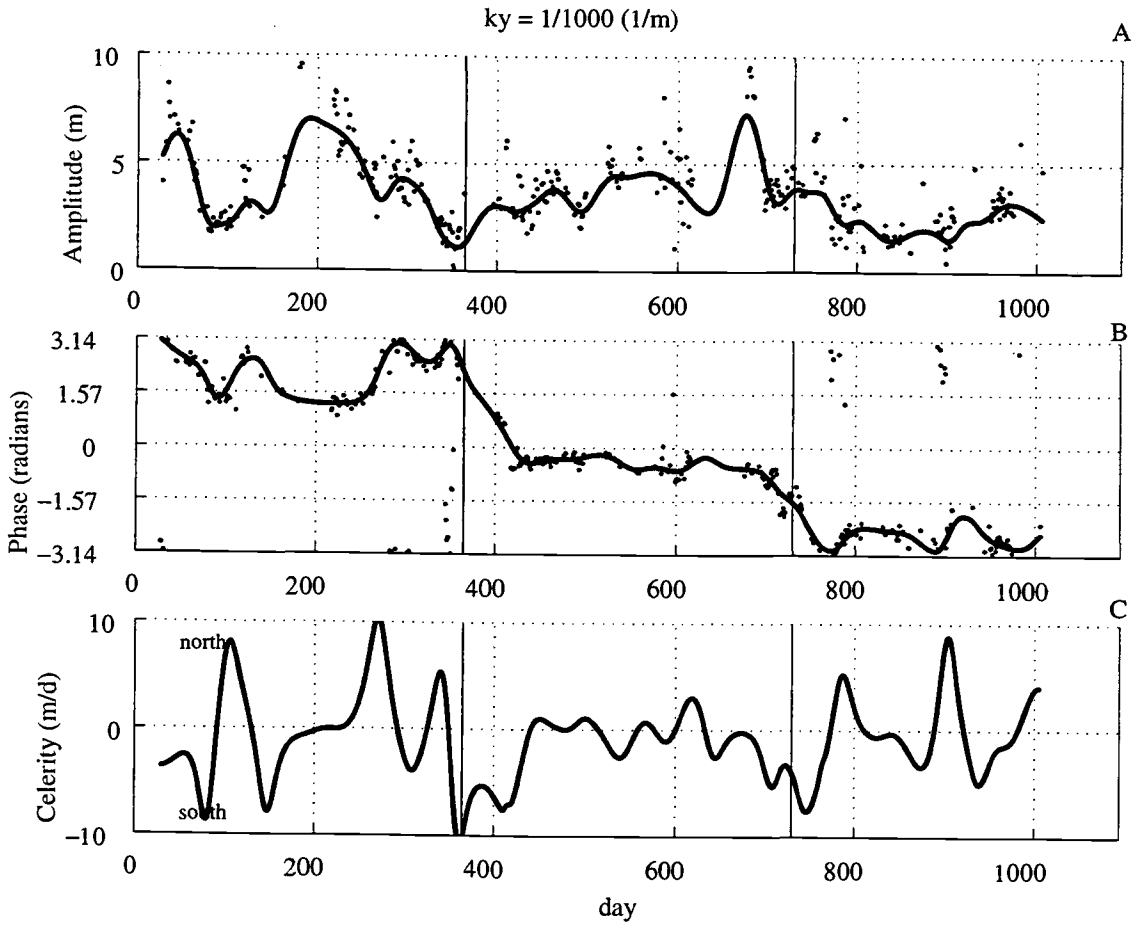

Figure III.6. Time series of the amplitude (A), phase (B), and celerity (C) of the 1 km wavelength component. The trend in the phase corresponds to an average alongshore celerity of -0.95 m/day (i.e., to the south).

Alongshore-averaged shoreline variability explained 36% of the total, observed shoreline variance. This component represented net onshore or offshore change of the shoreline (Figure III.5). Apparent, high frequency fluctuations due to measurement errors associated with rapid variation of the wave height were removed by filtering using a 30-60 day cutoff. The filtered time series of the alongshore-averaged shoreline deviations shows that dominant variability occurred over time periods greater than one year (inter-annual behavior). More rapid variations likely corresponded to storm/calm cycles. The absence of an annual cycle, as might be predicted with the summer/winter model, is conspicuous.

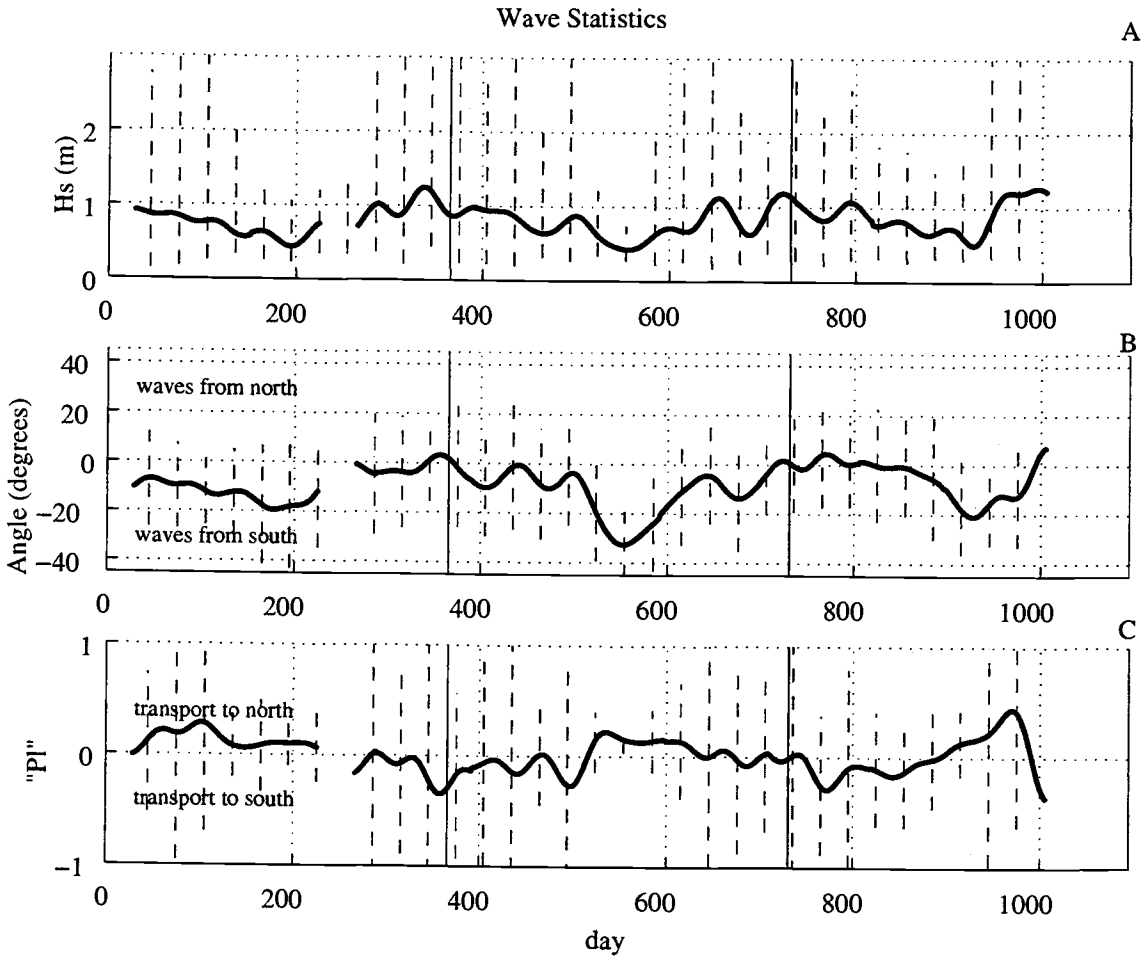

Figure III.7. Time series of significant wave height (upper panel), wave direction (middle panel), and alongshore wave energy flux (lower panel). Dashed lines show the monthly wave height range. Wave angles are relative to a shore-normal coordinate system, positive from the north, while a positive alongshore wave energy flux corresponds to expected sediment transport to the north. Dashed lines in the two lower panels correspond to monthly standard deviations.

The second component that we will consider corresponds to the 1 km wave length ($k_y = \frac{1}{1000}\ m^{-1}$), and accounted for 40% of the total shoreline variance. This component may be represented by time series of both amplitude, A, and phase, ϕ.

$$A(k_y,t) = \left| a(k_y,t) + i\, b(k_y,t) \right| \qquad (1)$$

and

$$\phi(k_y,t) = \mathrm{Tan}^{-1}[-b(k_y,t)/a(k_y,t)], \quad (2)$$

where $a(k_y,t)$ and $b(k_y,t)$ are the real and imaginary parts of the Fourier amplitudes. The amplitude time series had a strong annual cycle (Figure III.6). This is the quantitative representation of typical observations that the shoreline is relatively straight during the winter (largest waves) and develops increased alongshore variation during calmer periods, also evident in Figure III.2. The phase time series describes alongshore shifts of a coherent morphological structure. A simple phase ramp (constant slope) is indicative of a progressive wave form, while phase jumps of 180° suggest standing motions. The net phase shift over the study period corresponded to an average southward propagation of about 1 m/day. The estimated celerities are shown in the lower panel of Figure III.6. We expect the amplitude and celerity for this component to be correlated to wave height and direction.

4.3 Correlation to waves

We move now to determining how the two components of variability (ky = 0, $\frac{1}{1000}$ m^{-1}) were related to variations in the wave field. In particular, we expect that the amplitudes of the two components should be correlated to the wave height, while we expect that the alongshore propagation of morphologic features should be related to the product of the wave height and angle of incidence. The alongshore component of wave energy flux ($Pl \sim H_s^2 \mathrm{Sin}[-2\alpha]$) will be used to test this hypothesis. Figure III.7 shows a time series of the wave height, wave angle, and wave energy flux over the study period. The wave directions are relative to shore normal and positive wave angles correspond to waves approaching from the north, consequently driving sediment transport to the south. High frequency fluctuations dominate the wave time series, so time series were low-pass filtered with a 30-60 day filter cutoff. The filtered time series contain seasonal cycles in which wave heights tended to be high in the winter months and low in the summer months. Waves tended to approach from the north during winter and south during summer. Comparing the filtered

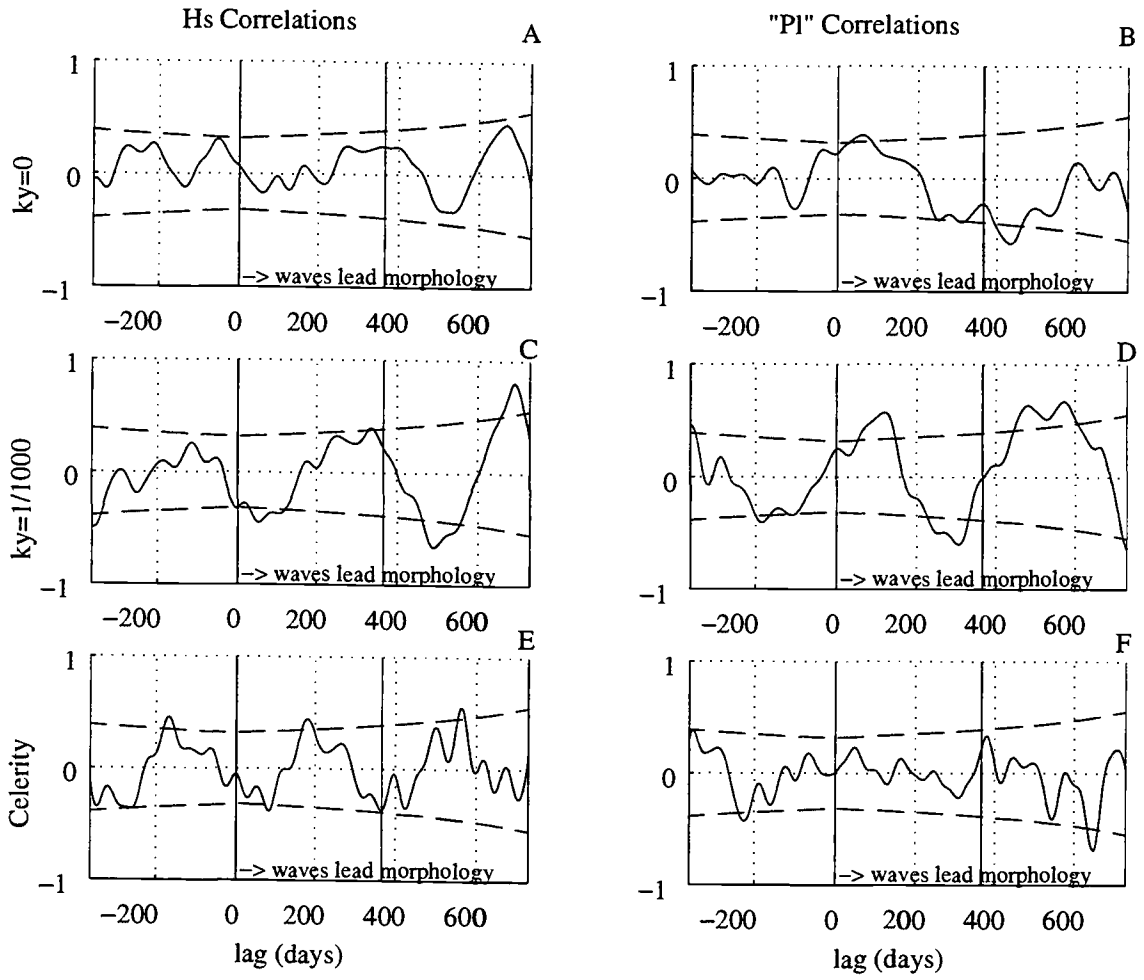

Figure III.8. Cross-correlations between wave parameters and morphologic parameters. The wave parameters (H_S and P*l*) are labeled at the top of the figure and the morphologic parameters (k_y=0, k_y=1/1000 amplitude, and celerity) are labeled to the left of each pair of figures. In each plot, dashed lines mark the 95% significance level of the correlation and vertical lines mark lags of ±1 year. Positive lags correspond to the wave time series leading the morphology.

wave time series to the filtered morphologic time series allows us to test for correlation between low-pass variations.

The time-lagged, cross-correlations between the morphologic time series and both wave height and the alongshore wave energy flux are shown in Figure III.8. The lag range

is defined such that positive lags correspond to the wave time series leading (forcing) the morphologic response. Time lags between -1 and +2 years are shown in all the correlation plots. The first panel shows the correlations between alongshore-averaged shoreline position and wave height, which were less than the 95% significance level at nearly all lags. In the adjacent panel, the correlation to the wave energy flux was most significant at a lag of about 60 days. The positive correlation suggests that periods of northward sediment transport lead to increased beach width. Both results are surprising, since we expected a correlation to wave height but did not expect the alongshore-averaged response to be a function of wave direction.

The cross-correlations of both the amplitude and celerity of the 1 km wavelength component with the wave parameters contained strong seasonal signatures. The amplitude of the 1 km wavelength component was significantly and negatively correlated to the wave height, at a lag of about 60-90 days. We infer from this that increasing wave heights reduced the amplitude of the 1 km scale features and the response of the morphology lagged behind the change in wave conditions. The amplitude time series was also, surprisingly, correlated to the wave energy flux. This may stem from the strong correlation between wave height and direction, rather than a direct forcing-response relationship of wave direction on these amplitudes.

The celerity and wave height were correlated significantly at a lag of about 90 days. The negative correlation indicates that when the wave height increased, the celerity increased towards the south. Surprisingly, the correlation between the celerity and wave energy flux was relatively poor, which was not expected. Interpretation of cause and effect relationships between the wave field and morphology is potentially impeded by the possibility that the celerity of the 1 km features was partly a function of their amplitude, which was modulated by the wave height.

5. Discussion

5.1 Source of alongshore propagating waves

Sand waves with various amplitudes and celerities have been observed in several nearshore environments [*Sonu*, 1969]. Clearly, large scale, progressive, morphologic features exist at Duck. We can suggest a few explanations for the existence of these features. We can also reject some possible explanations, based on characteristic time scales. For example, oblique sand ridges are large scale features, recently discussed by *Trowbridge* [*Trowbridge*, 1995]. These features extend to deep water (~10 m), and have characteristic, long-term, alongshore celerities of $0(10^{-2}$ to $10^{-1})$ m/day. The forcing mechanism for them is probably storm driven currents, which, as Trowbridge showed, may cause an initially alongshore uniform coastline and bathymetry to become unstable. *Hulscher* [*Hulscher*, 1996] presents theoretical descriptions of another type of sand wave, which is an instability driven by tidal currents. However, both oblique sand ridges and tidal sand waves, which are O(0.1 to 1) km in length, have much slower celerities than those observed at Duck. Since the length scale of these deeper water features matches the scales we have observed, it is possible that there is some interaction between the two.

Another sand wave formation mechanism, treated recently by *Thevenot and Kraus* [1995], is ejection of sand plugs from tidal inlets. These plugs may weld to the shore and perturb the longshore current field. Then, they are expected to propagate alongshore in the direction of the longshore current. *Thevenot and Kraus* observed sand waves with wavelengths of about 1 km and celerities of order 1 m/day. The alongshore-progressive behavior was modeled by *Thevenot and Kraus*. However, the modeled sand waves tended

to diffuse more rapidly than those observed in the field. The addition of wave refraction in the model reduced the tendency of the modeled waves to dissipate, and appears to be an important sand wave maintenance mechanism. Although there are no nearby inlets at the Duck field site to allow formation of sand waves as ejected sand plugs, the kinematics of the features we have observed seem consistent with the Thevenot-Kraus model.

5.2 Potential pier effects

A possibly important physical characteristic of our study site is the presence of a pier, which extends 500 m offshore (6 m depth). Since we observed the shoreline behavior only north of the pier, we have no information about what happens near to and south of the pier. If sand waves propagate past the pier, how are they affected by its presence? Does the pier generate sand waves? We hope to extend analysis to observations from both sides of the pier, as there is an extensive collection of surveyed profiles at Duck, spanning over a decade.

6. Conclusions

Observations of the shoreline position at Duck, NC indicated that alongshore progressive features with a length scale of order 1 km were responsible for a large portion (40%) of shoreline variability at this site. The amplitude of these features (~10 m) was modulated by the annual variations in wave height. The amplitude was reduced during periods of increased wave height (winter) and the amplitude increases during calm conditions (summer). Although these features propagated to the south, variations in celerities were not well correlated to the direction of expected wave-driven sediment transport, and were more correlated to changes in the wave height. Surprisingly, the

alongshore-averaged shoreline behavior was not well correlated to wave height. Although the wave field varied on an annual cycle, the alongshore-averaged shoreline position did not, in contrast to expectations from a simple conceptual model of summer-winter behavior. Instead, this component varied most dominantly over an interannual period, in which one cycle was completed in about two years.

The observations and analysis presented here describe the contribution of various alongshore length scales to beach variability at Duck, NC. The results of this analysis indicated the importance of large length and time scales to observed nearshore variability. Extending analysis to observations that cover larger lengths and longer time periods will improve our resolution of the phenomena presented here.

CHAPTER IV: OBSERVATIONS OF INTERANNUAL SAND BAR BEHAVIOR AT DUCK: HOW RELEVANT IS EQUILIBRIUM THINKING?

1. Abstract

Time and length scales of beach variability have been quantified using 16 years of surveyed beach elevations sampled at the Army Corps of Engineers' Field Research Facility, located on the US Atlantic Coast. Between 50% and 90% of the bathymetric variability at this site was explained by alongshore-uniform response over the approximately 1 km alongshore span of the surveys. Although the incident wave height variance was dominated by frequencies at or higher than 1 cycle/year, greater than 80% of the bathymetric variance at all cross-shore locations was explained by frequencies < 1 cycle/year. Interannual cycles consisting of sand bar formation, migration, and decay contributed to the low frequency variability.

An empirical model, forced by predominantly annual variations in incident wave height, explained interannual sand bar response consistent with our observations. The model assumed that bars migrate toward an equilibrium position that was determined to be consistent with a wave "break point". The model included a variable bar response time, empirically determined to be inversely proportional to the wave height cubed. The net effect of the variable response time was to shift the expected long-term mean sand bar position offshore, towards the equilibrium position associated with the largest waves. Response times that are long relative to the characteristic time scale of the forcing (1 year in our case) allow transient (far from equilibrium) response to persist for many cycles of the forcing. The model explained up to 55% of the variance of bar crest velocity time series extracted from 3 different sand bars, and it predicted up to 80% of the observed bar position time series variance. Transient bar behavior could be introduced when bars form near the

shoreline, or when outer bars decay, and inner bars face a changed wave climate. The model did not contain a mechanism for introducing transients, however.

2. Introduction

Sand beaches exhibit a wide variety of morphologies, which vary with geographic location and with time. On beaches with surf zone sand bars, morphologic changes due to changing wave conditions are often striking (Figure IV.1) and these changes have been well documented [*Sonu*, 1969; *Sonu*, 1973; *Short*, 1975; *Wright and Short*, 1984; *Lippmann and Holman*, 1990]. The simplest attempts to predict beach change are based on observed correlations between beach morphology and wave conditions [*Aubrey, et al.*, 1980; *Wright, et al.*, 1985]. Predictions have been made by describing beach morphology with a small number of parameters, and then describing the correlation between these parameters and the wave conditions.

Parameterizations used to describe beach morphology include objective descriptions of surveyed bathymetry [*Winant, et al.*, 1975] or broadly defined (subjective) morphologic states [*Wright and Short*, 1984]. An example of a morphologic state parameterization is the summer-winter (or bar-berm) model, which classifies the cross-shore beach profile within one of two beach states. The summer-winter model is based on observations of many beaches whose shape tends to change from an unbarred (summer or berm) profile to a barred (winter) profile when low energy wave conditions give way to high energy conditions [*Shepard*, 1948; *Komar*, 1974]. Commonly, it is assumed that a particular set of incident wave conditions is associated with a stable equilibrium state. That is, if wave conditions were steady a beach would asymptotically approach a single state. In a variable wave climate, beaches may continually evolve toward a continually changing equilibrium state. This could explain the observed correlations between changes in morphologic parameters

Time Exposure Images, Duck NC

11 October 1995 A

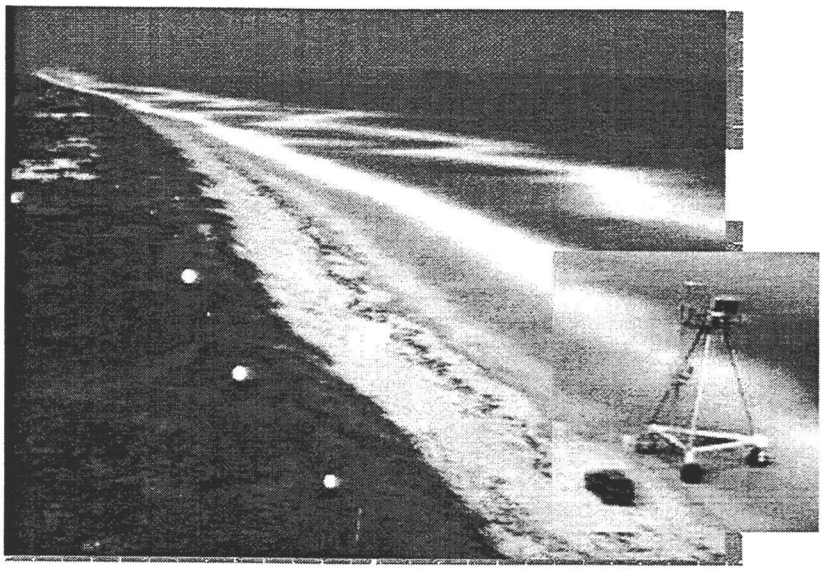

17 February 1996 B

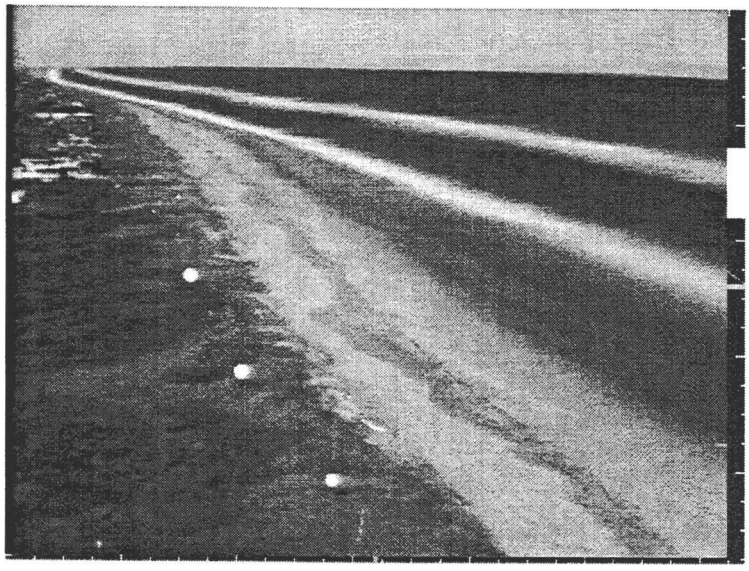

Figure IV.1. Time exposure images at Duck, North Carolina (Army Corps of Engineers Field Research Facility -- FRF) showing irregular (A) and shore-parallel sandbars (B). Averaging video images over a 10 minute period produces stable images of the foam patterns produced by wave breaking over sand bars and near the shoreline. The CRAB, used to conduct bathymetric surveys at this site, is shown in the inset next to a full sized vehicle (Chevrolet Suburban).

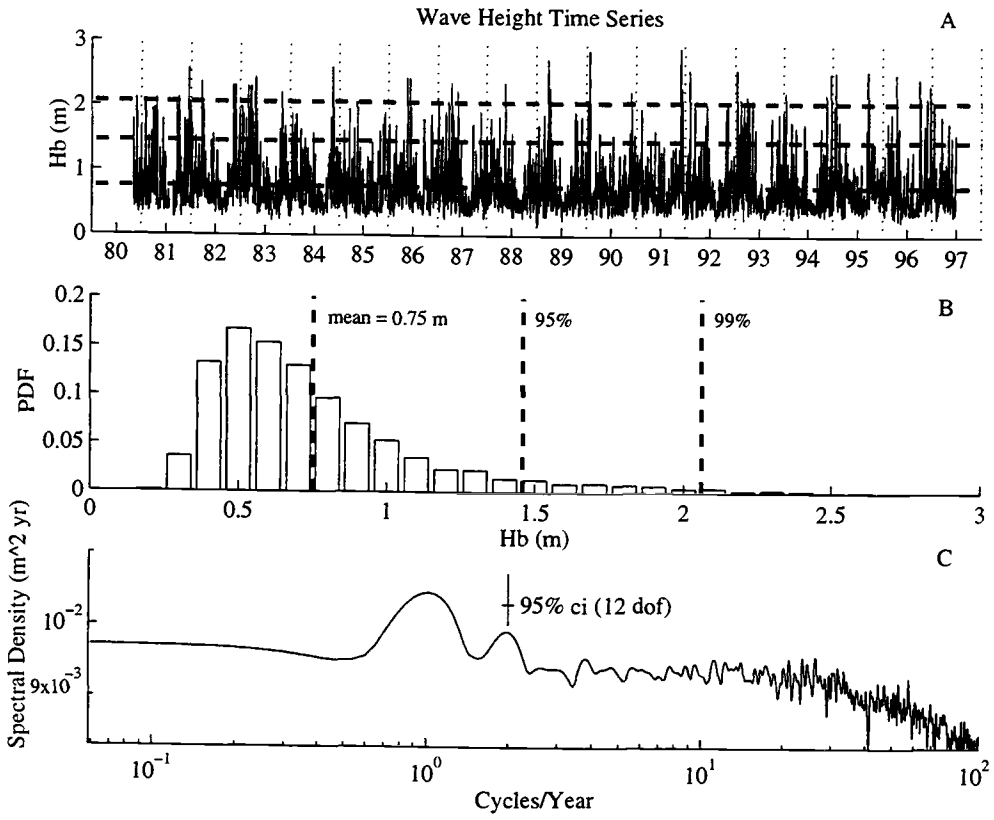

Figure IV.2. (A) Time series of daily averaged rms wave heights measured over a 16-year period at the FRF site. The wave height has been transformed to the predicted value at breaking. The dashed lines indicate (from the top) 99 and 95 percentiles, and the mean. These levels are marked on the pdf (B). The spectrum (C) shows significant peaks at annual and semi-annual frequencies.

and changes in wave conditions.

On barred beaches the cross-shore position of the bar crest has been used to parameterize the beach morphology and its variability. At some locations, changes in bar crest position are correlated to changes in wave conditions [*Wright, et al.*, 1985; *Lippmann and Holman*, 1990]. Time scales shorter than one year contribute to this correlation, since seasonal or storm (weekly to monthly) cycles tend to dominate the variation of the wave climate (Figure IV.2). Recently, however, interannual sand bar variability has been

observed, consisting of net seaward migration of sand bars over periods exceeding a decade. This variability was not correlated to observed variations in the wave conditions.

In The Netherlands, 30 years of annual beach profile surveys were collected annually over a 100 km long coastline [*Ruessink and Kroon*, 1994; *Wijnberg and Terwindt*, 1995]. *Ruessink and Kroon* [1994 -- hereafter referred to as RK94] describe interannual sand bar cycles consisting of bar generation near the shoreline, net seaward propagation, followed by decay when sand bars reached the outer extent of the surf zone. Surprisingly, seaward sand bar migration took place without net sediment loss or gain. The pattern of seaward migration was uniform over many kilometers of the coastline. *Wijnberg and Terwindt* [1995] showed that the characteristic duration of interannual sand bar cycles could change dramatically across sharp geographic boundaries. For example, the duration of sand bar cycles changed from about 15 years to 4 years on opposite sides of a jetty. The forcing and geologic constraints on either side of the jetty were similar.

Long-term, seaward bar migration was also observed on the US East Coast at the Army Corps of Engineers Field Research Facility (FRF), located at Duck, North Carolina. At this site, bi-weekly to monthly surveys spanning a 1 km length of the shoreline have been collected since 1981, and oblique video images (Figure IV.1) have been collected daily since 1986. Using the first three years of the survey data at this site (1981-1983), *Birkemeier* [1985] mapped the changes of the cross-shore position of several shore-parallel sand bars. He observed the end of one interannual bar cycle (outer bar decay), followed by offshore migration of an inner bar, and then generation of a new inner bar near the shoreline. The bar response was coherent over the 1 km alongshore extent of surveys.

Using video time-exposure images, *Lippmann et al.* [1993] documented the completion of an interannual sand bar cycle and the beginning of yet another in 1989. Bar

cycles, initiated by the generation of new inner bars, lasted approximately 7 years (1982 to 1989). Both *Birkemeier* [1985] and *Lippmann et al.* [1993] showed that the decay of an outer bar was followed within 1 year by rapid offshore migration of an existing inner bar and generation of a new sand bar near the shoreline. These transitions occurred synchronously with large storm waves, where the wave height was several times the annual average. However, there were many apparently similar storms that did not precipitate new sand bar cycles.

We would like to understand how wave forcing, dominated by frequencies equal to or higher than 1 cycle/year, can lead to significant, interannual response. An objective of this paper is to evaluate the consistency of the assumption that beach morphology evolves toward an equilibrium state. We will call models that make this assumptions "equilibrium models". In the next section (section 2) a simple, heuristic, equilibrium model for cross-shore bar migration is developed and used to establish quantitative predictions that can be compared with observed sand bar response. In section 3, the data used to test the model are described in detail. The data comprised over 400 bathymetric surveys, collected over a 16-year period at the FRF. Using an approach similar to that of RK94, time series of sand bar properties were extracted from the bathymetric data. In section 4, the response of sand bar crest positions to variations in incident wave height are compared to predictions based the equilibrium model.

3. Equilibrium theory

Beach morphology reaches equilibrium when time-averaged sediment transport gradients vanish everywhere. If we consider alongshore-uniform models, the cross-shore sediment transport must vanish everywhere. Process-based equilibrium models were derived by *Bowen* [1980] and *Bailard and Inman* [1981]. In these models, equilibrium

resulted when the tendency for offshore (down slope) transport driven by "stirring" due to oscillatory currents balanced the tendency for net onshore transport driven by a skewed velocity distribution or mean current. This led to prediction of a monotonic cross-shore profile ($h \sim x^{2/3}$, where h is depth, x is distance from the shoreline). The proportionality depended only on incident wave conditions and sediment properties.

It seemed reasonable that more complex morphologic patterns, such as shore-parallel and crescentic sand bars, were also equilibrium morphologies. In these cases, down slope transport could balance net transport driven by low-frequency wave modes [*Bowen*, 1980; *Bowen and Huntley*, 1984]. For example, *Holman and Bowen* [1982] produced realistic looking barred bathymetry over a 2-d horizontal domain which balanced transport driven by edge waves.

Assuming that sand bars approach an equilibrium state, and that bar morphology is adequately described by the cross-shore position of the bar crest, it is possible to construct a heuristic, equilibrium model to predict bar position evolution. If wave conditions are variable and a sand bar has a finite response time, a bar will approach a time-varying equilibrium position at a rate that we assume depends on a response time coefficient (α) and the distance from an equilibrium, X_{eq}:

$$\frac{\partial X_C(t)}{\partial t} = -\alpha(t)\,\{X_C(t) - X_{eq}(t)\}, \qquad (1)$$

where X_C represents the cross-shore position of an alongshore-uniform sand bar, α is the reciprocal of a characteristic response time (positive valued), and X_{eq} is the bar position at equilibrium, forced by a parameterization of the nearshore hydrodynamics. We will assume that the forcing is function of the incident wave height. *Wright et al.* [1985] proposed a similar model to predict changes between a set of 3 beach states (reflective, intermediate, and

dissipative). The full range of bar response predicted by this sort of model has not been described or compared quantitatively to observations.

A simple case to explore with the model (1) is that of constant response time and periodic forcing (e.g., $X_{eq} = \sin[\omega t]$), perhaps representing the seasonal variation of wave height. The response of this system is

$$X_c(t) = \{X_o + \frac{\alpha\,\omega}{\alpha^2+\omega^2}\} \exp[-\alpha t] + \{\alpha/\sqrt{\alpha^2+\omega^2}\} \sin[\omega t - \phi], \qquad (2a)$$

where

$$\phi = \tan^{-1}[\omega/\alpha]. \qquad (2b)$$

The first term on the right hand side of (2a) represents a transient response from an initial position, X_o, which decays over a time scale of $1/\alpha$. As a result of the finite response time, the periodic response (second term in 2a) is phase shifted relative to the forcing by ϕ, and the amplitude of the periodic response is damped in proportion to $\alpha/\sqrt{\alpha^2 + \omega^2}$.

Bar migration results from sediment transport patterns which erode sand from the rear flank of the bar and deposit sand on the front flank of the bar. The migration rate depends on the erosion and deposition rates, which depend, presumably, on the magnitude of near-bottom wave driven velocities. We note that the classic sediment transport formulas [*Bagnold*, 1963] predict a transport proportional to near-bottom velocities raised to a power, p (p=3 or 4). Since maximum wave orbital velocities are linearly related to wave height (linear theory), sediment transport rates may vary as H^p. *Komar and Inman* [1970], for example, presented an example of an $H^{2.5}$ dependence for alongshore sediment transport. We assume that a sediment transport rate dependence on wave height affects the bar response time such that

$$\alpha = \alpha_1 H^p. \qquad (3a)$$

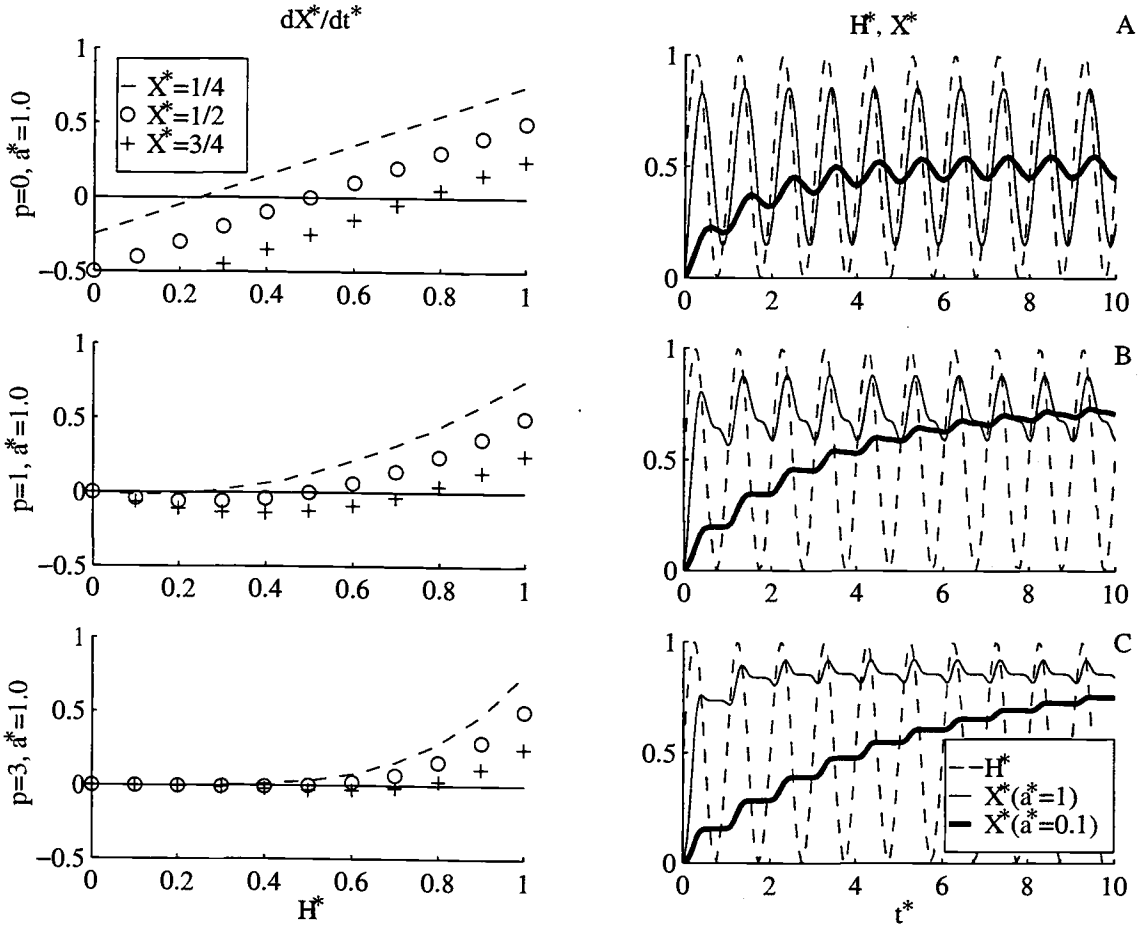

Figure IV.3. Equilibrium model prediction of migration rate and bar position time series. The plots on the left are the predicted migration rate (dX^*/dt^*) as a function of wave height (H^*), with p and a^* held constant in each row of plots (A-C). The adjacent plots show resulting time series with $a^* = 1$ and $a^* = 0.1$, illustrating the differences in phase shift, damping, and persistence of the transient response.

In Figure IV.3, the left hand panel in each pair shows the predicted bar response as a function of non-dimensional wave height, H*, with the non-dimensional bar position fixed at 3 different values. Bar position, wave height, and time were non-dimensionalized as $X^* = X_c/\alpha_2$, $H^* = H/H_{max}$ (H_{max} is the maximum wave height), $t^* = t\,\omega$, and $a^*=\alpha_1/\omega$. The equilibrium position was assumed to vary as

$$X_{eq}(t) = \alpha_2 H(t). \qquad (3b)$$

For all cases where $p>0$, the response was insensitive to changes in the wave height or bar position for low wave heights.

The right hand panels in Figure IV.3 show time series of the response for $a^*=1$ (short response time) and 0.1 (long response time). Wave height variations were periodic: $H(t) = H_{max} (1+\mathrm{Sin}[\omega t])/2$. The bar was initialized at the "shoreline". Transient, offshore migration persisted over a time scale shorter than $O(1/a^*)$. After the transient response decayed, the bar position oscillated about a mean position. The mean position was further from shore at higher values of p, approaching the maximum position according to $\overline{X^*} = 1 - 1/\{2\,(p+1)\}$. Thus, if sand bar response times are long relative to the time scale of the forcing, net seaward migration may persists as a transient response that is enhanced by increasing the response time exponent, p.

4. Field data description

4.1 Data collection and processing

Since 1981, both bi-weekly and monthly beach surveys have been performed at the FRF using the Coastal Research Amphibious Buggy (CRAB, Figure IV.1). The elevations have been referenced to the NGVD29 datum (National Geodetic Vertical Datum, which lies about 0.25 m below the mean water level at the FRF site). The surveys typically extended from the back beach to about 8 m water depth (about 1 km offshore), and spanned roughly 1 km alongshore, centered about the FRF pier (Figure IV.4A). The cross-shore sample interval varied from about 1 m to 50 m. Not all observations were independent, since the CRAB's footprint spanned 10 m. The alongshore sample spacing ranged from 25 to 100 m. Twenty-six transects were surveyed approximately monthly, while bi-weekly surveys sampled four of the twenty-six cross-shore transects, two at the south end (y = -92, 0 m)

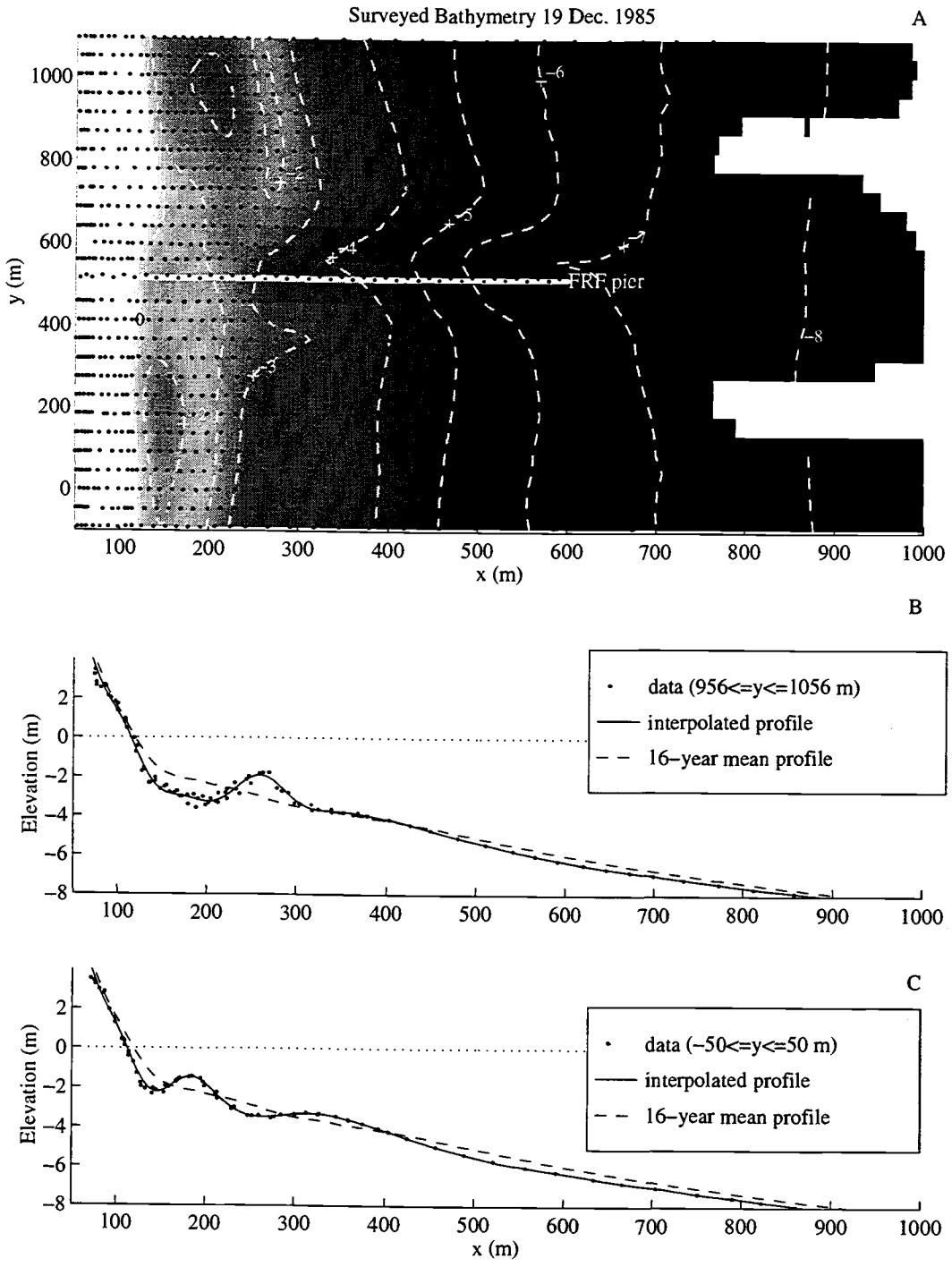

Figure IV.4. Contour map (A) and profiles (B-C) of surveyed bathymetry on 9 December 1985. Contour interval is 1 m and the shading maps elevations between -8 m (black) and 0 m (white). Dots indicate observed bathymetry. Note the differences in bar positions north and south of the pier.

and two at the north end (y = 1006, 1096 m) of the study area. A total of 449 different surveys from January 1981 to August 1996 have been analyzed.

The raw survey data were interpolated to a grid (Figure IV.4B-C) with a cross-shore spacing of 5 m and an alongshore spacing that matched the locations of the regularly occupied cross-shore transects (approximately 50 m spacing). An objective (sub-optimal) interpolation method [*Ooyama*, 1987] was used, and is described in Appendix A. The interpolation scheme imposed an adjustable spatial filter that was tuned to damp potentially unresolved cross-shore and alongshore length scales (cross-shore scales < 25 m and alongshore scales < 100 m). The interpolation scheme included an interpolation error estimate, which was the expected error between the interpolated surface and the spatially filtered version of the true surface. Interpolation errors resulted from measurement error, unresolved morphology (e.g. mega-ripples and beach cusps), and the mismatch between the true spatial covariance structure and the assumed Gaussian form of the covariances, which relate bathymetry at observation locations to the bathymetry at the interpolation points. Only the measurement error has been estimated directly and, over a smooth bottom, the vertical accuracy of each elevation observation was about 10 cm [*Birkemeier and Mason*, 1984]. This error estimate does not account for unresolved bed forms, such as mega-ripples (O(1 m) wavelengths and 0(10 cm) amplitudes, e.g. *Gallagher et al.* [1996]).

4.2 Spatial patterns of variability

Reducing the description of morphologic variability to a single parameter, X_C, implies that profile variability results from the migration of an alongshore-uniform sand bar having a fixed cross-shore spatial structure. We estimated the fraction of the total temporal variance that was alongshore-uniform. First, the 3-dimensional bathymetric data were decomposed into a time-mean bathymetry and deviations from the mean.

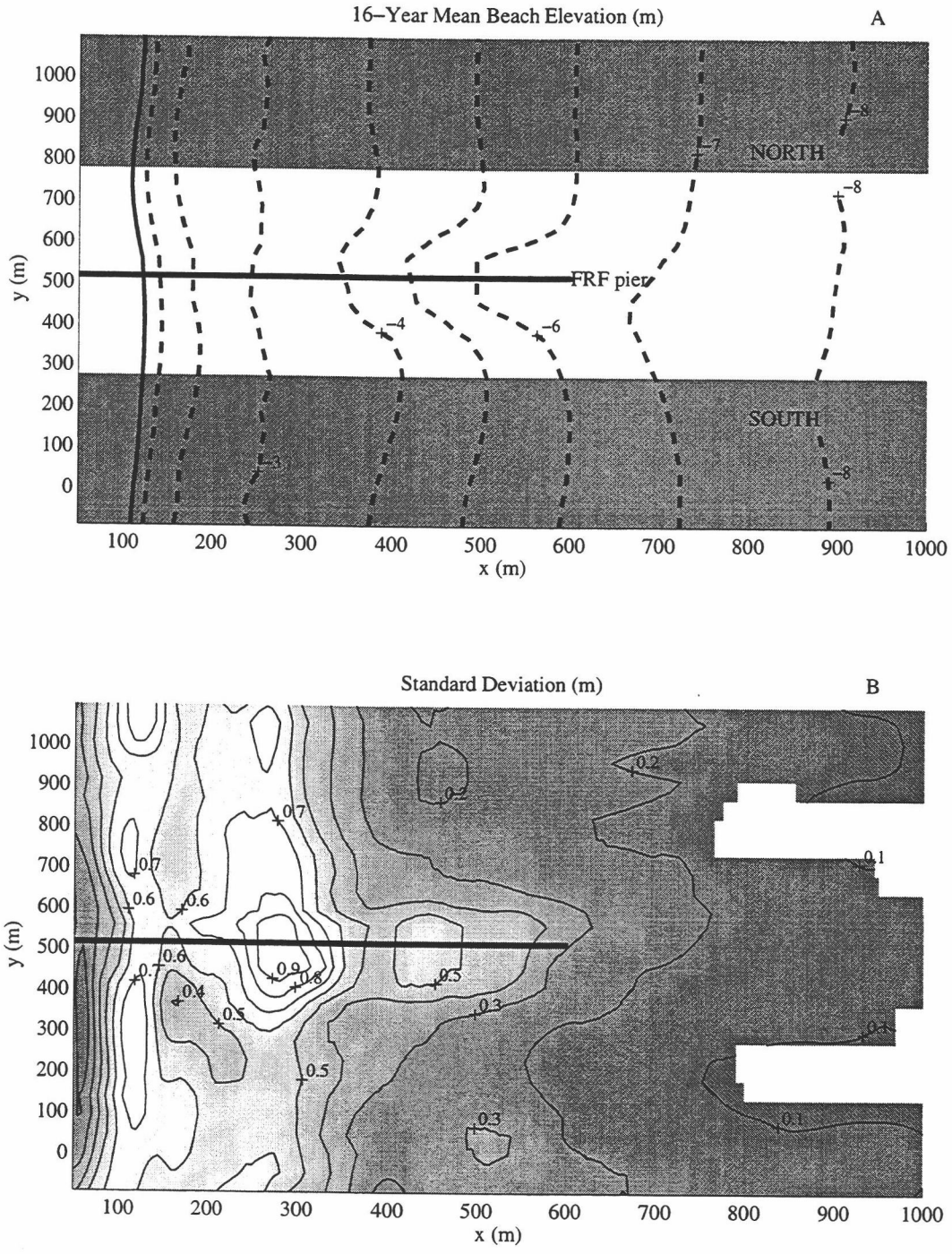

Figure IV.5. 16-year mean (A) and standard deviation (B) of interpolated elevations. The contour intervals are 1 m for the mean and 0.1 m for the standard deviation. Interpolated profiles within the shaded regions (A) were included in our analysis. Broken contours indicate regions where interpolation errors of at least half of the observations exceeded 0.2 m. The gray scale shading in (B) is proportional to the standard deviation (0=black, 1=white).

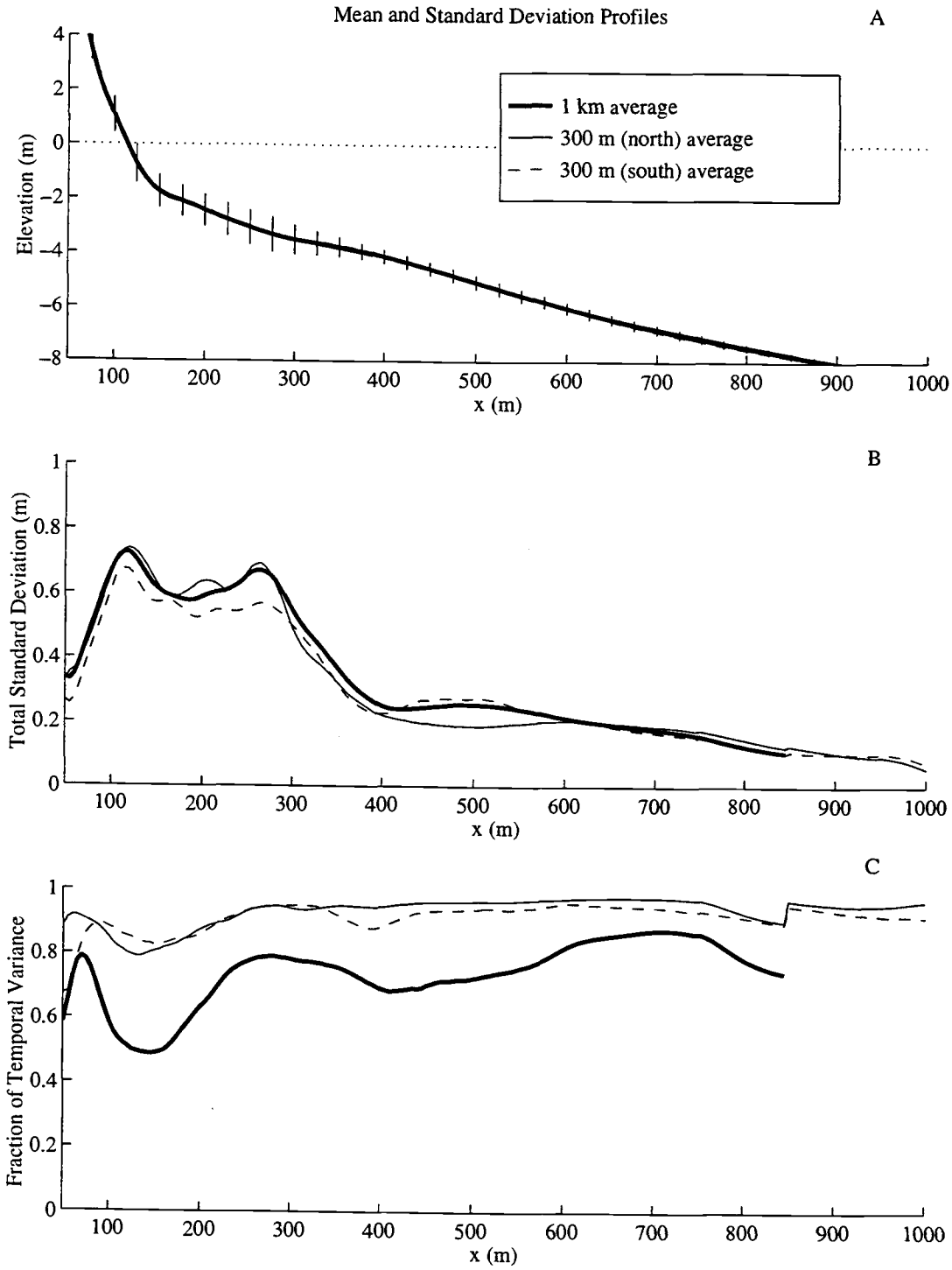

Figure IV.6. Alongshore-averaged profiles of the mean (A) and standard deviation (B) bathymetry, and fraction of alongshore-uniform, temporal variance (C). Profiles were estimated using observations within each of the 300 m wide regions (300 m averaged) and over both regions (1 km average). Error bars are 1 standard deviation (1 km alongshore average).

$$Z(x,y,t) = Z'(x,y,t) + \overline{Z}(x,y), \quad (4)$$

where the over bar indicates time averaging. Figure IV.5A shows the 16-year mean beach elevation at each grid location. The mean elevation at each grid point was calculated from all elevations having an rms interpolation error less than 20 cm. The mean surface has a pronounced shore-perpendicular trough beneath the pier seaward of the 4 m mean depth contour. Also, the standard deviation of beach elevation (Figure IV.5B) was relatively high near the pier. Because of these anomalies, the central region of the field area was excluded from the analyses to follow. Two regions were more than 200 m from the pier. The north region was bounded by transects along y = 776, 1096 m and the south region was bounded by y = -92, 228 m.

Figure IV.6A shows time- and alongshore-averaged profiles within the north and south regions (300 m average) and the average across these regions (1 km average). Differences between the mean profiles were small (the profiles overly one another), relative to the magnitude of temporal deviation. The shape of the mean profiles consisted of two nearly planar sections intersecting at a mean depth of about 2 m. The slope of the landward section was about 1/25, and the slope of the seaward section was about 1/100.

Standard deviation profiles (Figure IV.6B) were estimated by averaging the squared deviations in both time and alongshore:

$$S^2_{total}(x) = \sum_{i=1}^{Nt} \sum_{j=1}^{Ny} Z'(x,y_j,t_i)^2/(N_y\, N_t). \quad (5)$$

The shapes of these profiles in the north and south regions were similar (and, hence, similar to the 1 km average). Variance was low at the onshore limit of the surveys (in the dunes and back beach) and variance was high where sand bars were active (between the shoreline and about 3 m mean depth). Between the 3 and 4 m mean depth contours, the beach elevation variance dropped markedly and then decreased gradually across the remaining portion of

the profile. There were some differences in the variance structure from the north to south, such as a region of relatively high variance in the south (centered on x=500 m), that was absent in the north.

The alongshore-uniform component of profile deviations was extracted by alongshore-averaging:

$$Z'_y(x,t) = \sum_{i=1}^{Ny} Z'(x,y_i,t)/N_y. \quad (6)$$

Figure IV.6C shows the fraction of alongshore-uniform variance within and across the north and south regions, estimated as S_y^2/S_{total}^2, where

$$S_y^2(x) = \sum_{i=1}^{Nt} (Z'_y(x,t_i))^2/N_t. \quad (7)$$

In both the north and south regions, the alongshore-uniform mode, averaged over 300 m, explained more than 80% of the total profile variance. The percentage of alongshore-uniform variance was lowest (80%) slightly seaward of the mean shoreline position at a mean depth of about 1 m. This percentage was highest at the seaward limit of the surveys. Averaging over both north and south regions (1 km alongshore average) led to a pronounced variance reduction (50%) near the shoreline, indicating that much of the beach variability could be attributed to features with alongshore scales less than 1 km. A step in the percent-variance profile occurred at the typical seaward limit of the monthly surveys (about x=800). Seaward of 800 m, only two profiles in each region were surveyed (separated by 100 m), aliasing short scale variability.

4.3 Time scales of variability

The relative importance of morphologic variability occurring at interannual and intra-annual time scales was evaluated using time series extracted from the alongshore-averaged

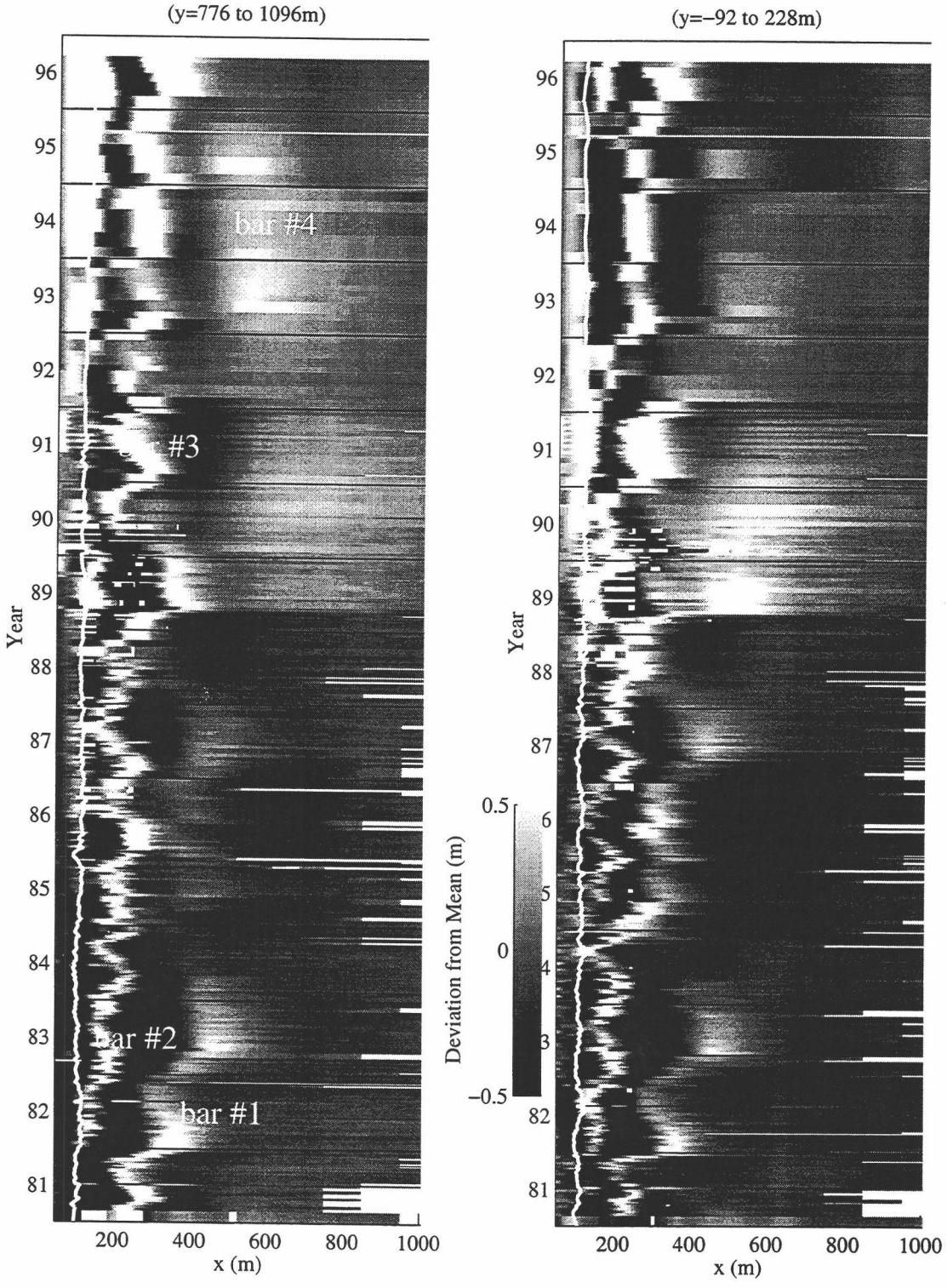

Figure IV.7. Time stack of alongshore-averaged deviations from 16-year mean profile. The solid white line running along the time axis is the position of the shoreline (0.0 NGVD). Individual sandbar crests are labeled in the north study region (y = 776 to 1096 m). Blank regions indicate missing observations (interpolation error > 0.2 m).

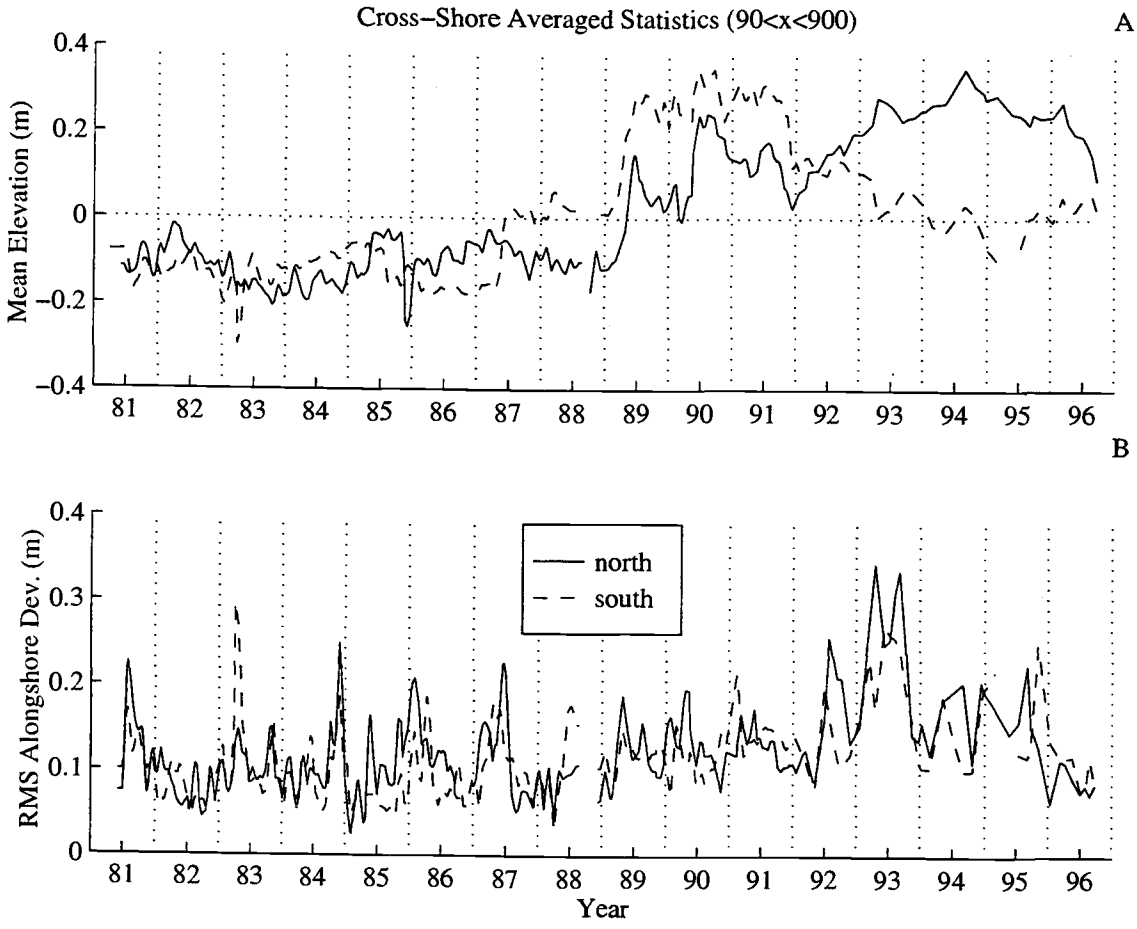

Figure IV.8. Time series of cross-shore averaged elevations (A) and rms deviation (B) about the alongshore-averaged profiles. Observations between +2 and -8 m mean elevations were included in the cross-shore average.

profiles. Intra-annual time scales include a seasonal cycle and shorter cycles associated with passing storms. The time-averaged profile was subtracted from all profiles and the residual deviations were analyzed. Figure IV.7 shows space-time maps (time stacks) of the deviations. For reference, a solid white line running roughly parallel to the time axis marks the shoreline (0.0 m elevation), and horizontal lines mark January 01 of each year. Warm colors correspond to elevations above the mean level (sand bars) and cold colors correspond to elevations below the mean (troughs).

A striking feature in the time stacks is the degree of coherence of sand bars, which can be tracked for nearly a decade in some cases. 4 bars are identified in the north region, and they will be analyzed in detail in section 3.4. Beach changes prior to 1989 occurred with relatively little change in the total sediment volume (Figure IV.8). However, in 1989 there was significant gain in sediment. It is likely that cross-shore sediment exchanges were responsible for this gain, since significant deposition occurred at the seaward limit of the surveys.

Time series of profile deviations were extracted at locations corresponding to mean depths of 0 m (near the shoreline), 3 m (inner bars), 4 m (outer bars), and 6 m (seaward of most bars). Figure IV.9 shows filtered (in time) time series of the deviations from the mean elevation. The filter applied to each observation was a weighted sum of observations within ±30 days. The filter weights were scaled by a Hanning (cosine squared) window. The filtered observations were linearly interpolated to an equally spaced time series with a sample interval of 30 days. Hereinafter, the resulting time series are called "monthly-averaged", although the filtering operation was imperfect, especially in cases where the sample spacing exceeded 60 days (the filter operation did nothing in these cases). The "monthly-averaged" time series were analyzed using techniques requiring equally spaced observations.

Cross-shore differences in beach response were evident. Near the shoreline, the beach elevation included strong intra-annual and interannual fluctuations. In contrast, at the 4 and 6 m mean depth locations the intra-annual cycles were strongly damped and the beach response had a "saw-tooth" appearance. This response appears correlated across both north and south regions and in the cross-shore direction. Rapid elevation increases typically corresponded to rapid seaward migration of sand bars (see Figure IV.7). A clear example

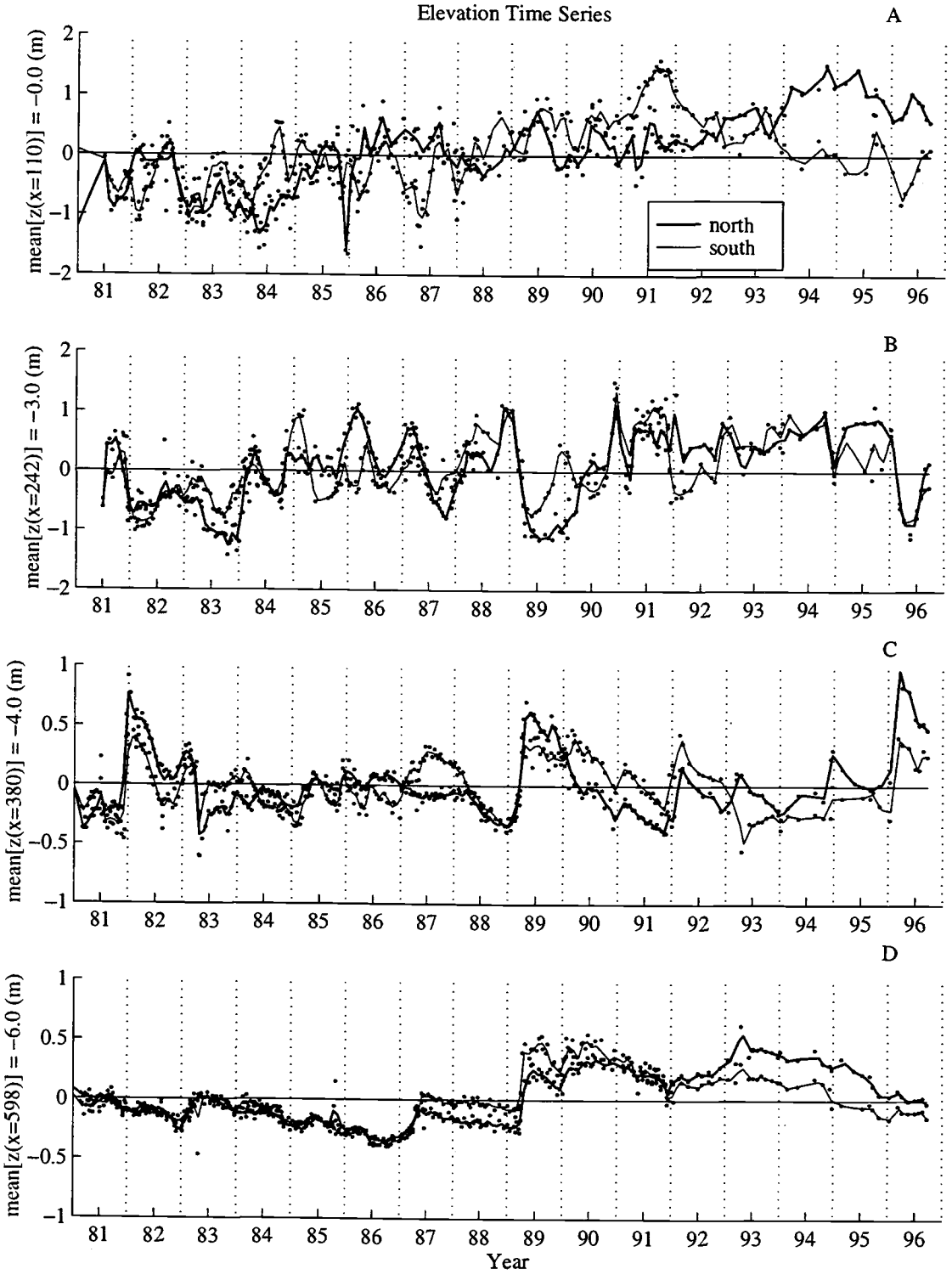

Figure IV.9. Time series of profile deviations, sampled at mean water depths of 0, 3, 4, and 6 m (A-D). The time series were extracted from the alongshore-averaged profiles at fixed cross-shore locations (labeled for reference to Figure IV.7). Dots indicate the grid elevations, while the lines represent the "monthly-averaged" values.

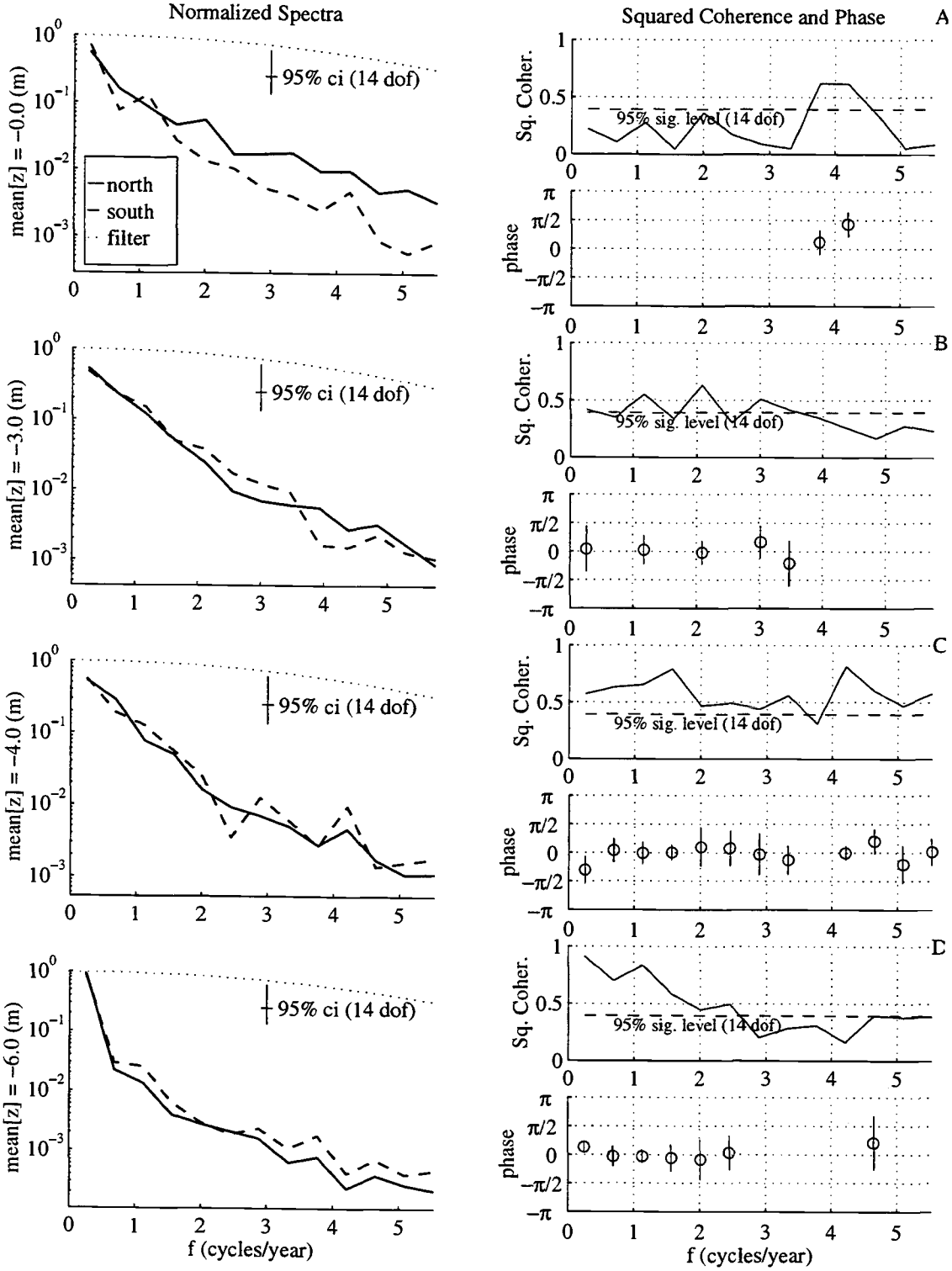

Figure IV.10. Power, phase, and coherence spectra corresponding to the elevation time series. The dotted line in each power spectrum plot describes the filter characteristics of the "monthly-average" operation, which introduced no more than a 50% power loss at the highest frequencies. Phases are plotted only where the coherence estimates exceeded the 95% significance level.

of this occurred between 21 and 27 February 1989, which corresponded to the transition of an inner bar to an outer bar, observed by *Lippmann et al.* [1993]. Following the rapid increases, the beach elevation decreased gradually. Similar behavior has been observed elsewhere [*Aubrey*, 1979].

At all locations, beach changes were dominated by interannual variability. Figure IV.10 shows band-averaged frequency spectra corresponding to each time series. More than 70% of the bathymetric variability was attributed to frequencies lower than 1 cycle/year (the first two frequency bands). These frequencies explained over 90% of the variability at the offshore locations. The squared-coherence and phase shift were calculated between each pair of time series extracted from the same mean depth, but separated by approximately 1 km alongshore. In most cases where the coherence between the north and south locations was high, the phase shifts were near zero. This is an important observation because it indicates that large-scale, alongshore-progressive features (which would appear as a phase ramp) were not responsible for the long-term sand bar cycles.

The coherence between the north and south was not always high. At the higher frequencies ($f > 1$ cycle/year) this may be due to the reversing migration direction of sand bars at intra-annual time scales. If the bars simply propagated offshore and the sample locations were offset relative to the phase of the bar, a phase ramp would appear in the phase spectrum. However, as the direction of bar migration changes the phase shift continually changes signs, leading to poor coherence averaged over the entire record. The alongshore coherence was poor even at low frequencies at the inner two locations. If long-term sand bar cycles were responsible for low-frequency variations, then some characteristics of these cycles must have differed on either side of the pier.

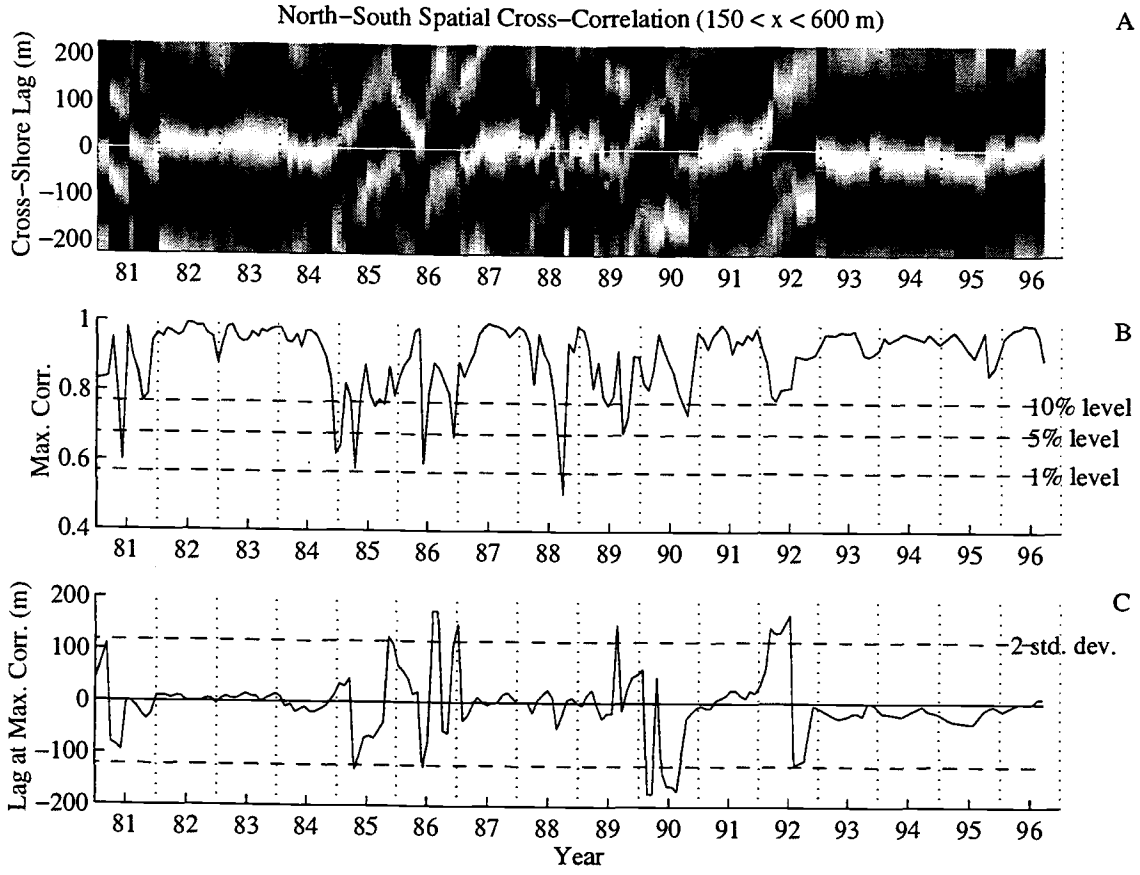

Figure IV.11. Spatial correlation between profiles north and south of the pier. The first plot (A) is a gray-scale map of correlation at each time (horizontal axis), but different cross-shore lags (vertical axis). Black corresponds to correlations less than zero and white corresponds to a correlation of 1. When the maximum correlation was near zero lag, bars in the north were aligned with bars in the south. The remaining time series show the maximum correlation (B) at each time (dashed lines are exceedance levels) and the corresponding lag at maximum correlation (C).

Differences in beach response on either side of the pier were quantified by examining the spatial correlation between profiles in the north and south regions. If beach response were uniform alongshore, correlations would be maximum at zero lag. Also, the correlation would be high (near 1). Figure IV.11A shows the cross-correlations as a function of cross-shore lag, estimated from monthly-averaged surveys. Figure IV.11B shows that there were periods of high correlation at nearly zero lag, interspersed with periods of poor correlation and/or maximum correlation at unusually high lags (Figure

IV.11C). For instance, in early 1985, the lag corresponding to the maximum correlation began to drift toward large lags (large is defined relative to 2 standard deviations about the mean). The drift was in the direction of increasing lag, which corresponded to the bar system in the south migrating seaward relative to the bar system in the north. The lag between the two systems remained high and the correlation was low until 1987. Figure IV.4 shows a contour map of the beach in December 1985. The sand bars were nearly shore-parallel on either side of the pier. However, an inner bar was absent to the north. Instead, a single bar appeared at a cross-shore position that corresponded to the trough between the inner and outer bars in the south. In 1992, another episode of relative migration occurred, doubling the number of bar cycles observed in south, relative to the north region.

4.4 Identification of individual sand bars

Alongshore-uniform response was significant (explained > 80% of variance) and was associated with the migration of sand bars. If sand bar properties, such as amplitude or length remain fairly constant, bar crest positions adequately parameterize much of the morphologic variability at this site. Bar crests were identified as maxima in detrended and smoothed deviation profiles. The results obtained using this bar crest definition differ from the result that would have been obtained if bars were identified as bathymetric maxima. The difference depends only on the slope of the mean profile. Differences are small where the mean profile's slope is small, relative to the deviation profile's slopes. However, no bathymetric maxima would be found if the slope of the mean profile approached the maximum deviation profile slopes. Tracking crests in the deviation profile better preserves the identity of coherent bar forms, regardless of their location on the mean profile [*Bowen and Huntley*, 1984].

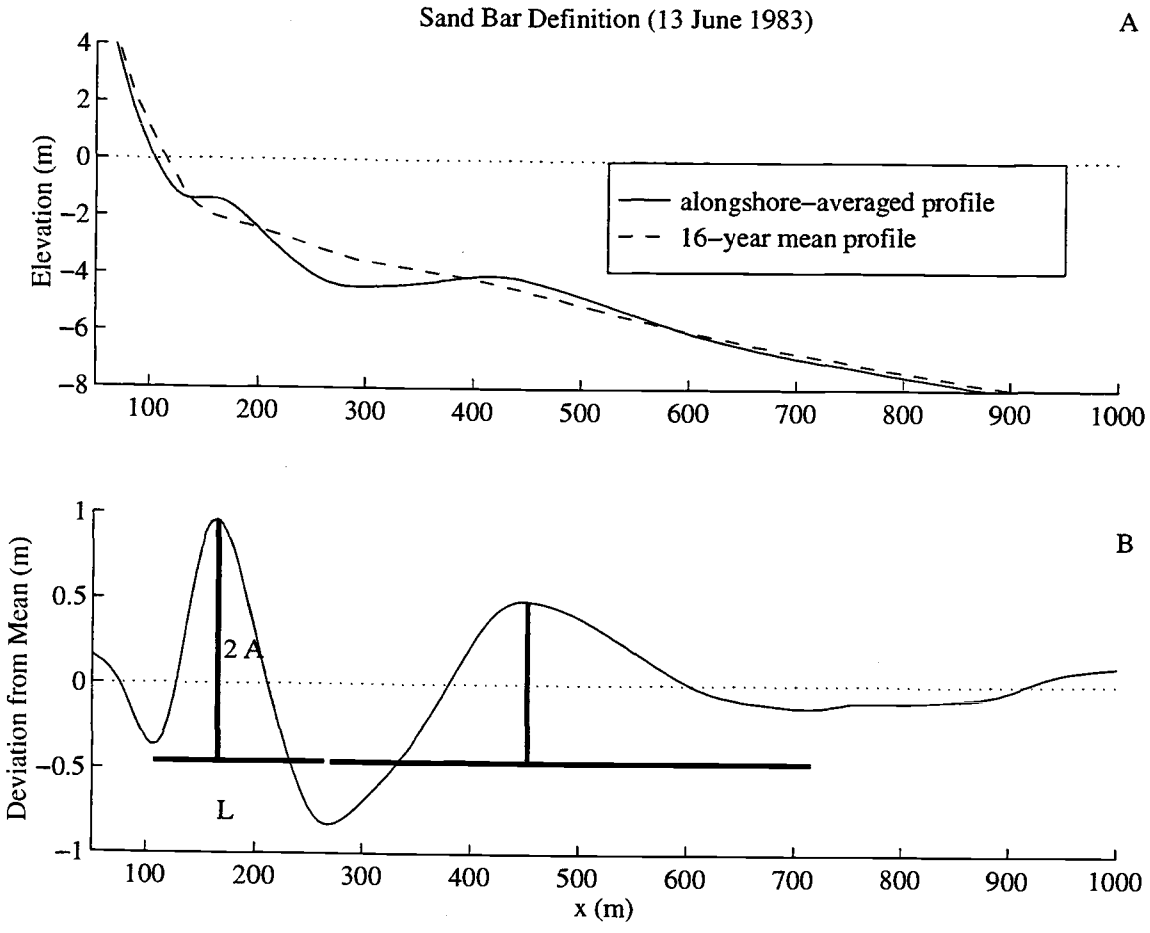

Figure IV.12. Definition sketch of bar parameters on 13 June 1983. The mean profile (shown in A) was subtracted from the observed profile. Bars were identified in the detrended deviation profile (B).

Using data from the region north of the pier, zero-down-crossings of the deviation profile's slope were used to locate bar crests. The extent of bars was bounded onshore and offshore by profile minima (Figure IV.12). Bar length was defined as the distance between the minima, and bar amplitude was defined as half the mean elevation difference between minima and maxima. Bar properties were estimated with a variety of other techniques, which all gave essentially the same results. Each bar crest was associated with one of four persistent sand bars (named bar #1-#4, Figure IV.7). Each crest was assigned to the nearest bar, where "distance" was measure by position and bar crest depth. Some manual

intervention was required to identify bar's at the beginning and end of interannual bar cycles. Bars occasionally divided into a shoreward propagating feature (called shoreward propagating accretionary waves, SPAW, [*Wijnberg and Holman*,]) and an offshore propagating feature. The SPAWs were manually identified and culled from the time series. Figure IV.13 shows resulting time series of bar properties. As with the elevation time series discussed earlier, the time series in Figure IV.13 were filtered. The mean values of bar properties are summarized in Table IV.1.

The monthly sample frequency resolved both the interannual changes in bar position as well and the transition periods when outer bars disappeared, inner bars migrated offshore, and new bars formed near the shoreline. These aspects of bar response were consistent with the RK94 model. Sand bars generally formed near the shoreline (e.g., bars 2 and 3) and migrated offshore (e.g., bars 1 and 2). The transitions of an inner bar to an outer bar occurred in less than a year to 3 years. In the case of bar 1, the transition period was indicated by the approach of bar crest depth to a stable value of about 4 m by mid 1983. During the transition of bar 2, a stable depth of about 4 m was reached within a few months. While bar 1 persisted as an outer bar for 7 years, bar 2 decayed within 2 years. Interestingly, bar decay and ultimate disappearance was clearly associated with onshore migration. Onshore migration of outer bars conflicts with the RK94 model, which associated outer bars with decay and offshore migration. Bar 4, which appeared offshore and migrated onshore, was particularly anomalous in this respect.

The amplitudes and wavelengths of all the sand bars exhibited large fluctuations (relative to their mean values). Significant amplitude and wavelength changes occurred over time scales that were comparable to the time scales of significant bar position changes. There were occasional, striking variations in bar wavelength, which resulted when bars divided (forming SPAWs). This occurred in 1988 (bar #2) and in 1992 (bar #3). In 1986,

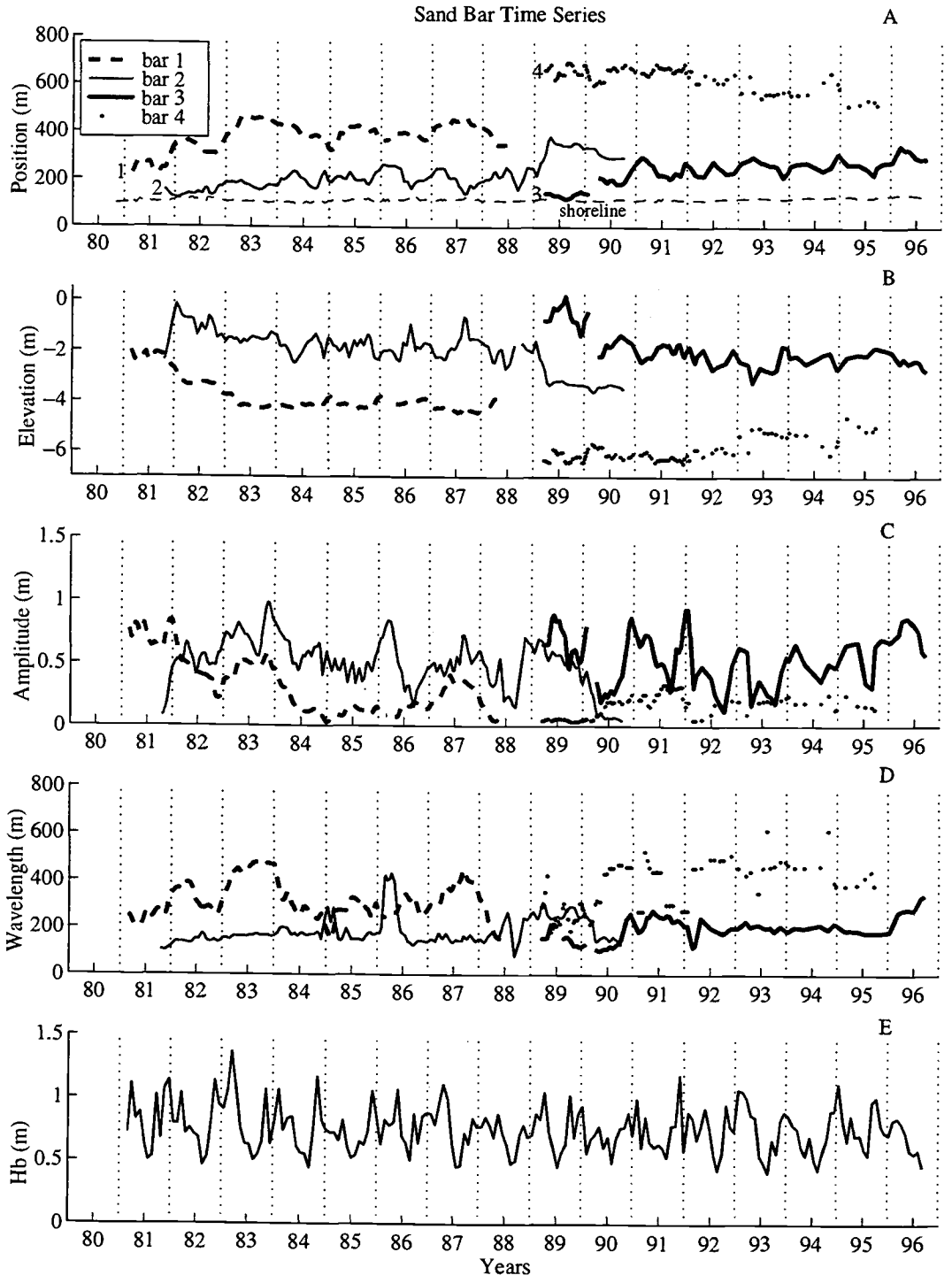

Figure IV.13. Time series of bar crest parameters. All time series are of monthly-averaged values. The corresponding wave height time series have been filtered as well.

Table IV.1. Bar and Shoreline Statistics

Data	N	$\overline{X_c}$	$\overline{A}$	$\overline{L}$	$\overline{h_c}$	$\overline{C}$	% var. in trend
	[# obs.]	[m]	[m]	[m]	[m]	[m d^{-1}]	
Bar 1	195	375 (66)	0.7 (0.5)	314 (81)	3.8 (0.7)	0.046	38
Bar 2	233	215 (62)	1.0 (0.4)	185 (64)	1.9 (0.8)	0.051	59
Bar 3	94	227 (58)	1.1 (0.4)	199 (54)	1.9 (0.7)	0.057	59
Bar 4	85	634 (51)	0.3 (0.2)	369 (117)	5.9 (0.4)	-0.058	45
Shore (north)	300	113 (9)	--	--	--	0.004	51
Shore (south)	328	113 (8)	--	--	--	0.003	28

Values in parentheses are 1 std. dev.
$\overline{h_c}$ is bar crest depth
$\overline{C}$ is mean migration rate estimated from linear trend.

the wavelength of bar #2 doubled, as the inner bar apparently merged with the outer bar. The model that we will test does not incorporate any changes in bar amplitude or wavelength.

5. Equilibrium model evaluation

The equilibrium model (equation 1) was used to predict changes in bar crest position, using the measured wave height to force X_{eq}. Wave height observations were transformed to an rms breaking wave height, assuming that the wave height at breaking was

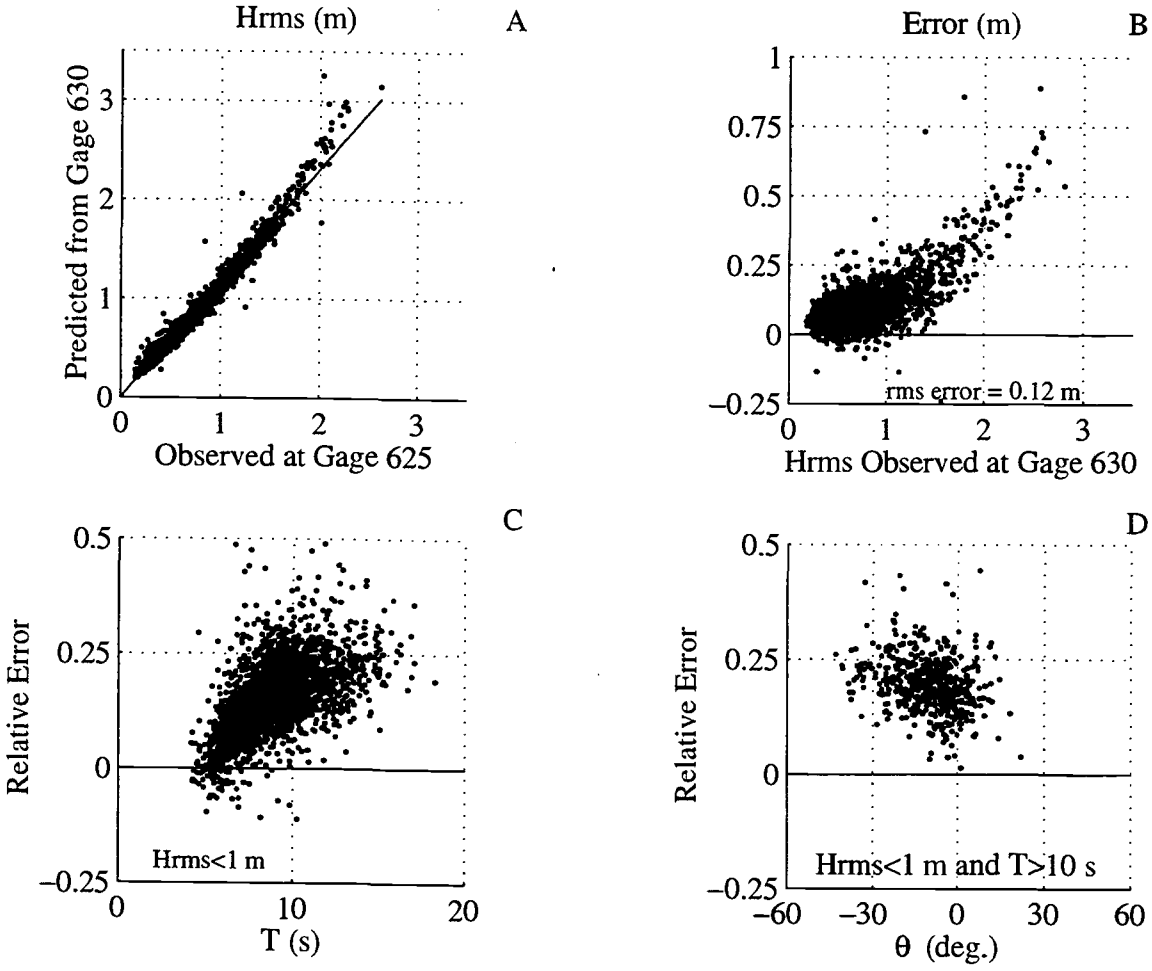

Figure IV.14. (A) Comparisons of the measured wave height at gage 625 (end of pier) and linear theory prediction (assuming normal incidence) from wave heights measured at gage 630 (4 km offshore). The best-fit linear relationship is shown as a solid line. The differences between predictions and observations are shown in (B). Relative errors (error divided by the offshore wave height) are plotted against wave period for all cases where the offshore wave height was less than 1 m (C) and were highest for long period waves, which typically approached from the south (D).

proportional to the water depth ($H_b = \gamma h_b$ and γ=0.4 was used [*Thornton and Guza*, 1982]). The wave height at breaking was estimated as

$$H_b = (\frac{F_o^2 \gamma}{g})^{1/5}, \quad (8)$$

where the constant, F_o, was evaluated at the location of a wave gage. $F_o = H_o^2 C_o \cos\theta$, H_o is the rms wave height, C_o is the wave group velocity, and θ is the angle of wave approach from shore normal.

Wave height and period were recorded at several different wave gages over the period 1981-1996. When available, we used wave heights measured by a surface piercing wave staff (gage 625) at the end of the FRF pier. This location was seaward of most bar crests. If data were not available from gage 625, we used data from an array of bottom-mounted pressure gages (collectively named gage 3111, located in approximately 8 m depth, 1 km offshore), which provided estimates of wave direction. If neither gage 625 nor gage 3111 were available, we used data from a Waverider buoy, located 4 km offshore (17 m depth) and 2 km to the south of the research pier. Wave data were also available from a wave staff located between the shore and the pier end (gage 641 at x = 219 m). Figure IV.2A shows a time series of the breaking wave height estimates. Since wave direction estimates were not uniformly available, θ=0 was assumed. Using this assumption, predictions made from gages 3111 and 630 of the shoaled wave height (non-breaking conditions) at gage 625 were in error by less than 10% (using gage 3111, Figure IV.14) and 25% (using 630, Figure IV.14).

Assuming that transient bar behavior was negligible (it was removed by detrending the bar position time series) and that the bar response time was constant, equation (2) predicts a correlation between the wave height and bar position time series. In this case, the correlation may be highest a time lag that depends on the characteristic time scales of both wave height fluctuations and bar response. Figure IV.15 shows the time-lagged cross-correlation between wave height time series and detrended bar position time series. Because

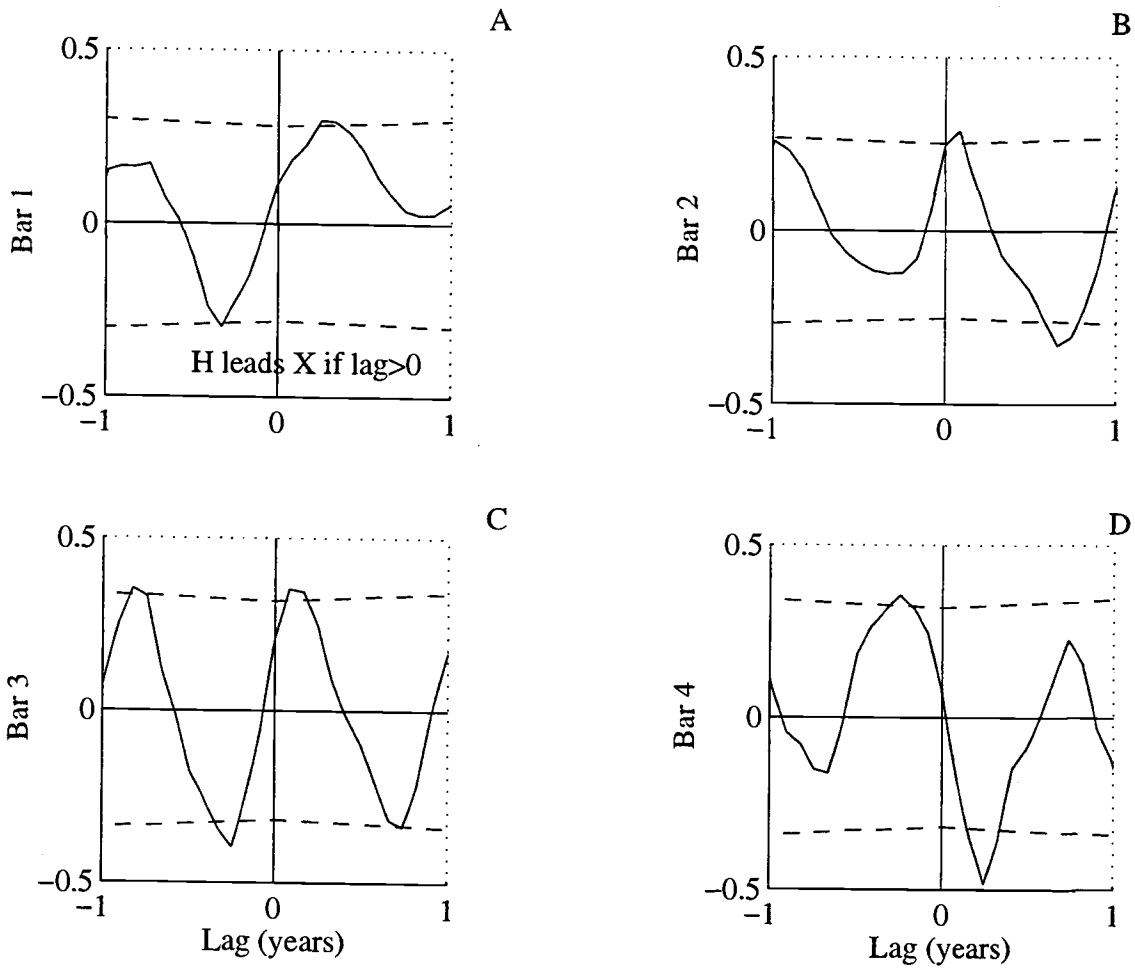

Figure IV.15. Cross-correlation between monthly-averaged wave heights and bar crest positions. Time series were detrended before the cross-correlation was estimated. Positive lags correspond to physically meaningful correlations (wave height leads bar position). The dashed lines are 95% confidence intervals, estimated according to a scheme described in Appendix B.

of the dominance of the annual cycle, we interpret the time lag (τ in months) as a phase shift such that $\phi = 2\,\pi\,\tau/12$. In all cases, there were significant correlations at lags of a few months. Bar 1 showed the highest correlation at a lag of 3 months. This corresponds to a phase lag of $\pi/2$. This is the maximum physically reasonable phase lag for bar response forced by wave height, since the forcing and response are in quadrature. This implies that

the response time of this bar was long compared to the annual cycle and that transient response could be relatively important. Bar 2 and bar 3 crest positions were both significantly correlated to wave height, at lags of 1 and 2 months. These lags correspond to normalized response times (α_1/ω) of about 2 and 0.5, respectively. If the bar response times were truly constant. transient behavior would be expected to persist for as long as several years. The response of bar 4 lagged behind the wave height fluctuations by 3 months, suggesting that forcing and response were in quadrature and that the response time was long compared to the annual cycle. Interestingly, the maximum correlation in this case was negative. Large waves were correlated with onshore migration.

The equilibrium model predictions (equation 1) of bar position changes were evaluated assuming that the bar response time depended on wave height (3a) and that the equilibrium position was proportional to the breaking wave height (3b). Estimates of bar migration rates (hereafter called bar velocities) were obtained from backwards differences of bar position time series

$$\frac{\Delta\tilde{X}_i}{\Delta t_i} = \frac{\tilde{X}_i - \tilde{X}_{i-1}}{t_i - t_{i-1}}, \tag{9}$$

where $\tilde{X}_i$ are filtered bar positions and the index i orders the bathymetric surveys. The backwards difference operation is accurate if bar position fluctuations have periods longer than $2\pi\,\Delta t$ (Δt typically 15-30 d). Bar position fluctuations with periods shorter than 60 d were removed by filtering.

Since the bar position time series was filtered, the differential equation was filtered as well. The resulting model predictions of bar velocities are

$$[\frac{\Delta\tilde{X}_i}{\Delta t_i}]_{model} = -\alpha_1[(X_c\, H_b^p)_i^\dagger - \alpha_2(H_b^{p+1})_i^\dagger], \tag{10}$$

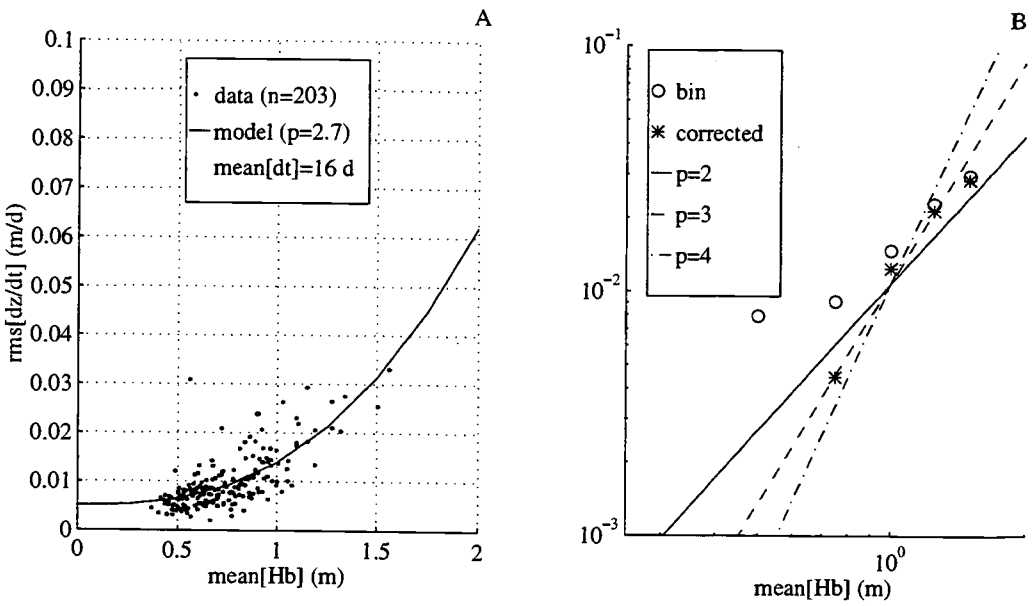

Figure IV.16. (A) Relationship between beach response rates and mean wave height. The rms response (dots) was estimated from changes in the bathymetry both north and south of the pier. Profile differences were estimated for survey pairs having a sample interval less than 60 days and at least 50% coverage of the profile between 0 and -8 m mean depths. The rms response were used to constrain the power law model (solid line): $\text{rms}[dz/dt] = 0.006 + 0.01\ \text{mean}[H_b]^p$, and was significant at better than the 95% confidence level (R^2=0.05). The exponent, p=2.7±0.5, was estimated from the log-transformed data (B). Assuming that measurement error contributed heavily to beach variability at low wave heights, the rms response rates were corrected (asterisks) by averaging the squared response within 0.2 m wave height bins and subtracting the minimum value: $\text{rms}[dz/dt]_{\text{corrected}} = (\text{rms}[dz/dt]^2_{\text{bin}} - \text{rms}[dz/dt]^2_{\text{min.}})^{1/2}$. .

where the "†" denotes products that were first filtered and then averaged over the sample interval. p=3 was used in all cases, since we observed that the response rate of beach elevation changes, defined as the rms elevation difference between surveys, increased approximately as the cube of the mean wave height between surveys (Figure IV.16).

Figure IV.17A shows the estimated bar velocities (Bar 1), plotted against wave height. A curve fit through velocities averaged within equally spaced wave height ranges (bins) indicates qualitative similarity to the pattern expected from the equilibrium model for p>0 (Figure IV.3). Low wave heights corresponded to small, onshore-directed bar velocities. Large wave heights, corresponded to large, offshore-directed velocities. The model parameters describing the response time and equilibrium position dependence on wave height, α_1 and α_2, were estimated using a nonlinear least squares method. To help interpret estimated model parameters, the results are presented in non-dimensional variables, which normalize wave height by the maximum observed height, bar position by an estimate of the surf zone width, and time by an annual cycle.

$$H^* = H_b/H_{max}, \tag{11a}$$

$$X^* = X_c /X_{sz}, \tag{11b}$$

$$t^* = t/(2\pi), \quad \text{(units for t is years)}, \tag{11c}$$

$$a_1 = \alpha_1 (2\pi) H_{max}^3 \tag{11d}$$

and

$$a_2 = \alpha_1 H_{max}/X_{sz}. \tag{11e}$$

H_{max} is a maximum wave height, estimated from the smooth time series as $\max[(H_b^{p+1}))/(H_b^p))]$. Assuming a plane beach with slope $\tan\beta$ (=1/100), X_{sz} is the surf zone width (= $\tan\beta\, H_{max}/\gamma$, where γ=0.4). Thus, if $a_1 \sim 1$, the minimum response time is about 1 year. If $a_2 \sim 1$, the equilibrium bar position corresponds to the outer edge of the surf zone.

Figure IV.17. Bar 1 velocities. The first panel (A) shows the observed (dimensional) bar velocities, plotted against the wave height. The solid line is the average velocity within equally spaced wave height bins. Error bars in (A) represent the standard error about the mean velocity in each bin. The second panel (B) compares non-dimensional observations to the equilibrium model. The model predictions of velocity are shown for a bar located at the mean position (circles) and ±1 standard deviation about the mean (-, +) (similar to Figure IV.3). The last panel (C) shows the response time estimates as a function of wave height. The parameter estimates are labeled on this plot and confidence intervals for the model parameters are in parentheses. If $a_1 = 1$, then the characteristic response time is 1 year. If $a_2 = 1$, the equilibrium bar position equals the expected surf zone width.

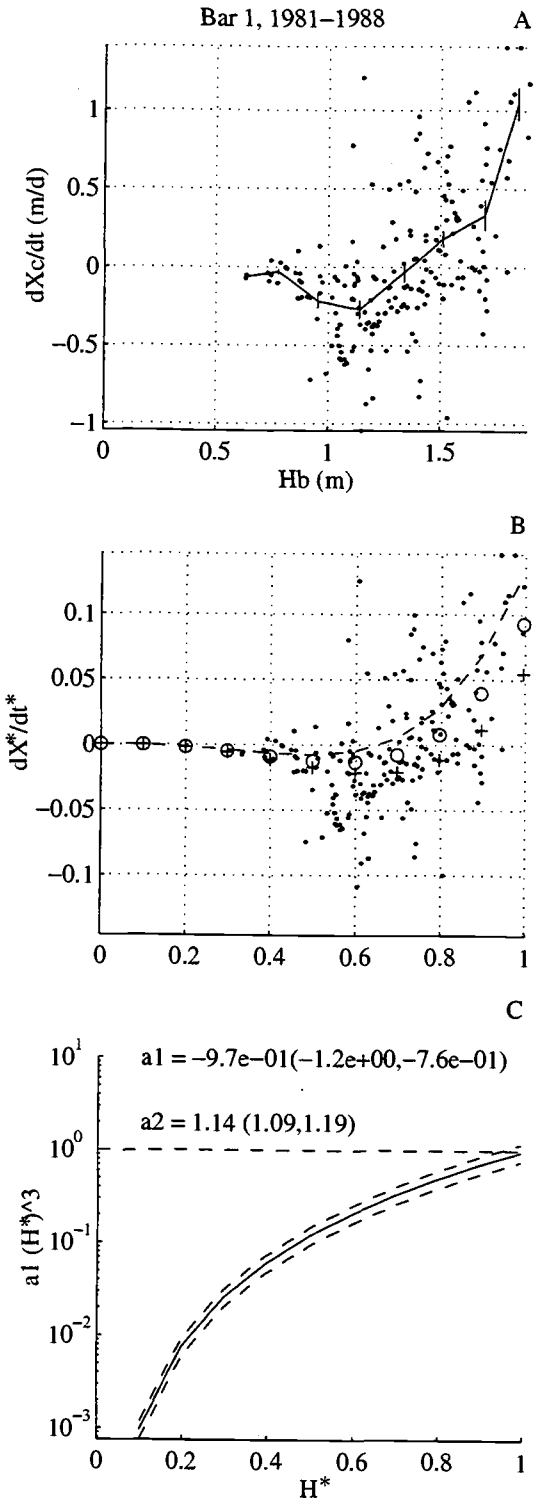
Bar 1, 1981–1988
A
dXc/dt (m/d)
Hb (m)
B
dX*/dt*
C
a1 = –9.7e–01(–1.2e+00,–7.6e–01)
a2 = 1.14 (1.09,1.19)
a1 (H*)^3
H*

Figure IV.17

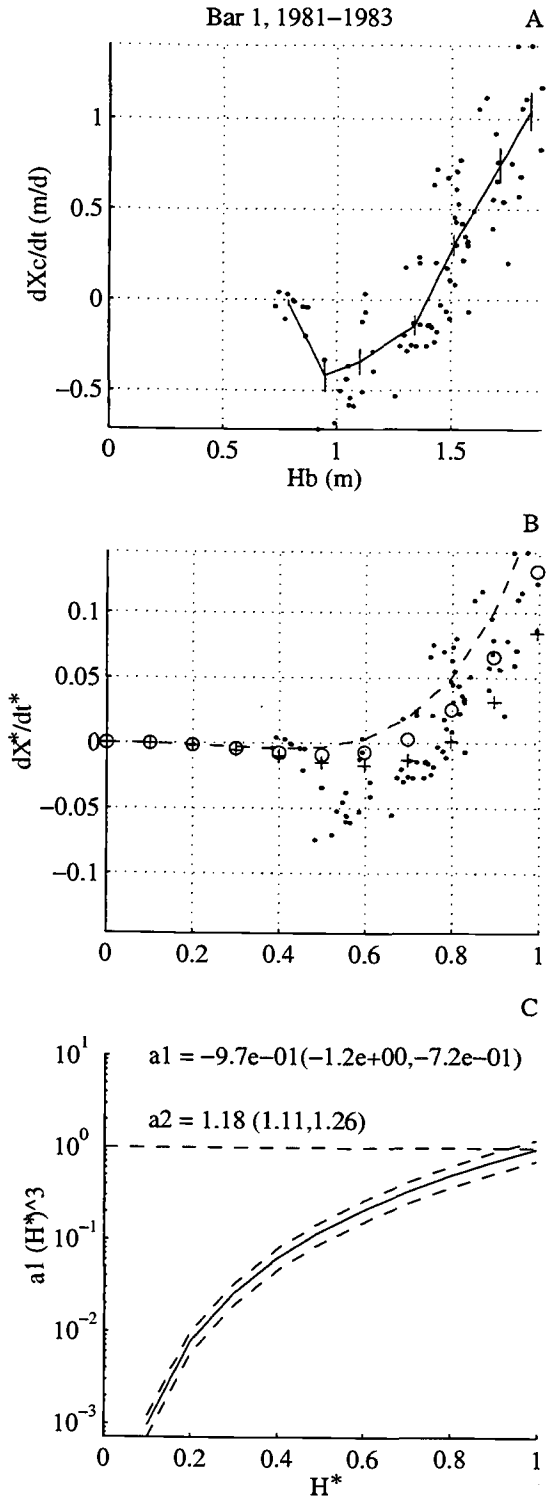

Figure IV.18. Observed and model estimates of bar 1 velocities calibrated over the period 1981-1983 (2 years).

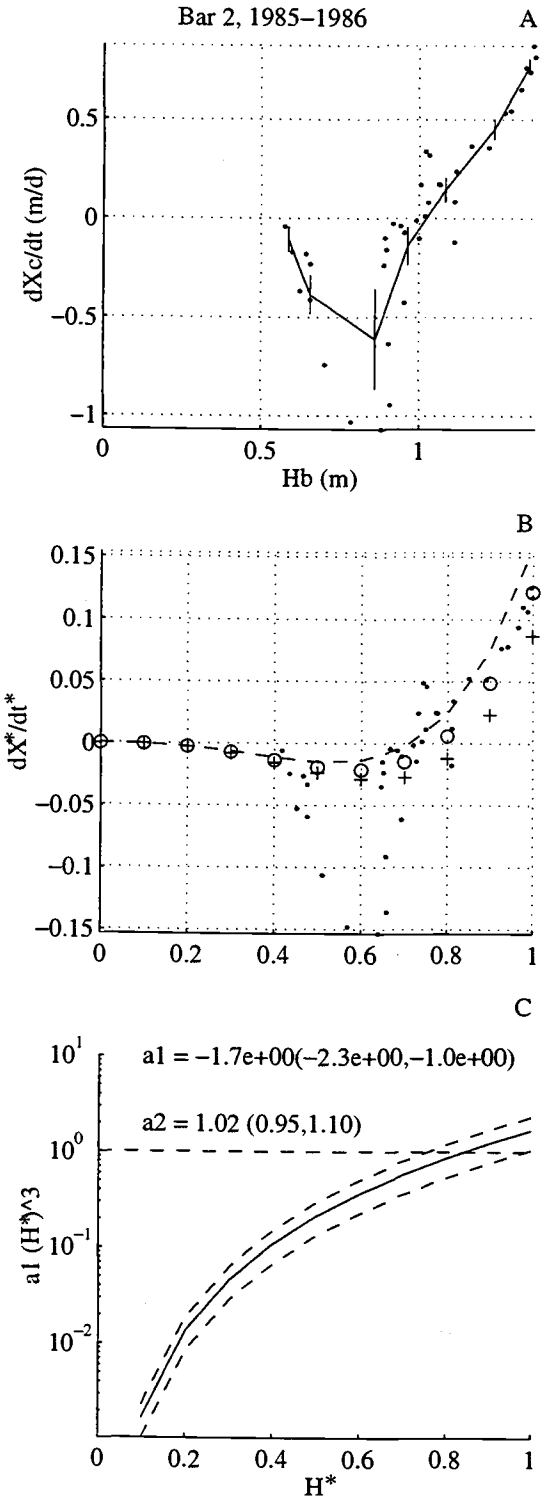

Figure IV.19. Same as Figure IV.17, but for bar 2. The wave heights were measured at gage 641 (available only for the period 1985-1986).

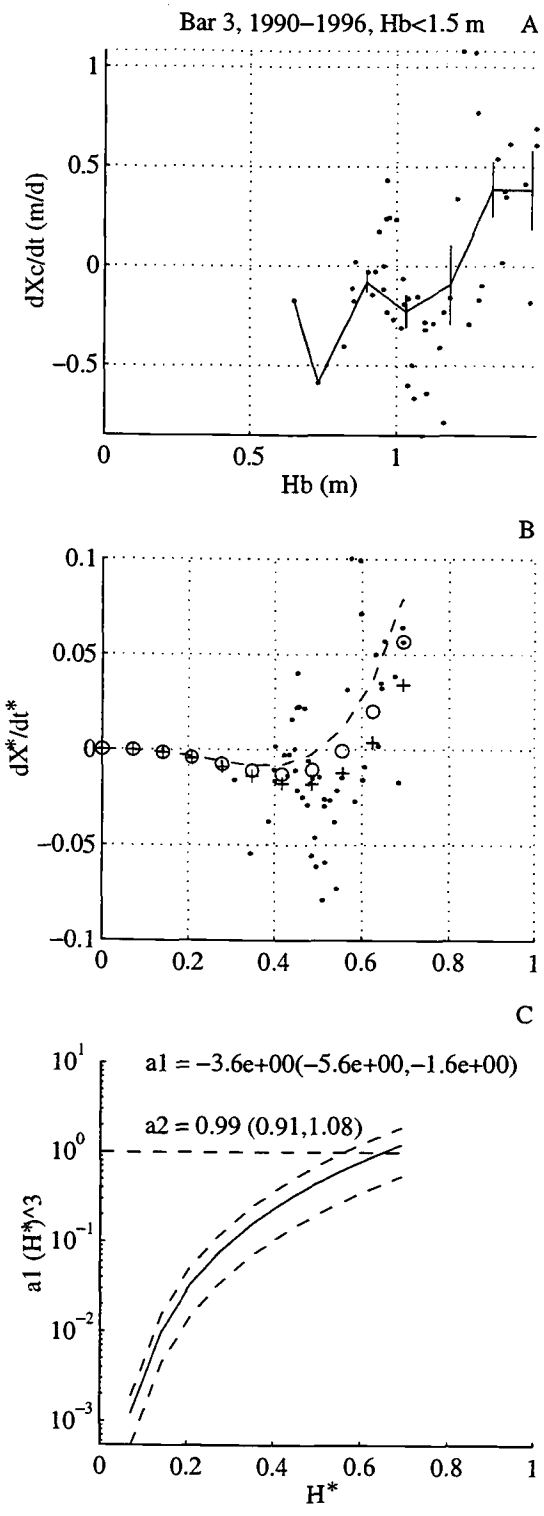

Figure IV.20. Same as Figure IV.17, but for bar 3. The wave heights were measured at gage 625 (pier end), but only heights less than 1.5 m were used.

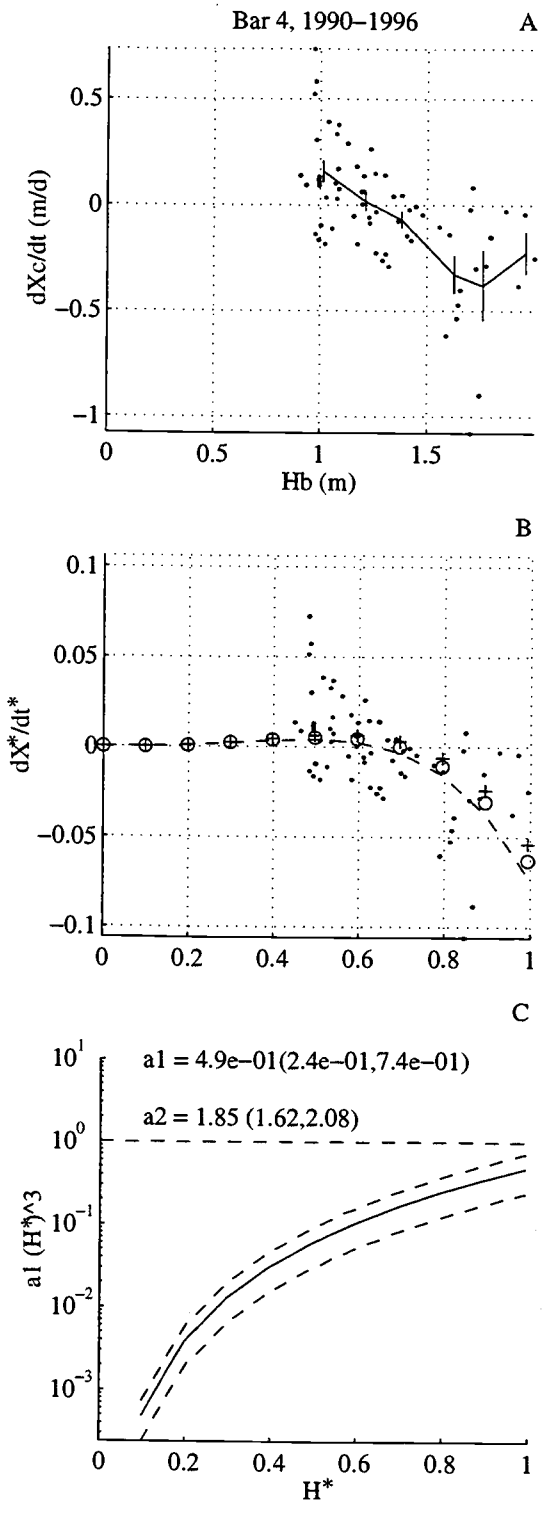

Figure IV.21. Same as Figure IV.17, but for bar4. The wave heights were measured at gage 625.

The equilibrium model explained 40% of the bar velocity variance (bar 1), and the model skill was significant at the 95% level. The model skill is the squared correlation between the predicted velocities and the observed velocities. The predicted response time (α_1) was 0.97, with 95% confidence intervals ranging from 0.76 to 1.2. The predicted equilibrium position ($X_{eq}= \alpha_2 H_b$) corresponded to the width of the surf zone, since $\alpha_2 \sim 1$). This suggests that this bar migrated toward the "break point".

The model was tested on a subset of the bar position time series comprising only observations over the period 1981-1983. During this period, the bar migrated up to 250 m offshore (half the surf zone width). Figure IV.18 shows the observed and modeled bar velocities, which depended strongly on the wave height alone. The equilibrium model skill was again significant and the estimated parameters were similar to the previous estimates. The model, however, tended to under predict the maximum onshore velocities.

We tested the model on velocity observations from the other bars as well. The tests using bars 2 and 3 were complicated because the wave heights were measured seaward of an intervening outer bar (bars 1 and 4). Thus, under high waves (higher than about 1.5 m) the wave height just seaward of the inner bars had been altered by breaking over the outer bar. Fortunately, there was a period where wave height measurements were available from a gage located just offshore of bar 2's crest (gage 641). Figure IV.19 shows the model test using these data. The model skill was significant, explaining 57% of the variance. The equilibrium position scaling was again consistent with the location of wave breaking, with an estimated response time that was half that of bar 1. This is consistent with the cross-correlation analysis.

Bar 3's crest position was seaward of the inner wave gage but onshore of Bar 4, where wave breaking occurred. Thus, the predicted wave heights were not necessarily

representative of the wave conditions in the vicinity of Bar 3. As a result, the model skill was not significant in the bar 3 case unless it was applied to mild wave conditions. The model skill was significant (25% of variance explained) when applied to bar velocities with corresponding wave heights less than 1.5 m (Figure IV.20). Again the equilibrium position scaled consistently with surf zone width. The response time estimate was about 0.3 years, which was shorter than the estimates made on the previous bars.

The equilibrium model did not fit the velocity estimates from bar 4 well (Figure IV.21). This bar was always seaward of the estimated outer edge of the surf zone. The band averaged velocity curve (Figure IV.21A) suggests a qualitative similarity to the equilibrium model in the regime where the wave heights are always smaller than the equilibrium height. The predicted bar velocities in this regime are not sensitive to changes in bar position or wave height, which may explain the non-physical estimate of a negative response time coefficient.

In a final test we used (10) to predict bar crest position time series, forced by observed wave heights. Figure IV.22 presents the results for bar 1. In all cases, the bar was initialized with the first observed position. A 4th order Runge-Kutta scheme was used to integrate the differential equation. The first example presents the results based on calibrating the model over the entire 7 years of observations. The bar crest position prediction skill was 0.77 (77% of the predicted variability was correlated to the observations). The next two examples show predictions when only the first three and last three years of observations were used to calibrate the model. Between 70% and 80% of the variance was recovered by the model. The model predicted the main features of the long-term behavior. However, it did not capture some details of the short-term fluctuations. In December 1984, for example, the observed and predicted migration have opposite signs. This is a time when the bar amplitude nearly vanished.

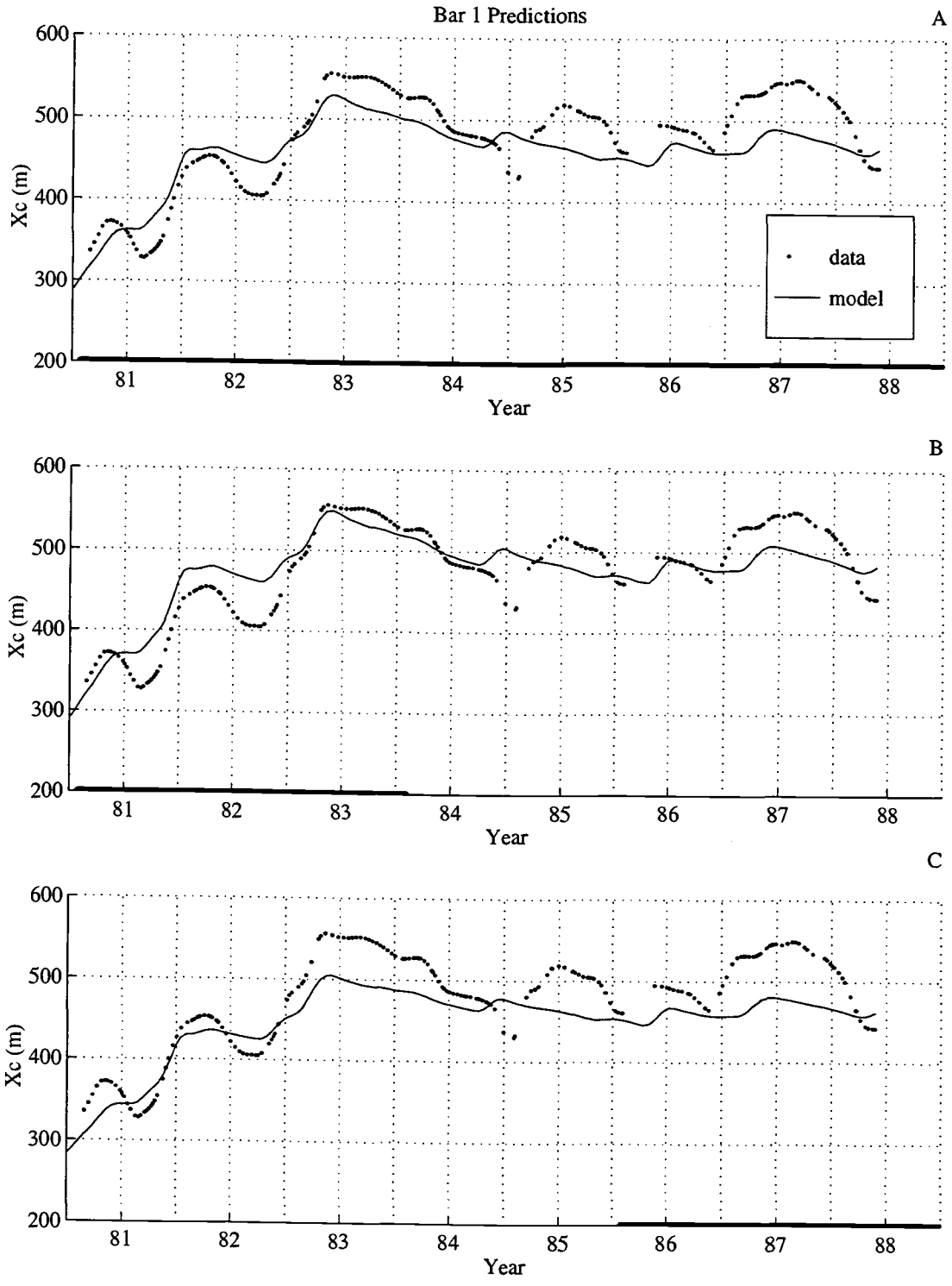

Figure IV.22. Examples of observed and predicted bar crest positions (bar 1). The 3 examples correspond to the model calibrated using all the data (A), only observations from 1981-1983 (B), and only observations from 1986-1987 (C). The calibration period is marked by a solid line along the time axis.

6. Discussion

The general form of the proposed equilibrium model (1) appears to have captured much of the relationship between nearshore forcing and cross-shore bar migration. The model has two parts. One part describes the dependence of the response time on wave height. The other part controls the direction of bar migration. It is likely that the variable response time component is relevant to descriptions of all modes of nearshore morphologic response, since the waves provide the energy to move sediment. Response time estimates from 3 of the bars ranged from 0.3 to 1 years, and an outer bar was associated with the longest response time. This suggests that outer bars may be more likely to a exhibit a transient component of response.

The break point has been suggested in previous studies as a location for bar formation [*Dally*, 1987]. This analysis suggests that existing bars migrate towards the break point. Paradoxically, wave breaking tends to be concentrated on the crests of existing bars [*Lippmann and Holman*, 1989] and patterns of breaking have been used to visually identify sand bars as they migrate both onshore and offshore. The "break point" identified in this study, therefore, requires a statistical definition such as the location where the fraction of breaking waves reaches a critical level. Wave breaking can drive processes such as undertow, which has been linked to offshore bar migration [*Thornton, et al.*, 1995].

We have ignored the generation and decay stages of the long-term bar cycles. Changes in bar amplitude potentially affect bar migration in at least two ways. *Bagnold* [1941] points out that, for fixed variation in transport across a bed form, low amplitude forms migrate faster than those with larger heights. Sandbars share this kinematic constraint. In addition, bar amplitude changes will change the water depth over bar, potentially modifying the location of the depth-dependent "break point". Potentially, two

bars located at the same cross-shore location, but having different amplitudes, could migrate in different directions. It is possible that subtle differences in bar amplitude explain the differences in the bar responses north and south of the pier.

7. Conclusions

We have analyzed 16 years of surveyed beach elevations sampled at the Army Corps of Engineers' Field Research Facility, located on the US Atlantic Coast. Surveys were conducted within a region that spanned approximately 1 km alongshore and 1 km cross-shore, and extended to depths greater than 8 m. This site typically had one or two sand bars, which varied from shore-parallel to irregular. The 16-year mean and variance of the surveyed bathymetry were mostly homogeneous in the alongshore direction, except for anomalies near a pier (variance increased by factor of 2). In the cross-shore direction, the variance was highest between the mean shoreline position and a mean depth of 3 m. Depending on cross-shore location, between 50% and 90% of this variance was explained by alongshore-uniform response over the approximately 1 km alongshore span of the surveys (omitting the central 500 m). Alongshore variability was highest near the shoreline. Greater than 80% of the elevation variance was alongshore-uniform within 300 m wide (alongshore) sub-regions to the north and south of the pier.

The incident wave height variance was dominated by frequencies at or higher than 1 cycle/year, while greater than 80% of the bathymetric variance at all cross-shore locations was explained by frequencies < 1 cycle/year. Interannual cycles consisting of sand bar formation, migration, and decay were responsible for some of the low-frequency variability. RK94 observed similar cycles in the Netherlands, where bars formed near the shoreline, migrated seaward, and decayed. In the north half of our study area, 3 out of 4 sand bars exhibited this pattern of net, over a period of about 7 years, seaward migration. However,

one sand bar appeared offshore, migrated onshore, and decayed. Similar patterns were observed in the south half, although 2 additional sand bar cycles occurred there.

An empirical, equilibrium model was formulated which explained interannual sand bar response driven by predominantly annual forcing. The model assumed that bars migrate toward an equilibrium position, scaled by wave height. The model also assumed a characteristic response time that was inversely proportional to the wave height raised to the p^{th} power ($p = 3$ yielded the best fit). If the characteristic bar response time is long relative to the time scale of the forcing, the model predicts a phase-lagged and damped response. Additionally, the wave height dependent response time shifts the mean bar position (after decay of a transient response) towards the equilibrium position associated with the maximum wave height. Thus, long response times allow transient (far from equilibrium) response to persist for many cycles of the forcing. Transient bar behavior could be introduced when bars form near the shoreline, or when outer bars decay, and inner bars face a changed wave climate. The model did not contain a mechanism for introducing these transients.

Two free parameters, the response time and equilibrium position coefficients, were estimated by minimizing the squared deviation between the equilibrium model and the observed bar velocities. The calibrated model explained between 25% and 57% of the bar velocity variance, corresponding to 3 of the sand bars in the north half of the study area. The estimated response times for all 3 bars varied between 0.3 and 1 times the dominantly annual time scale of the forcing. Outer bars had longer response times. The estimated equilibrium position was consistent with a break point position. When the calibrated model was initialized with an observed bar position, and then forced with measured wave heights, it predicted up to 80% of the observed bar position variability.

CHAPTER V:
THE ROLE OF MORPHOLOGIC FEEDBACK IN SURF ZONE SAND BAR RESPONSE

1. Abstract

Using bathymetric surveys, sampled monthly over a 16 year period at the Army Corps of Engineers' Field Research Facility (North Carolina), we have characterized surf zone sand bar response to changing wave conditions. Bar response was defined by changes in position, amplitude, or length scale. These parameters were described objectively using a model of the commonly double-barred beach profiles comprising Gaussian-shaped bars, which were added to a planar slope. The rms error between alongshore-averaged bathymetry and the profile model was 0.10 m (estimated over 322 different surveys), which was small compared to the bathymetric variability associated with sand bars (rms elevation ~ 1 m).

The profile model was used to estimate sediment transport patterns associated with profile response. Transport patterns associated simply with the migration and growth of Gaussian-shaped bars were compared to the total transport in the vicinity of individual sand bars. The correlation between predicted and observed patterns was typically high (squared correlation > 0.9). The magnitude of transport variations over a bar and the ratio of transport associated with bar migration to bar growth or decay were compared to a simple parameterization of nearshore hydrodynamics. This parameter, γ_{crest}, was the ratio of the rms wave height to water depth, estimated at bar crest locations using a simple shoaling model. The transport magnitude was estimated as the standard deviation of the transport in the vicinity of a bar crest. In 3 out of 4 cases, the transport magnitude increased monotonically as γ_{crest} increased. The ratio of transport associated with bar migration to that associated with bar decay was described in terms of a phase shift between bar form and

transport pattern. Estimates of this phase shift were typically bi-modally distributed, corresponding to bar response dominated by onshore and offshore migration. At low values of γ_{crest}, bars migrated onshore and their amplitude tended to decay. At high values of γ_{crest}, bars migrated offshore, with relatively little change in amplitude. The value of γ_{crest} dividing onshore and offshore migration was consistent with the onset of wave breaking.

Because transport patterns were correlated to the bathymetry, and because the nature of this correlation depended on a local measure of the hydrodynamic conditions, it is concluded that morphologic feedback played an important role in governing bar response. However, feedback did not appear to play the commonly assumed role of driving the profile towards an equilibrium state (negative feedback). This statement is made based on the observation that the magnitude of bar response (the sediment transport magnitude) increased monotonically as γ_{crest} increased, in spite of the fact that the direction of bar migration changed. Neutral feedback was likely, especially under non-breaking (low γ_{crest}) conditions. Potentially, neutral feedback was responsible for the demise of outer bars.

2. Introduction

The concept of "morphologic feedback" has played an important role in the development of both conceptual and quantitative models of beach profile response. Morphologic feedback is a term for the component of morphologic response that depends on the morphology itself. In the near shore environment, morphologic feedback results because hydrodynamic processes driving sediment transport usually depend on the bathymetry. Gradients in sediment transport lead to changes in the bathymetry. A feedback loop is completed as hydrodynamic processes respond to the modified bathymetry.

Morphologic feedback is inherent if sediment transport depends on bottom slopes. A typical assumption is that beach morphology reaches an equilibrium (steady) state when the tendency for net, wave-driven transport due to steady wave conditions balances down slope transport [*Bowen*, 1980; *Bowen and Huntley*, 1984]. Down slope transport results from "stirring" by orbital wave motions, while net transport can be driven by mean currents or skewed current distributions. For the case of 3-dimensional morphology, residual transport may result from circulation patterns, but the transport divergence is everywhere zero. The problem of estimating equilibrium morphologies is typically linearized, such that the superposition of different processes (e.g., incident waves, edge waves, longshore currents) yields an equilibrium morphology that is simply the superposition of the equilibrium morphologies associated with each process. The problem with this is that all processes ought to respond to the total bathymetry, not just one component [*Bowen and Huntley*, 1984].

Implicit in many attempts to predict beach evolution is the assumption that equilibrium morphologies are stable. That is, steady offshore wave conditions combined with morphologic feedback drive profiles towards equilibrium. This requires negative feedback such that morphologic response tends to re-establish the sediment transport balances associated with equilibrium. Alternatively, morphologic feedback may be neutral, such that response has no affect on transport patterns. An example is the migration of ripples in a steady current, such as river flow. Once the ripples have developed, they migrate down stream at a steady rate. In this case, the bed forms are clearly stable, but the bed itself continues to evolve. Feedback can be positive, as well. In this case, morphologic evolution enhances transport gradients, driving the morphology away from an equilibrium state. The growth of bed forms from an initially smooth bed is one example of positive feedback [*Smith*, 1970; *McLean*, 1990]. Although we suspect that feedback is important, the role actually played by morphologic feedback in beach evolution is not well described. In

particular, it is far from clear that the variety of identified feedback mechanisms [*Roelvink and Stive*, 1989; *Holman and Sallenger*, 1993], as well as observations of beach behavior, are always consistent with the negative feedback premise.

Surf zone sand bars are shore-parallel, rhythmic, or irregular sand ridges, which typically respond to fluctuations in the incident wave conditions [*Sonu*, 1968; *Short*, 1975; *Wright and Short*, 1984]. Morphologic feedback almost certainly affects surf zone sand bar evolution. Variations of fluid processes and sediment transport over a bar can be extreme. Wave breaking, for example, tends to be concentrated near bar crests and likely plays an important role in driving sediment transport over bars. Changes in bar position or amplitude affect spatial patterns of wave breaking, likely modifying the sediment transport over bars. However, changes in breaking patterns, and other processes, also depend on changes in the incident wave conditions. Previous studies of sand bar response have not always teased apart the effects of changing morphology from those of changing wave conditions.

The goal of this paper is to describe the role played by morphologic feedback in controlling bar response. Here, bar response is assumed to include changes in bar position, amplitude, and length. Our approach is to describe how spatial patterns of sediment transport are related to the bar form, and then to describe how this relationship depends on a parameterization of the processes which may drive sediment transport. This parameterization is the ratio of wave height to water depth, estimated at the bar crest, which depends on both incident wave conditions and the configuration of the barred profile. In section 2, a cross-shore beach profile model is defined that can be used to estimate the cross-shore transport associated with temporal changes in the profile. The model includes objective definitions of sand bars, and is used to develop relevant characterizations of the transport patterns associated with bar response. In section 3, we describe how this model

was fit to a series of beach surveys obtained at the Army Corps of Engineers' Field Research Facility (FRF). The relationship between transport patterns, sand bars, and γ_{crest}, is described in section 4. In section 5, we discuss the role that morphologic feedback played in governing bar response.

3. Sandbar model

3.1 Profile model

Sand bar response has been described simply by changes in bar crest position [*Birkemeier*, 1985; *Lippmann and Holman*, 1990; *Lippmann, et al.*, 1993; *Ruessink and Kroon*, 1994; *Plant, et al.*, in review], neglecting or making assumptions about changes in bar amplitude, length, or other measures of bar shape. A more complete description of bar response includes some measure of bar shape. In spite of having a fixed spatial structure, Gaussian profiles have well defined positions, amplitudes, and lengths. Although not a unique representation, a barred beach profile can be constructed from several Gaussians, superimposed upon a monotonic profile, such as a plane beach (Figure V.1A).

$$\hat{Z}(x,t) = b_0(t) + b_1(t)\,x + \sum_{m=1}^{M} A_m(t)\exp\left[-\left(\frac{x-X_m(t)}{L_m}\right)^2\right] + A_s(t)\exp\left[-\left(\frac{x-X_s}{L_s(t)}\right)^2\right], \qquad (1)$$

where x is the distance increasing offshore, t is the time, b_0 and b_1 describe the plane beach, A_m, X_m, and L_m are objective definitions of the amplitude, position, and length of the m^{th} bar. Bar lengths are assumed constant in time. A_S, X_S, and L_S are the parameters describing an additional Gaussian placed at the shore (constant position) in order to fit the intertidal and subaerial portion of a profile.

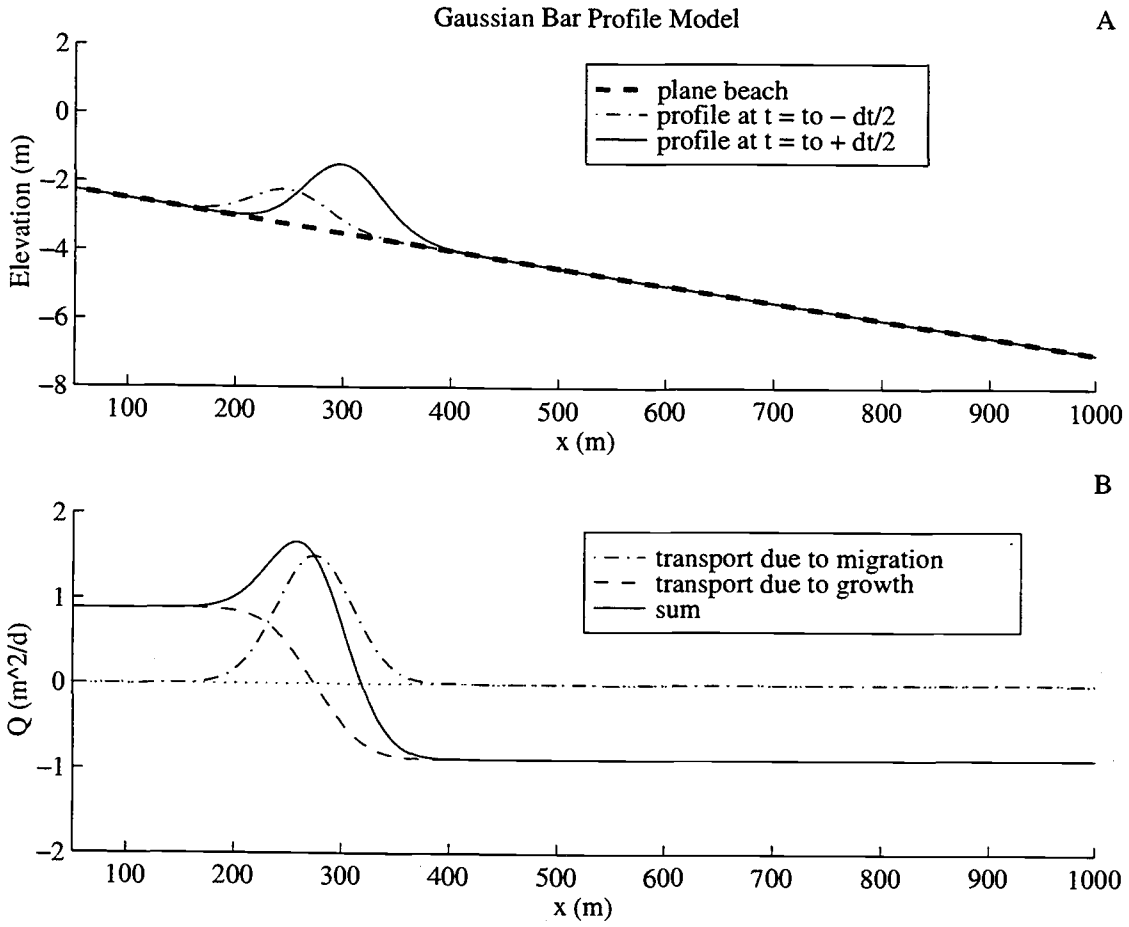

Figure V.1. Beach profile model, showing (A) Gaussian shape profiles added to a plane beach. The model is shown at two times (t=t0-Δt, t=t0+Δt), during which the bar migrated offshore and its amplitude increased. The bottom panel (B) shows the sediment transport patterns (at t=t0) that correspond to bar migration and bar growth.

3.2 Related sediment transport patterns

This morphologic model can be used to estimate cross-shore sediment transport patterns over an evolving beach profile. An equation for one-dimensional sediment conservation relates the gradients in cross-shore sediment transport to the change in the beach profile.

$$\frac{\partial Q}{\partial x} = -\frac{\partial Z}{\partial t}, \qquad (2)$$

where, Q is the depth integrated transport (a volume flux per unit width, e.g., m^2/d), corrected for the porosity of the bed. A simple expression for the transport at $t=t_0$ can be related to the profile parameters if they vary linearly in time,

$$b_0(t) = b_0(t_0)\,[1 + (t-t_0)\,\beta_0(t_0)], \tag{3a}$$

$$b_1(t) = b_1(t_0)\,[1 + (t-t_0)\,\beta_1(t_0)], \tag{3b}$$

$$A_m(t) = A_m(t_0)\,[1 + (t-t_0)\,\alpha_m(t_0)], \tag{3c}$$

$$X_m(t) = [X_m(t_0) + (t-t_0)\,C_m(t_0)], \tag{3d}$$

$$A_s(t) = A_s(t_0)\,[1 + (t-t_0)\,\alpha_s(t_0)], \tag{3e}$$

and

$$L_s(t) = L_s(t_0)\,[1 + (t-t_0)\,\lambda(t_0)], \tag{3f}$$

and bar amplitudes vary slowly (i.e., $(t-t_0)\,\alpha_m(t_0) \ll 1$). The flux profile is obtained by inserting (1), with substitutions (3a)-(3f) into (2), integrating over x, and evaluating at $t = t_0$.

$$Q(x,t_0) = -\beta_0(t_0)\,b_0(t_0)\,x - \beta_1(t_0)\,b_1(t_0)\,\frac{x^2}{2} + \sum_{m=1}^{M} Q_m(x,t_0)$$

$$+ Q_s(x,t_0) + \text{const}(t_0), \tag{4a}$$

where the constant satisfies a boundary condition. For instance, the transport at the offshore boundary is typically assumed to be zero. The terms Q_m and Q_s correspond to the transport resulting from changes in the Gaussian bars

$$Q_m(x,t_0) = A_m(t_0)\,\{C_m(t_0)\,\exp[-(\frac{x - X_m(t_0)}{L_m})^2]$$

$$- \frac{\sqrt{\pi}}{2}\,\alpha_m(t_0)\,L_m(t_0)\,\text{erf}[(\frac{x - X_m(t_0)}{L_m})]\} \tag{4b}$$

and the shoreline

$$Q_S(x,t_0) = A_S(t_0)\ \{\lambda(t_0)\ (x-X_S)\ \exp[-(\frac{x - X_S}{L_S(t_0)})^2]$$

$$-\frac{\sqrt{\pi}}{2}\ L_S(t_0)\ \lambda(t_0)\ \mathrm{erf}[(\frac{x - X_S}{L_S(t_0)})]$$

$$-\frac{\sqrt{\pi}}{2}\ \alpha_S(t_0)\ L_S(t_0)\ \mathrm{erf}[(\frac{x - X_S}{L_S(t_0)})]\}. \qquad (4c)$$

Equation 4b has two terms. The first term describes the transport resulting from the migration of a Gaussian-shaped bar having a fixed amplitude. This transport is also Gaussian shaped and has the same length as the bar (Figure V.1B). The sediment transport pattern associated with unchanging, arbitrarily-shaped bed forms share this property of similarity [*Bagnold*, 1941]. The amplitude of the resulting transport pattern depends only on bed form height and speed. The second term in (4b) is the transport associated with a growing or decaying Gaussian bed form, having a fixed position. This transport term depends on the bar growth rate and length. The cross-shore transport pattern is described by the error function, which is essentially a phase-shifted version of the original bed form.

Over a bar length (taken as $\pm 2L_m$), the transport pattern associated with bar growth/decay (an odd function) is uncorrelated to the transport associated with migration (an even function). In analogy to a Fourier representation, we have defined the transport associated with bar growth and migration in terms of a magnitude and phase shift

$$Q_m(x,t_0) = b_m(t_0)\ \{\cos[\phi_m(t_0)]\ \exp[-(\frac{x - X_m(t_0)}{L_m})^2]$$

$$-\sin[\phi_m(t_0)]\ \mathrm{erf}[(\frac{x - X_m(t_0)}{L_m})]\} \qquad (5)$$

where

$$\phi_m(t_0) = \tan^{-1}[\frac{\sqrt{\pi}}{2}\ \alpha_m(t_0)\ L_m / C_m(t_0)] \qquad (6)$$

and

$$b_m(t_0) = A_m(t_0)\{(\frac{\sqrt{\pi}}{2}\alpha_m(t_0)\,L_m)^2 + C_m(t_0)^2\}^{1/2}. \quad (7)$$

The sediment transport phase shift describes the location of the sediment transport maximum relative to the bar crest. A phase shift of 0 implies that the transport maximum lies over the bar crest, corresponding to offshore migration. Likewise, a phase shift of π corresponds to onshore migration. Phase shifts of $\pm\pi/2$ correspond to bar growth or decay. b_m is a measure of the spatial variation in sediment transport over a bar crest due to both migration and growth, and describes the magnitude of bar response.

An additional measure of profile response is the transport magnitude associated with changes in all of the profile parameters. The transport magnitude is defined as the standard deviation of the transport

$$B_m(t_0) = \mathrm{var}[Q]^{1/2} \quad (8)$$

estimated over $X_m(t_0)\pm 2L_m$. If changes in the plane beach component of the profile are small and bars are well separated (i.e., crests separated by a distance exceeding 2 L_m), then $\mathrm{var}[Q_m] \sim B_m^2$. On the other hand, if changes in the plane beach component are large, or bars are not well separated, then $\mathrm{var}[Q_m] < B_m^2$. The correlation, over $\pm 2L_m$, between Q_m and the total transport, Q, measures the degree to which bars evolve as isolated, Gaussian-shaped features, with fixed length scale. The squared correlation represents the fraction of sediment transport variance over a bar that is correlated with the isolated bar model

$$R_m(t_0) = \{\mathrm{covar}[Q_m(t_0), Q(t_0)]\}^2 / B_m^2(t_0)\,\mathrm{var}[Q_m(t_0)]. \quad (9)$$

4. Sandbar observations

4.1 Profile data

The data set used to examine bar response and morphologic feedback consists of 16 years of surveyed beach profiles that have been collected since 1981 at the Army Corps of Engineers Field Research Facility (FRF). The surveys were sampled on bi-weekly to monthly intervals over a region spanning approximately 1 km alongshore and 1 km offshore (to at least 8 m water depth). Cross-shore profiles, separated by approximately 40 m alongshore, were sampled by the Coastal Research Amphibious Buggy (CRAB), which has a 10 m footprint and survey precision of about 10 cm in the vertical [*Birkemeier and Mason*, 1984]. Bi-weekly surveys were available along only two transects at the southern end of the study area (y = -92, 0 m) and two at the northern end (y = 1006, 1096 m). Figure V.2 shows a contour map and two cross-shore profiles generated from a typical survey.

Plant et al. [in review] quantified the spatial and temporal variability of the bathymetric data set. They showed that over 80% of the variability was alongshore-uniform within 300 m wide (alongshore) regions, which were more than 200 m from a research pier. Bathymetric variability near the pier was anomalous (Figure V.2A). Our analysis focuses only on the region north of the research pier. Alongshore-uniform variability at the FRF site was attributed to the migration of surf zone sand bars, which have been discussed by others [*Birkemeier*, 1985; *Lippmann and Holman*, 1990; *Lippmann, et al.*, 1993; *Plant, et al.*, in review]. In addition to migration, bar growth and decay were clearly important on interannual time scales, in association with cycles consisting of inner bar formation, followed by a period dominated by onshore and offshore migration, a transition to an outer bar, and eventual bar decay. This cycle was completed over a period of nearly a decade.

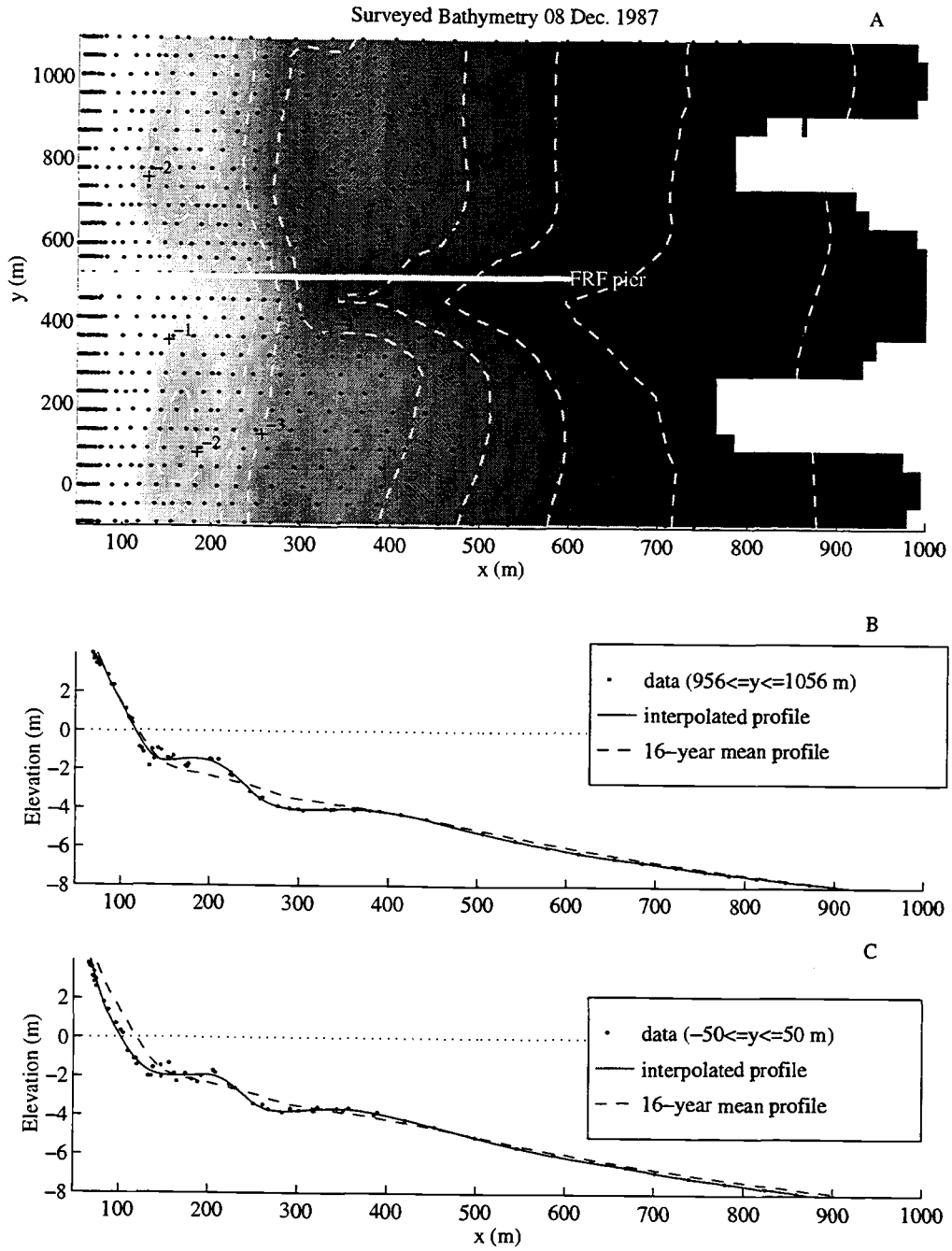

Figure V.2. Contour map (A) and cross-shore profiles (B-C) generated from CRAB survey on 8 December 1987. The alongshore direction (y coordinate axis) points approximately 20° west of north, and the cross-shore direction is approximately shore-normal. The contour interval is 1 m. The cross-shore profiles were extracted along one line north of the pier (y = 1006 m) and one line south of the pier (y = 0 m). Two nearly shore-parallel bars are located at x = 200 m and x = 375 m. An objective interpolation scheme was used to generate the gridded bathymetry analyzed in this paper.

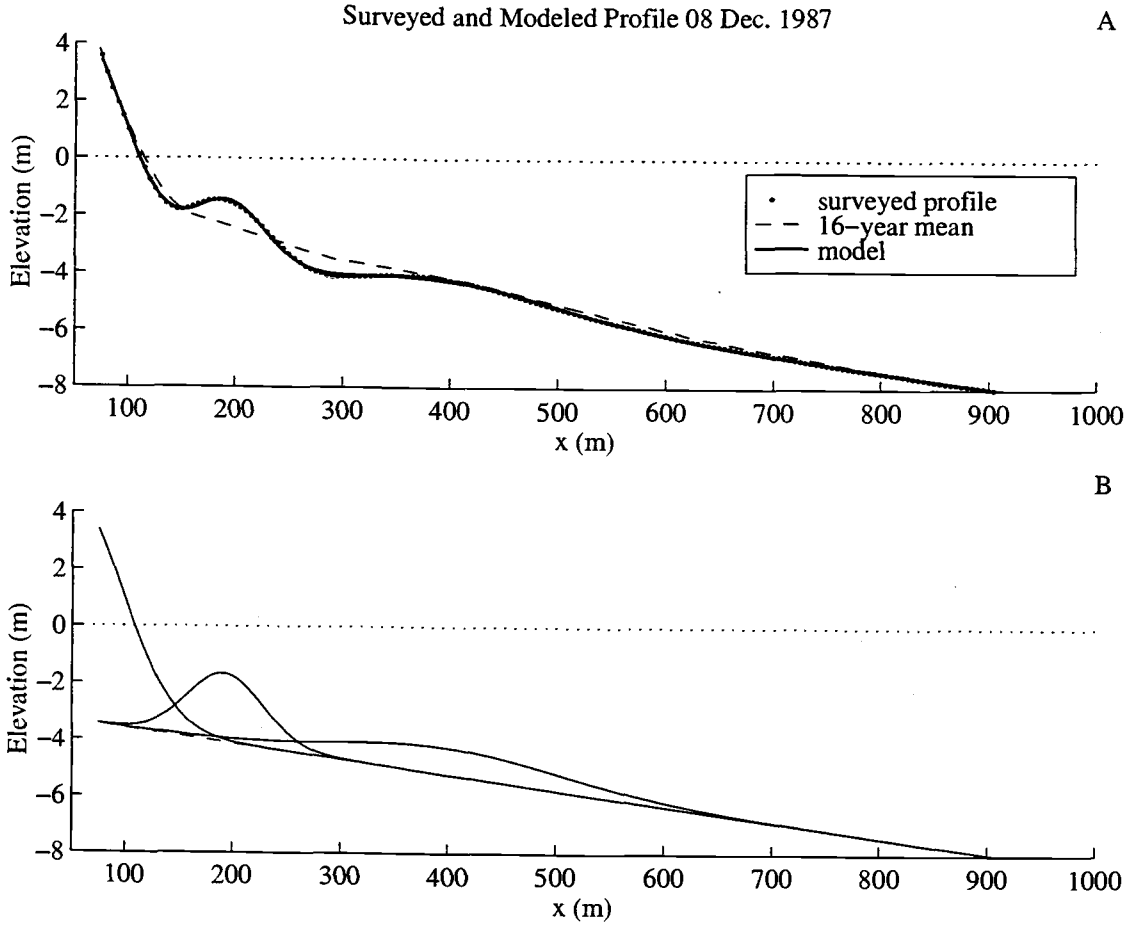

Figure V.3. Comparison between surveyed and model bathymetry (8 December 1987) showing (A) the surveyed bathymetry (alongshore-averaged) and the model fit to the survey data. The rms error in this example was 0.03 m. The lower panel (B) shows the four components of the model: a shoreline "bar", inner bar, outer bar, and plane beach.

4.2 Modeling the profiles

The simple profile model (1) was fit to alongshore-averaged profiles (Figure V.3) by choosing the profile parameters which minimized the squared deviation between model and observed profiles. Profile data between -8 m (relative to National Geodetic Vertical Datum, 1929) and +4 m were used and the model was fit to each of 322 surveys. Eight parameters were estimated (b_0, b_1, A_1, X_1, A_2, X_2, A_S, L_S). The position of the shoreline

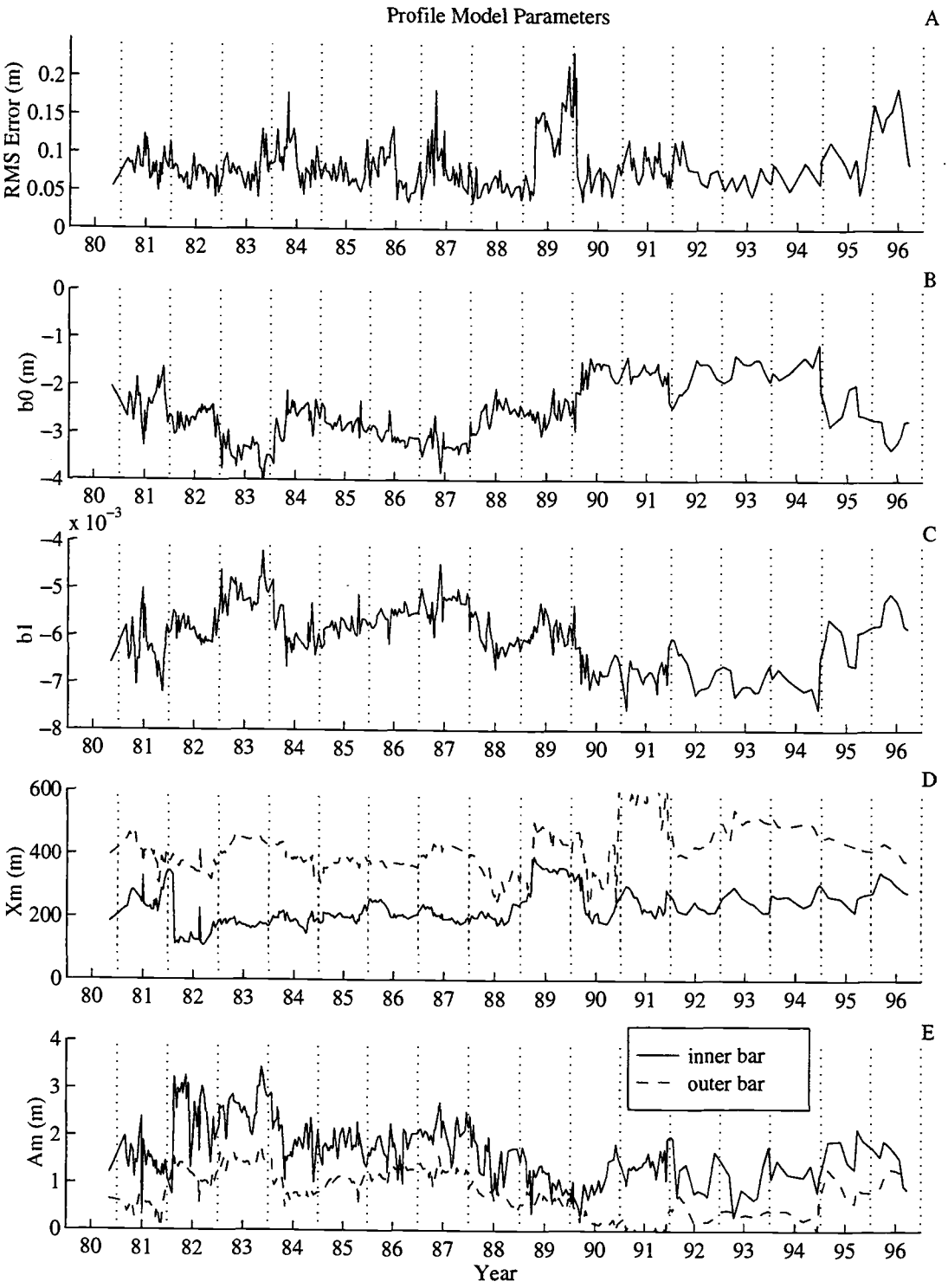

Figure V.4. Time series of model parameters. The top panel (A) shows the rms error between surveyed and model profiles. The rms error was estimated over all observations with elevations between -8 m and +4 m NGVD. The rms error was highest in December 1989, corresponding to a bar transition period. The other parameters are the intercept (B) and slope (C) of the plane beach component, and the bar position (D) and amplitude (E).

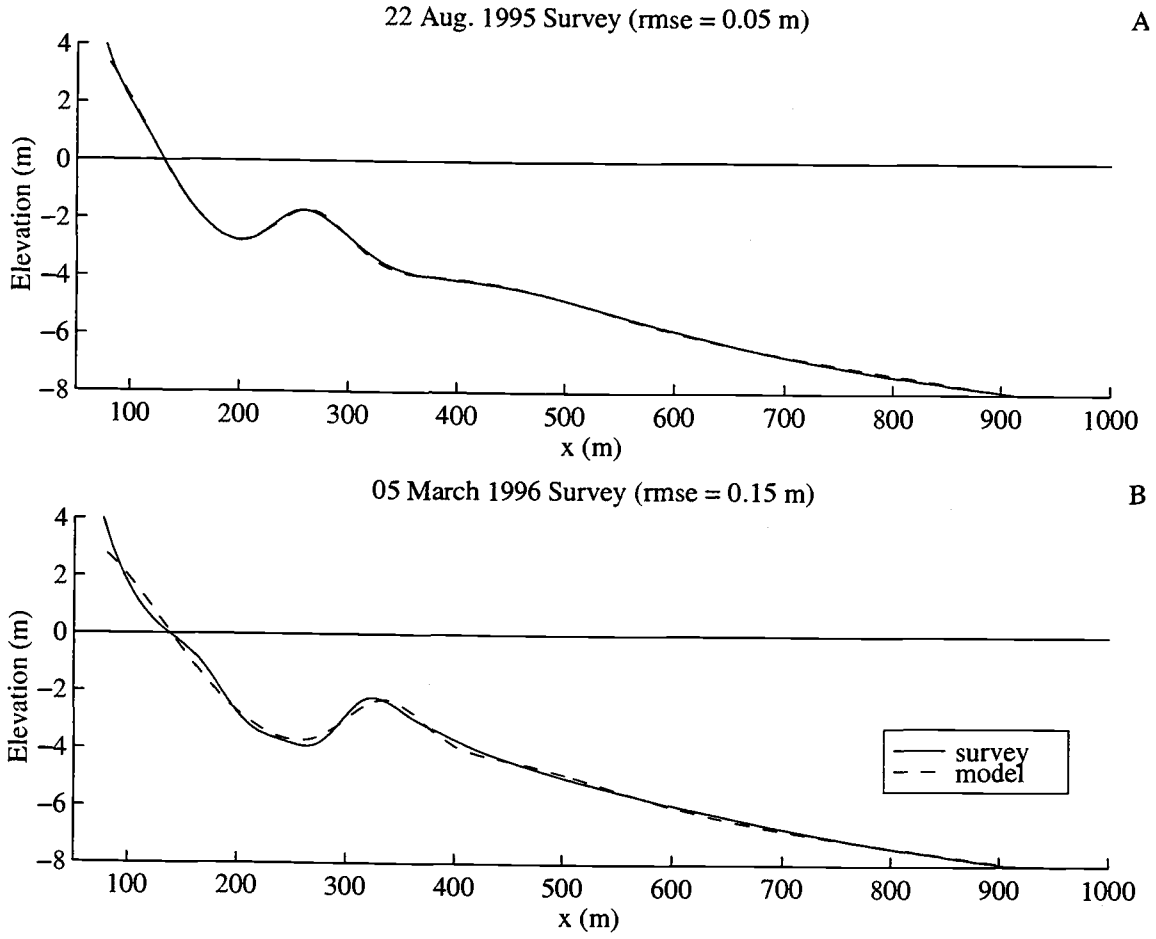

Figure V.5. Profile errors increased when well-separated bars (A) merged (B), forming an asymmetric profile.

Gaussian was fixed (X_S = 50 m), and its amplitude and length were allowed to vary. The lengths of the inner and outer bars were fixed at the mean values (determined from an analysis that allowed these parameters to vary) of 200 for inner bars and 600 m for outer bars. Since the profile model is nonlinear in parameters X_m and L_S, all parameters were estimated iteratively (nonlinear regression), initialized with the estimates corresponding to a preceding survey.

An F-test was performed and verified that the addition of each Gaussian bar contributed significantly to the model performance. The rms error over all data was 0.09 m. The rms error over any one profile never exceeded 0.23 m, and the rms errors associated with 90% of the profiles were less than 0.12 m (Figure V.4A). These errors were small, relative to the variance explained by the model. There were two periods when the rms error was relatively high (much of 1989 and 1996). In 1989, the outer bar had merged with the inner bar, producing an asymmetric bar form. The simple 2-bar profile model fit the asymmetric bar form imperfectly, requiring significant overlap of the inner and outer Gaussians. At the same time, a new inner bar began to form near the shoreline, which required an additional (but unavailable) Gaussian in the model. In 1996, the inner bar and outer bar merged and, again, became very asymmetric (Figure V.5).

5. Analysis of sandbar response

5.1 Parameterization of the forcing

Previous work has demonstrated that some aspects of bar response may be correlated to simple parameterizations of the incident wave forcing [*Aubrey, et al.*, 1980; *Wright, et al.*, 1985; *Lippmann and Holman*, 1990]. A non-dimensional wave height has often been used, and has typically been interpreted as a measure of dissipative or reflective wave conditions. Dissipative conditions correspond to significant dissipation of incident wave energy through breaking, which transfers energy to, for example, mean currents [*Bowen*, 1969; *Longuet-Higgins*, 1970] and infragravity waves [*Thornton and Guza*, 1982]. Reflective conditions are associated with the dominance of incident-frequency processes.

The ratio of the rms wave height to water depth over a bar crest (γ_{crest}) is a simple parameterization of the local hydrodynamic conditions. The rms wave height is useful for

describing the local distribution of observed wave heights, which are typically well described by a Rayleigh distribution. The intensity of breaking is typically proportional to γ_{crest} [*Thornton and Guza*, 1983]. Here, the term "intensity of breaking" refers to the fraction of locally breaking waves. Because wave heights become saturated (depth limited) in the surf zone, γ_{crest} likely reaches a maximum value [*Thornton and Guza*, 1982]. According to previous studies at the FRF site, maximum observed value of γ_S (the maximum ratio of rms wave height to depth) ranges from 0.25 to 0.4 [*Sallenger and Holman*, 1985; *Sallenger and Howd*, 1989; *Haines and Sallenger*, 1994]. γ_S has been shown to depend on the local beach slope and water depth [*Raubenheimer*, 1996]. γ_{crest} is potentially sensitive to profile changes (hence the potential for feedback), since the local wave height depends on the offshore wave height, the path over which the waves shoal or break, and the local water depth.

Over the 16-year period spanned by beach surveys, significant wave height and peak periods were recorded by several wave gages (Figure V.6). The wave gages were not necessarily located over bar crests. Thus, a simple shoaling-breaking wave model [*Thornton and Guza*, 1983] was used to estimate the rms wave height across the entire cross-shore profile landward of a wave gage used to initialize the model. Shoaling in the wave model was assumed energy flux conservation applied to a narrow-band (in frequency), random wave field. Breaking was based on dissipation in periodic bores. The shoaling model required two free parameters, which have been calibrated previously at the FRF [*Haines and Sallenger*, 1994]. We use their values for wave height saturation (γ_{model} = 0.34) and efficiency of dissipation (β=0.8). *Haines and Sallenger* [1994] point out that the values of these tuning parameters leading to the smallest error between the modeled and observed rms wave height differ at different cross-shore locations, which is expected based on observed variability of γ_S [*Sallenger and Holman*, 1985; *Raubenheimer*, 1996].

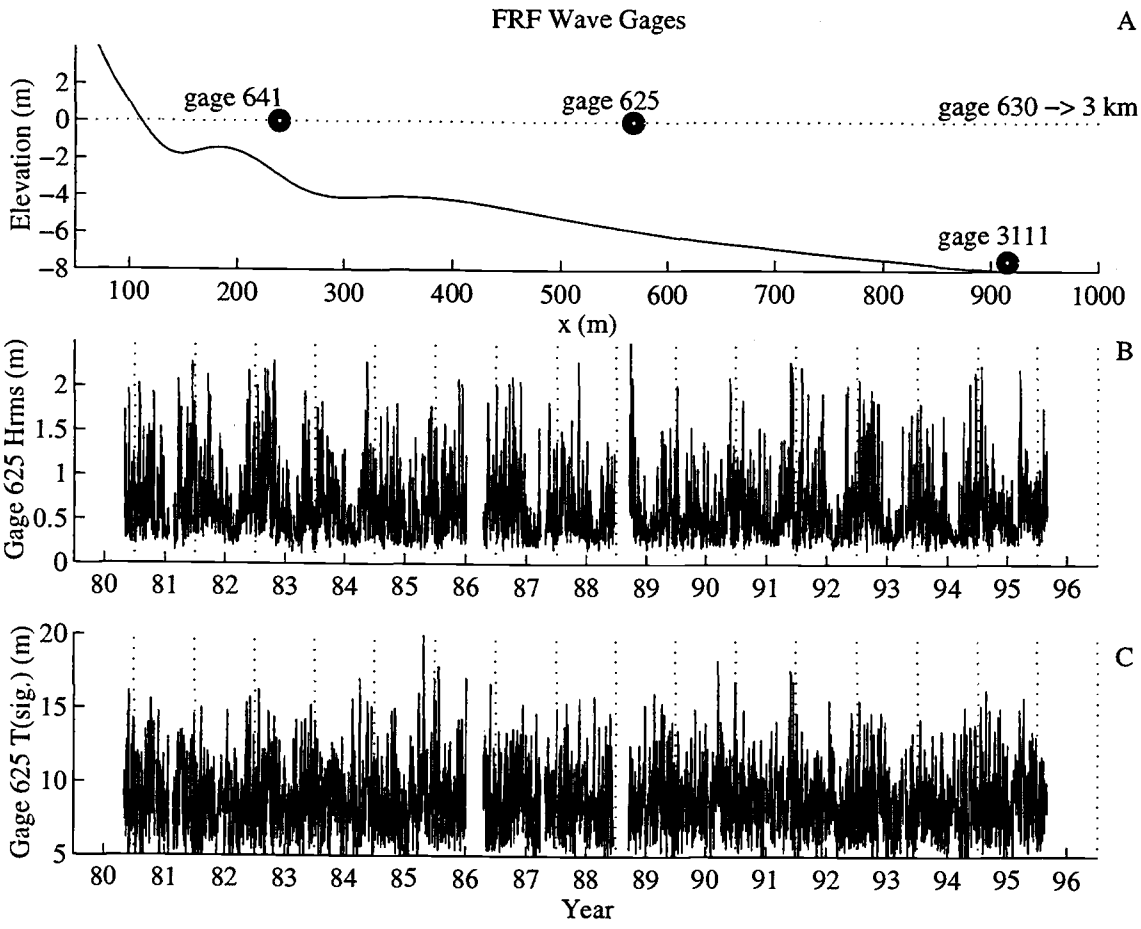

Figure V.6. Wave gage locations (A) and wave height (B) and period (C) time series. The rms wave height and significant period shown were recorded at gage 625.

The simple shoaling model was essential to obtaining estimates of the wave height over inner bars, since breaking over outer bars could be significant. Several tests were performed to verify the model's ability to make accurate predictions. The shoaling model, initialized with observations seaward of a bar, produced accurate estimates of observations at a shallow water gage (gage 641, Figure V.7). Notice that the offshore wave height (gage 3111) exceeded the onshore wave height by a factor of 2 and that the shoaling model produced estimates with nearly a 1:1 correspondence. Estimates of pier-end wave heights (gage 625) tended to under-predict the wave height when the wave height exceeded about 1.5 m. The bathymetry over which the waves were shoaled corresponded to the analysis

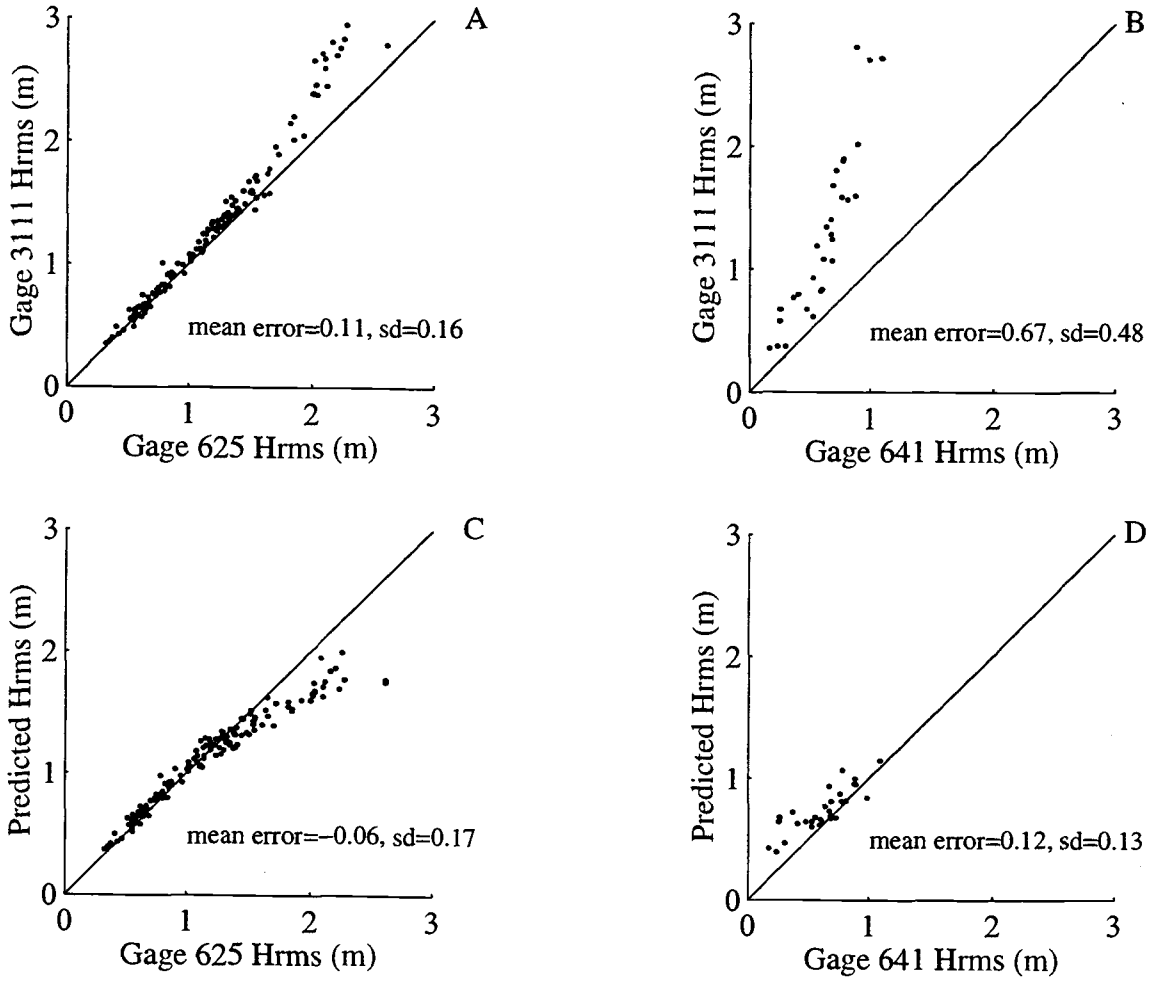

Figure V.7. Comparison of estimated and observed wave heights. In all cases, the wave model was initialized with wave heights measured at gage 3111 (Figure V.6). Alongshore-averaged bathymetry was used in the comparison. Wave heights used in the comparison were measured within a few days of each survey. The top two panels compare the wave height measured at gage 3111 to the heights measured at gage 625 (A) and the height measured in approximately 2 m depth (B, gage 641). The lower panels compare the observations to the wave model predictions.

region used in this study (north of the pier). These bathymetries differed from the bathymetry near the pier, which had a pronounced trough. As a result, it is reasonable to expect that energy losses due to wave breaking were over predicted. As wave angle estimates were not uniformly available, normally incident waves were assumed in all cases.

The sensitivity to this assumption was explored using the shoaling model and a particular profile, which had only one prominent sand bar (Figure V.8). Large waves propagating over this bathymetry resulted in estimated rms wave heights at the bar crest that differed from the maximum height (corresponding to normal incidence) by less than 10%. For the smallest waves typically observed at the FRF, bar crest height estimates differed by less than 10% if the wave angle was less than 45° (0° is shore normal).

Wave height measurements were available for most of the 16-year period from gage 625, located at the end of the FRF pier (Figure V.6). If data from this gage were not available on a particular day, data from a pressure gage in 8 m depth (gage 3111) or from a Waverider buoy located in 17 m depth were selected, preferably from the shoreward most gage. Rms wave height profiles were estimate once per day, using the daily-averaged rms wave height.

The beach profile used to calculate the wave height transformation was a time-averaged version of the modeled bathymetry. The time series of estimated profile model parameters were first low-pass filtered (Hanning filter, width of 60 d) and then linearly interpolated to each day. The profile was then reconstructed from the interpolated parameters. In addition to being an efficient method of time-interpolation, this method preserved the amplitude of migrating bars. An alternate approach, interpolating the elevations at each cross-shore location, is both inefficient and would tend to damp the bar amplitude. For example, if, between surveys, a bar migrated through a distance of one "wavelength", bar and trough elevations cancel and the mean profile might not contain a bar at all.

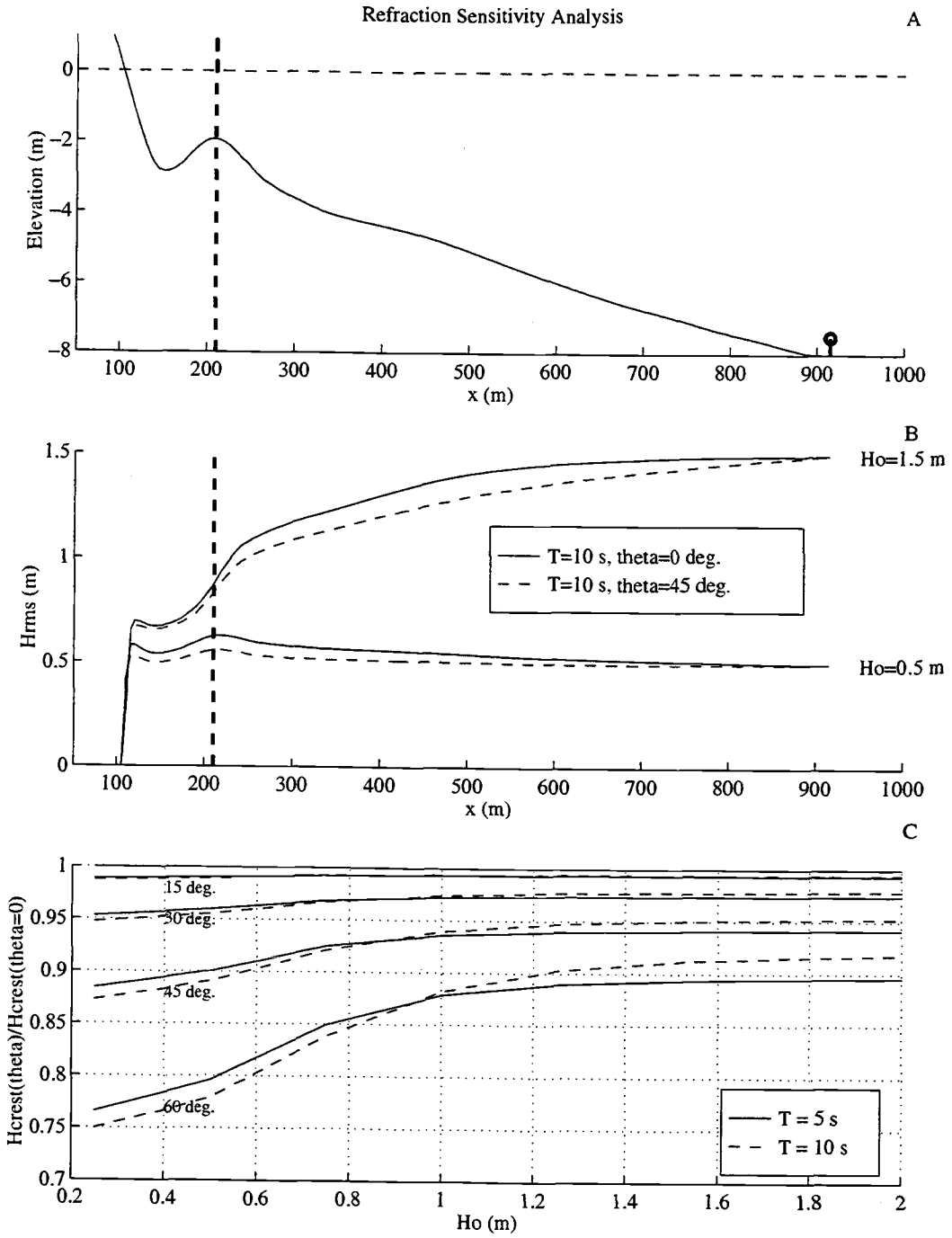

Figure V.8. Sensitivity of wave height estimates to variations in wave angle. The top panel (A) shows the bathymetry over which the sensitivity test was run, the location (bar crest) where wave heights were extracted from the model, and the wave gage location. A cross-shore profile of the modeled rms wave height for two different incidence angles and two different offshore wave heights are shown in the next panel (B). The lower panel (C) shows the ratio of the wave height estimated by including wave refraction to the estimate without refraction. The height estimates including refraction are always lower than the estimate without refraction.

5.2 Sediment transport estimates

Estimates of the mean (between consecutive surveys) values of the profile parameters (b_0, b_1, A_m, X_m, A_s, L_s) were also obtained from the low-passed time series. A backwards difference approximation was used to estimate their rates of change (β_0, β_1, α_m, C_m, α_s, λ). To minimize errors, differences were estimated only between consecutive surveys that were separated by less than 60 d. The cross-shore sediment transport profile was constructed using equation (4), where t_0 corresponded to the time midway between surveys. The transport correlation, magnitude, and phase shift (R_m, B_m, and ϕ_m) were estimated from the transport profile. These statistical measures were estimated over $\pm 2\ L_m$, centered on the mean bar crest position. In the following section, they are compared to the forcing parameter, γ_{crest}.

5.3 Forcing-response relationships

The forcing parameter, γ_{crest}, was estimated along the space-time path corresponding to the filtered and interpolated version of $X_m(t)$. Because the transport profiles were estimated from a low-pass filtered version of the profile response, the time series of γ_{crest} was low-pass filtered (denoted $\gamma_{crest}(t)^*$). R_m, B_m, and ϕ_m were compared to a single value of γ_{crest}, which was the average value between consecutive surveys.

$$\overline{\gamma_{crest}}\,(t_0) = \frac{1}{N} \sum_{t_0+\Delta t/2}^{t=t_0-\Delta t/2} \gamma_{crest}(t)^*, \qquad (10)$$

where Δt is the interval between consecutive surveys and the asterisk denotes the filtered time series. Hereafter, γ_{crest} refers to $\overline{\gamma_{crest}}$.

The relationships between the transport parameters (R_m, B_m, and ϕ_m) and γ_{crest} are presented in Figures 10-13. The analysis was split into 4 different cases, which

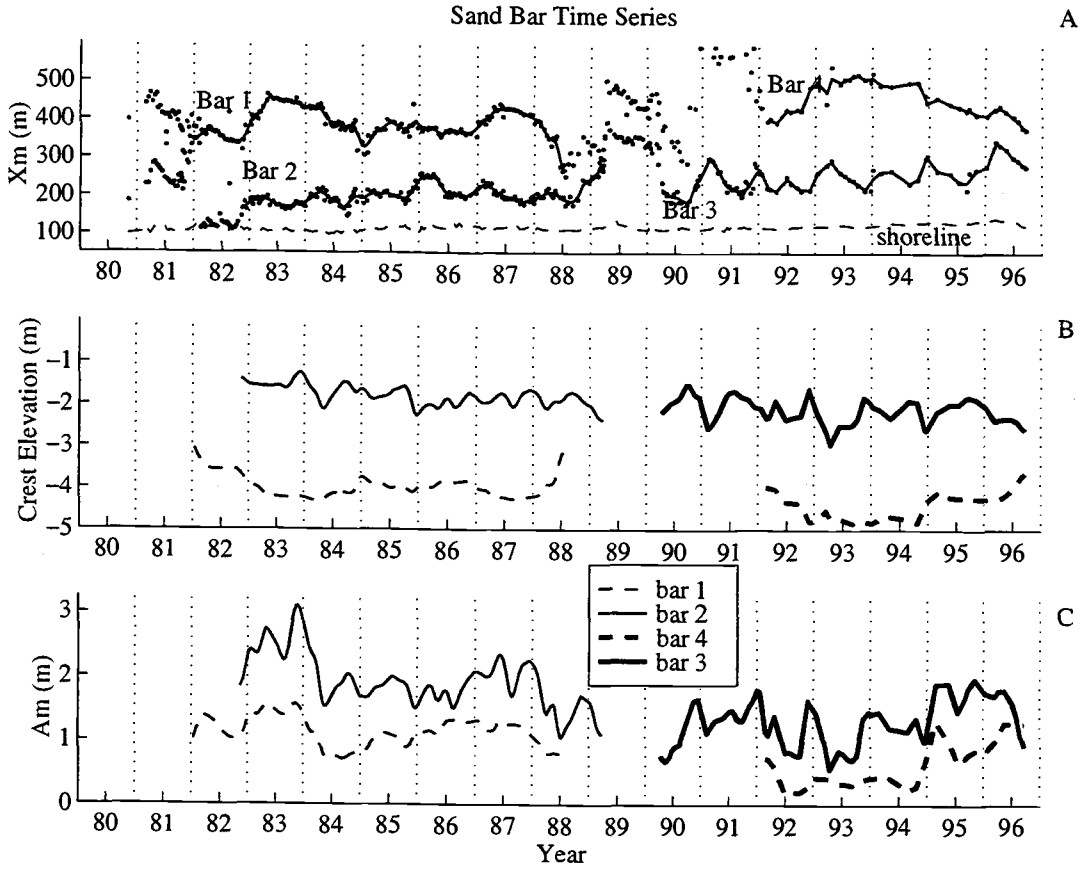

Figure V.9. Time series of bar parameters. The position of all bar crests are marked by dots in the top panel (A), while the bars data used in the analysis are marked by solid lines. Time series of bar crest depths (B) and amplitudes (C) are shown for each bar.

differentiated inner and outer bars (Figure V.9). Figure V.10 presents the results from the analysis of bar 1, an outer bar. High correlation between the estimated transport and the transport predicted for an isolated Gaussian-shaped bar was indicated by R_m near 1. 80% of the observations exceeded 0.5, which corresponded, approximately, to a 95% significance level. Low correlations imply that the spatial scale of the transport patterns differed from the bar scale, resulting in the bar changing shape. The squared correlations were averaged within 6 different ranges (bins) of γ_{crest}, which were chosen to span the observations and have an average of about 30 observations in each bin. There did not appear to be any relationship between R_m and γ_{crest}.

The transport magnitude and phase shift were analyzed using only cases where R_m exceeded 0.5. The transport magnitude, B_m (Figure V.10B), tended to increase with increasing γ_{crest}. The observations at high γ_{crest} suggest a power law relationship, between B_m and γ_{crest}. This relationship was estimated to be $B_m \sim \gamma_{crest}^{2.5\pm0.5}$. These results are somewhat surprising, since they suggest that as long as there is adequate wave energy ($\gamma_{crest}>0$) bars continue to evolve.

The transport phase shift, which describes the ratio of transport associated with migration vs. growth, was bi-modally distributed. One mode was centered, approximately, at $\phi=0$ and the other mode at $\phi = \pi$. At low values of γ_{crest} (non-breaking conditions, $\gamma_{crest} < 0.15$), the phase shift corresponded to onshore migration and bar decay. At somewhat larger values of γ_{crest}, transport patterns resulted predominantly in onshore migration ($0.15 < \gamma_{crest} < 0.17$). For $\gamma_{crest} > 0.17$, the predominant phase shift changed to 0, corresponding to offshore migration. Conditions where $\gamma_{crest} > 0.17$ likely correspond to breaking over the bar, and $\gamma_{crest} = 0.25$ corresponds to saturated breaking at the depths and slopes at the outer bar crest (mean crest depth was about 4 m, mild slopes on the seaward flank of the outer bar).

To assess the reliability of the phase shift dependence on γ_{crest}, mean phase shifts and a measure of phase significance were estimated. The mean phase shifts are shown as open circles (Figure V.10C), and are connected across regions having significant phase estimates. The mean phase shifts within each bin were estimated as

$$\overline{\phi} = \tan^{-1}\{\Sigma\sin[\phi_m]/\Sigma\cos[\phi_m]\}. \qquad (11)$$

The significance of the mean phase was assessed by evaluating the likelihood that the observed phases were sampled from a uniform distribution. The test statistic is the radial distance corresponding to the sum of unit vectors whose orientation is ϕ_m, normalized by

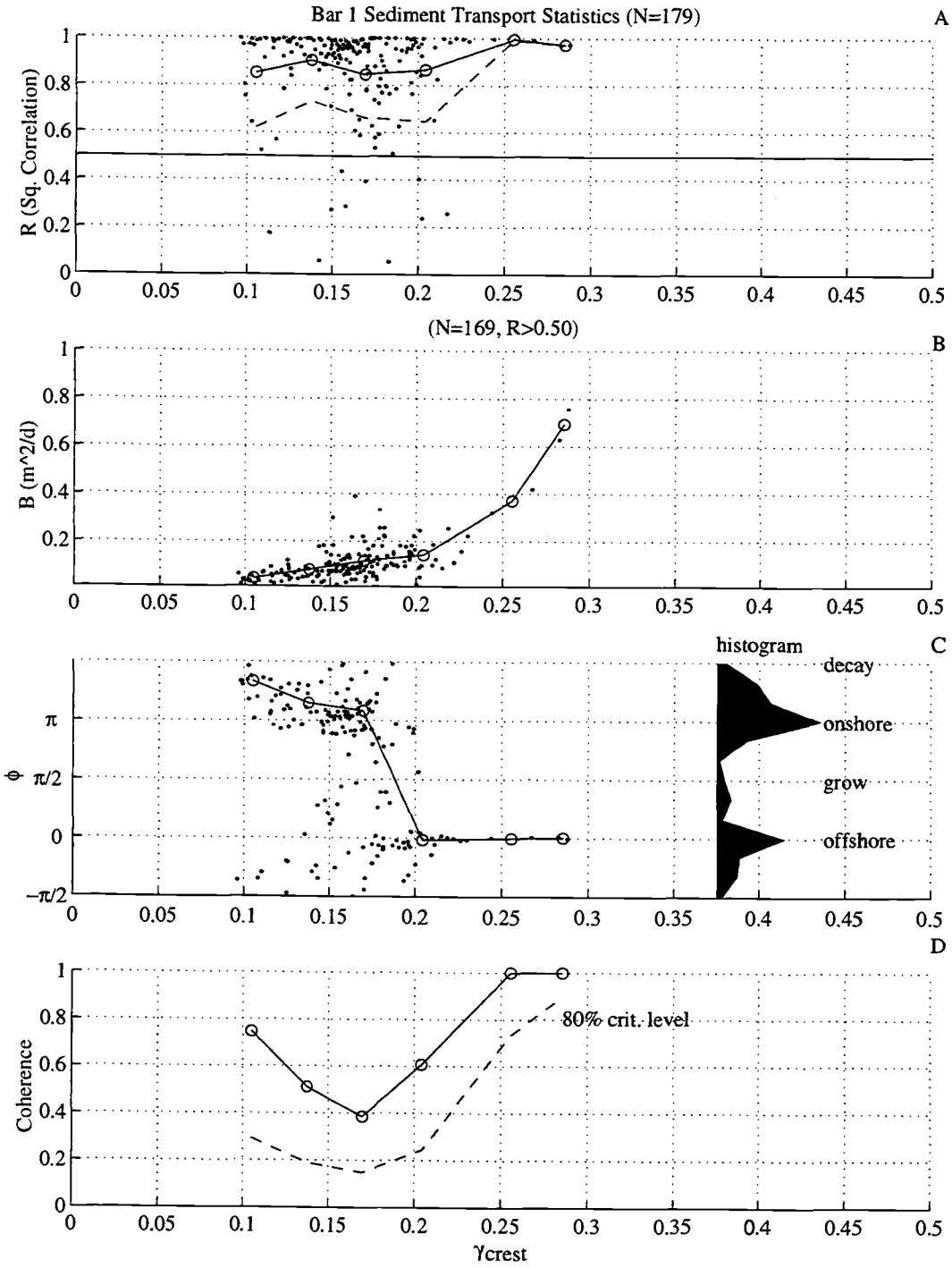

Figure V.10. Sediment transport response vs. γ_{crest}: Bar 1. The top panel (A) shows the correlation between cross-shore transport patterns associated with bar migration or growth and the actual transport. In all panels, the circles denote average values within 6, equally spaced γ_{crest} bins. The dashed line is the mean - 1 standard deviation. The second panel (B) shows the transport magnitude. The third panel (C) shows the sediment transport phase shift estimates, as well as a histogram of the phase shifts. The sense of bar response is labeled in each phase quadrant. The last panel (D) presents the phase "coherence" within each bin.

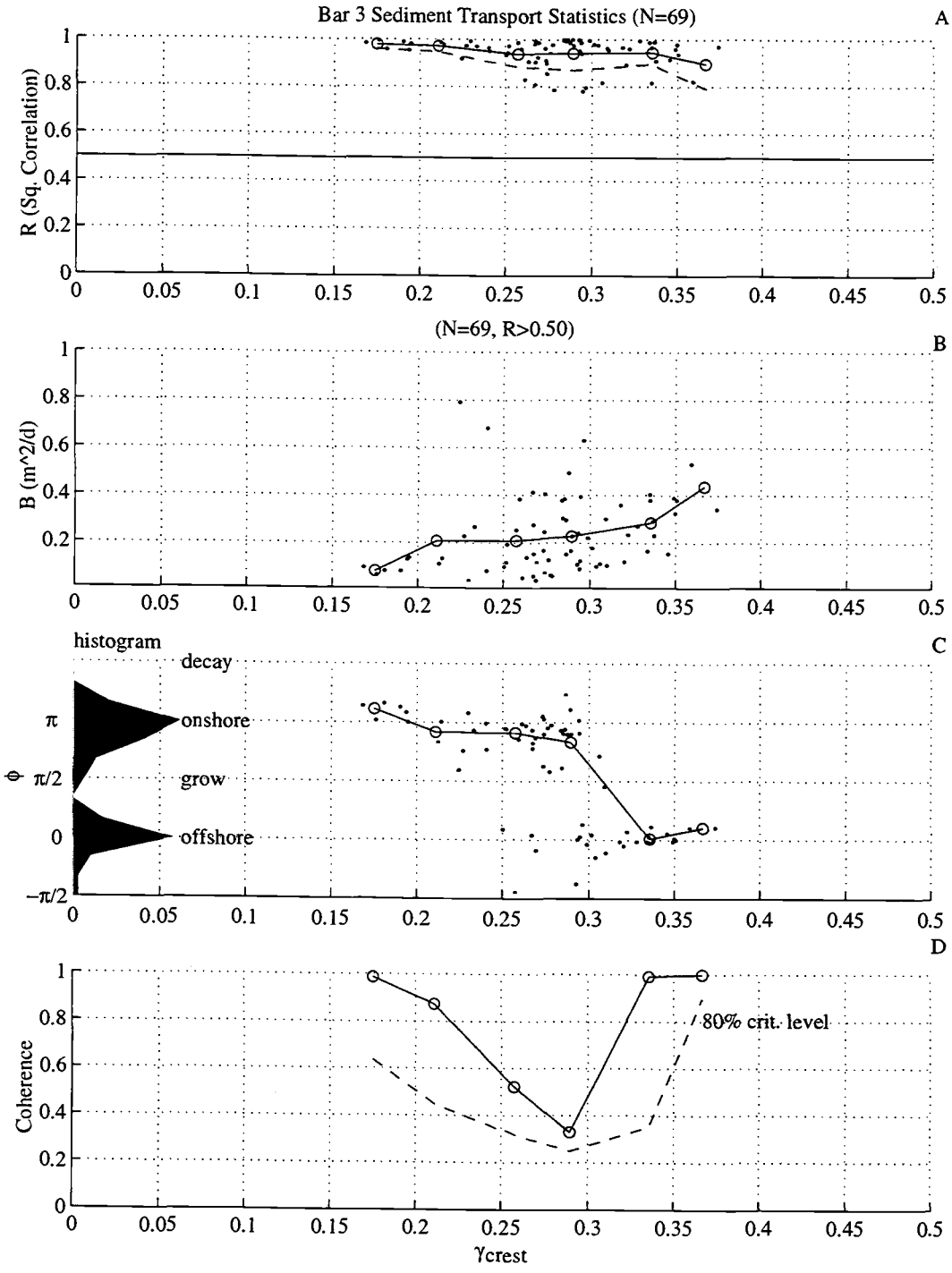

Figure V.11. Same as Figure V.10: Bar 3.

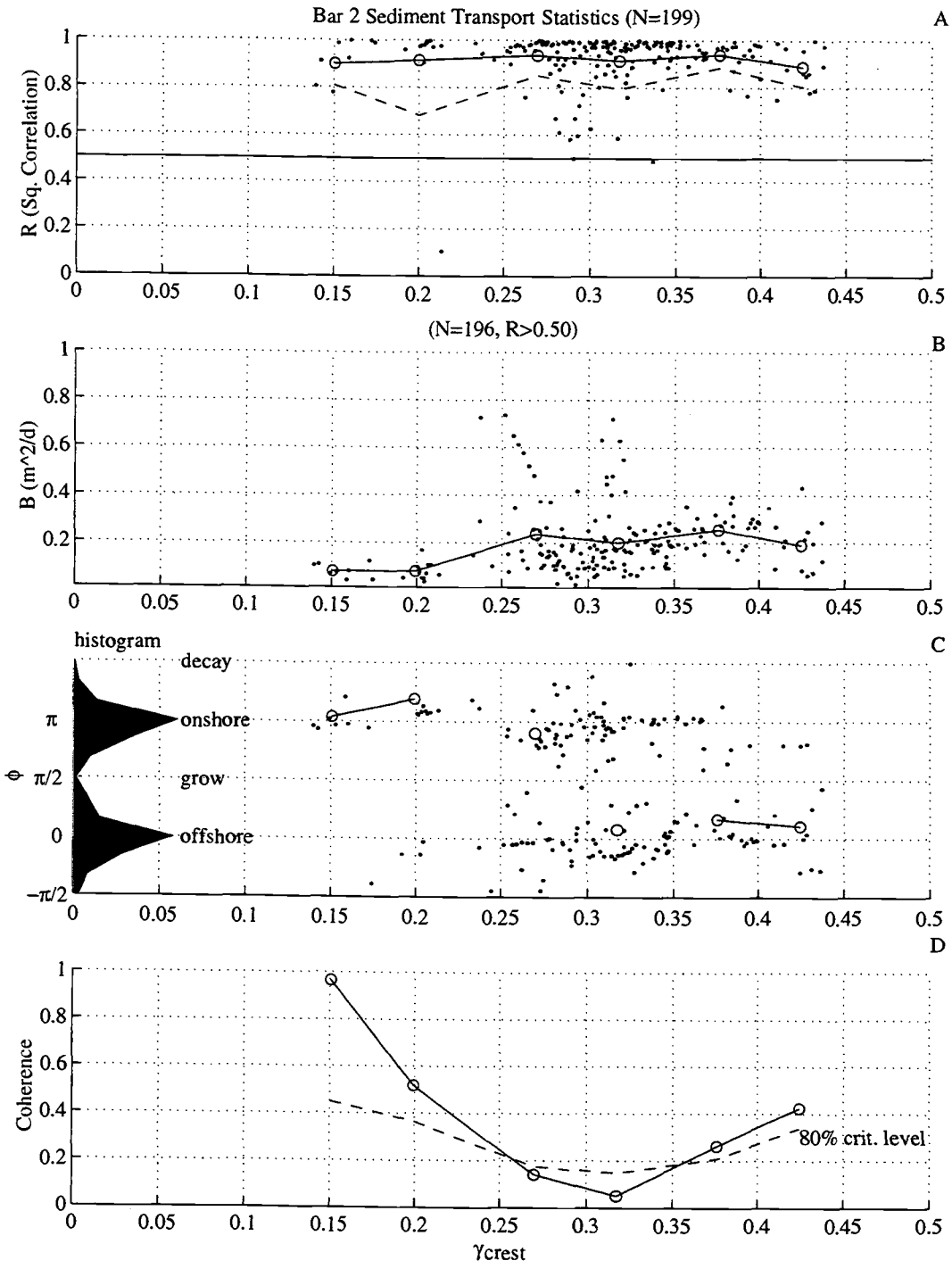

Figure V.12. Same as Figure V.10: Bar 2.

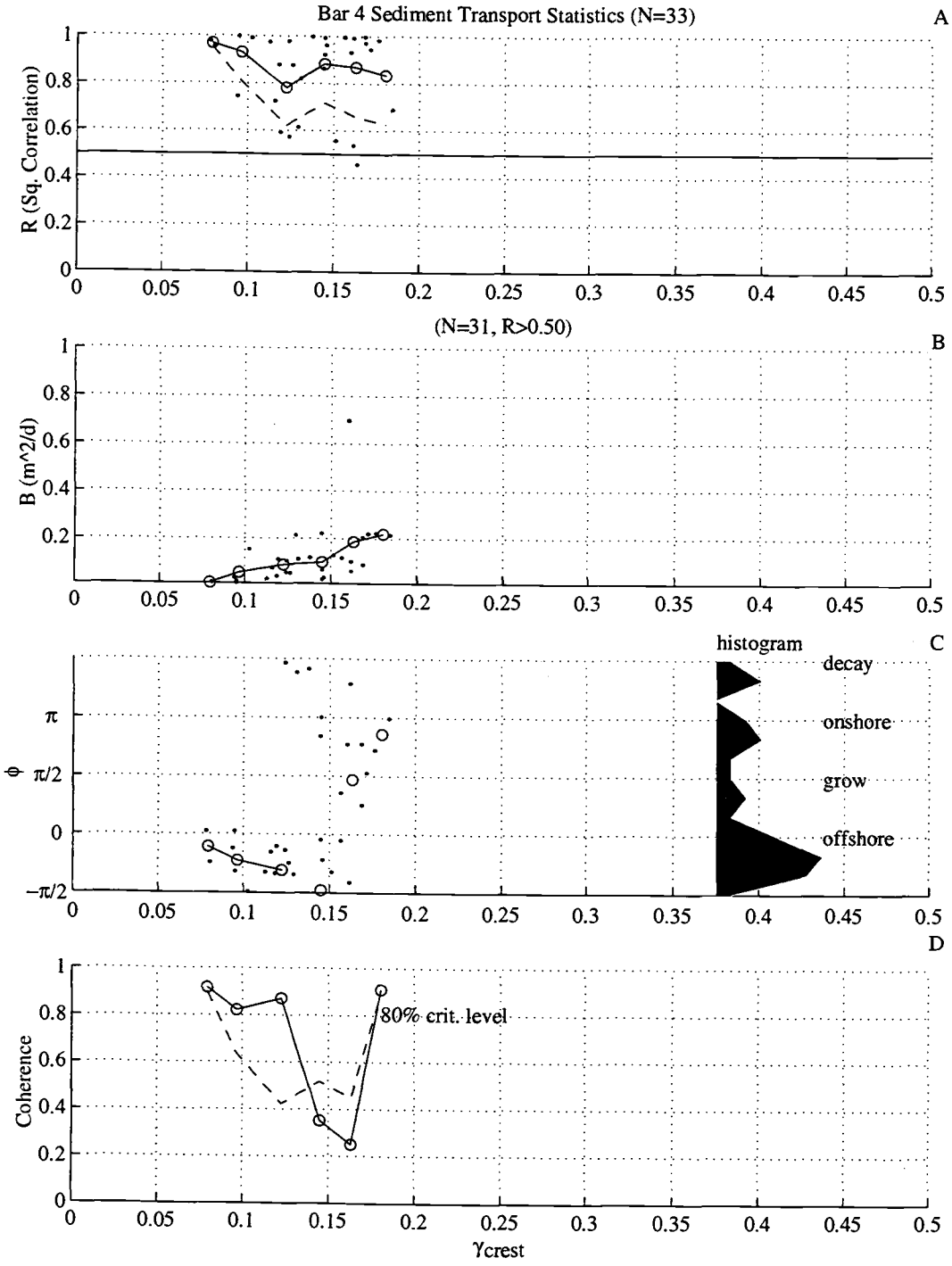

Figure V.13. Same as Figure V.10: Bar 4.

the number of observations

$$r = \{\Sigma(\sin[\phi_m]^2 + \cos[\phi_m]^2)/n\}^{1/2}. \quad (12)$$

In an analogy to estimating the coherence of a phase spectrum, we will refer to r as the coherence of the sediment transport phase shift (Figure V.10D). A critical value of r is

$$r_{crit} = \{\chi^2_2(1-\alpha)/(2\,n)\}^{1/2}, \quad (13)$$

where $\chi^2_2(1-\alpha)$ is the $100(1-\alpha)$ percentage point of the chi-squared distribution with 2 degrees of freedom [*Mardia*, 1978]. If the phases were sampled from a uniform distribution, there is only a 100α percent probability of r exceeding r_{crit}. The 80% significance level is shown, which corresponds to α=0.2. The phase significance was lowest near the transition from onshore to offshore migration.

The analysis of sediment transport parameters was repeated using observations from 3 other bars. Bars 2 and 3 were inner bars and bar 4 was an outer bar. We present the results for bar 3 next (Figure V.11), since they are qualitatively similar to those of bar 1. 94% of the transport correlation estimates exceeded 0.5. The transport correlation tended to decrease as γ_{crest} increased, suggesting that changes in bar shape were associated with dissipative (high γ_{crest}) conditions. The transport magnitude increased as γ_{crest} increased and the phase shift estimates were bi-modal. At low values of γ_{crest}, the phases were near and slightly above π (onshore migration and amplitude decay). As γ_{crest} approached 0.3, the phase shift decreased slightly (onshore migration and growth). The phase shift jumped to 0 (offshore migration) at about γ_{crest}=0.30, and remained near 0 at higher values of γ_{crest}. $\gamma_{crest} > 0.3$ clearly corresponds to wave breaking over bars and $\gamma_{crest} = 0.34$ corresponds to saturated breaking over a typical inner bar (mean depth of about 2 m and relatively steep slopes on the seaward bar flank).

The sediment transport parameters corresponding to bar 2 (inner bar, Figure V.12) were not clearly related to γ_{crest}, compared to the previous two cases. 98% of the transport correlations were above 0.5, but they showed little dependence on γ_{crest}. The transport magnitude increased over the range $\gamma_{crest} < 0.3$ (approximately), but showed no tendency to increase at higher values. The phase shifts were strongly bi-modal $(0,\pi)$, however the values of γ_{crest} corresponding to onshore and offshore migration overlapped considerably. A transition between onshore and offshore migration was suggested between γ_{crest} values of 0.25 and 0.35. Mean phase shift estimates were most significant at low γ_{crest}.

The results corresponding to bar 4 (outer bar, Figure V.13) did not resemble those of the other bars, except for a trend of increasing transport magnitude with increasing γ_{crest}. 80% of the transport correlation estimates exceeded 0.5, and significant phase coherence was associated with offshore migration and decay at low γ_{crest}.

6. Discussion: the role of morphologic feedback

We have demonstrated that, in most cases, the sediment transport patterns causing bar response were consistent with patterns associated with changes in the position or amplitude of Gaussian-shaped bars, having fixed lengths. Bar migration was the most common form of bar response, resulting when bar form and overlying sediment transport were spatially correlated at zero cross-shore lag. The relationship between transport patterns and morphology constitutes a partial description of morphologic feedback. The other part requires a description of the effects of changes in the morphology. This part needs to be interpreted from the relationship of the sediment transport parameters (R_m, B_m, and ϕ_m) to γ_{crest}.

Two simple, and relevant, cases to consider are non-breaking conditions and saturated breaking conditions. Under non-breaking conditions (and constant offshore wave

height), the local rms wave height is a function of local depth (assuming linear wave theory is valid). Changes in γ_{crest} depend only on changes in crest depth. If bar response causes the crest depth to increase (through reduction of the bar amplitude, for instance), γ_{crest} will be driven toward zero. On the other hand, if bar response leads to decreased crest depth (onshore migration with no amplitude change, or amplitude increase), γ_{crest} is driven toward a higher value. Since the observed dependence of the sediment transport magnitude was a monotonic and increasing function of γ_{crest}, the only equilibrium state corresponds to $\gamma_{crest}=0$. This suggests that, under non-breaking conditions, bar response is stable (driven toward equilibrium) only if the crest depth increases. Figure V.14 shows estimates of the change in crest depth as a function of γ_{crest} corresponding to bars 1-3. At low values of γ_{crest}, the crest depth either increased or did not change at all. This suggests that low γ_{crest} conditions are potentially unstable (neutral or positive feedback).

A second, extreme case to consider is that of a saturated surf zone. If the wave height remains saturated, γ_{crest} is approximately constant and bar response has no effect (neutral feedback). On the other hand, if bar response increases the water depth (via offshore migration, for instance) such that the wave height is no longer saturated, γ_{crest} will be driven toward zero (negative feedback). The observations suggest that the negative feedback scenario is possible. In the bar 1 and bar 3 cases (Figure V.14), bar crest depth increased at high values of γ_{crest}. Thus, conditions corresponding to high γ_{crest} are potentially stable.

The crest depth of bar 1 tended to vary little over periods of years (Figure V.9), in spite of significant excursions in its cross-shore location. This suggests neutral morphologic feedback. Outer bars are particularly prone to neutral feedback, since greater crest depths decrease the fractional change in depth that might result from either changes in amplitude or position (Note the following h^{-1} sensitivity: $\frac{\partial \gamma_{crest}}{\partial t} = \frac{1}{h}\{\frac{\partial H}{\partial t} - \gamma_{crest}\frac{\partial h}{\partial t}\}$). As

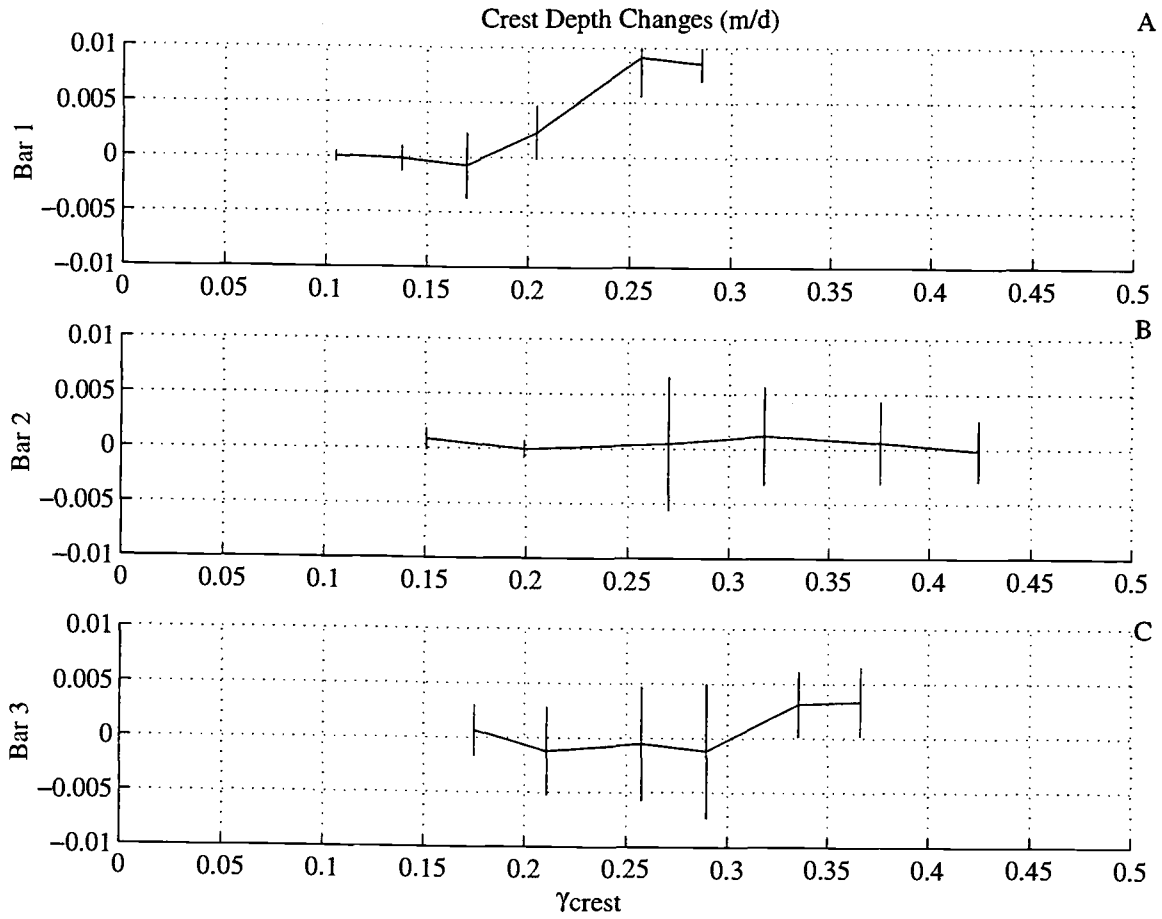

Figure V.14. Bar crest depth changes corresponding to bars 1-3, plotted against γ_{crest}. The depth changes were estimated from a low-pass filtered depth time series.

a result, outer bars may be vulnerable to being trapped in a low γ_{crest} regime, which corresponded to onshore migration and amplitude decay. Neutral feedback may be responsible for the demise of outer bars, which has been associated with decreased occurrence of breaking [*Wijnberg*, 1995].

On the other hand, changes in either wave conditions or bar crest elevation can have significant impacts on γ_{crest} at inner bars, perhaps preventing inner bars from becoming trapped in a low γ_{crest} regime. Additionally, outer bars may prevent inner bars from

becoming trapped by limiting the wave height experienced by inner bars. High values of γ_{crest} (associated with large waves), produced rapid offshore migration in bars 1-3. Offshore migration results in increased water depth. Wave breaking over outer bars decreases the probability of inner bars encountering high values of γ_{crest} and decreases the likelihood of inner bars migrating offshore into a low γ_{crest} regime.

Contrary to most interpretations, the conditions corresponding to a change in the direction of bar migration did not correspond to morphologic equilibrium. Instead, at the transition in migration direction, the bathymetry continued to evolve rapidly through changes in bar amplitude or length scale. The transition in migration direction occurred at fairly sharply defined γ_{crest} values (at least for bars 1 and 3), suggesting that hydrodynamic regimes responsible for onshore and offshore migration were differentiated well by this parameter. The correspondence between the forcing parameterization and bar response was not well defined in the case of bar 2, even though bar migration comprised the dominant form of bar response. A possible explanation for poorly defined transport-γ_{crest} relationship in this case may have been aliasing of high-frequency fluctuations of bar crest positions. As a result, the bathymetry used to estimate γ_{crest} may have differed significantly from the actual bathymetry. Analysis of a bathymetric data set having higher temporal resolution might be able to address this issue.

The relationships between morphology, transport patterns, and coarsely defined hydrodynamic regimes illuminate the sediment transport processes important to observed profile response. Both non-breaking and saturated breaking conditions resulted in bar response that consisted predominantly of bar migration. The associated sediment transport patterns were either negatively correlated (onshore migration) or positively correlated (offshore migration) to the bar form. Onshore bar migration (and sediment transport) under non-breaking conditions is consistent with transport driven by the skewness of orbital

wave velocities [*Wright and Boon*, 1991; *Osborne and Greenwood*, 1992a; *Osborne and Greenwood*, 1992b]. Under these conditions, near bottom velocities (and sediment transport) likely depend inversely on water depth (e.g., $u \sim H_{rms} \sqrt{g/h}$). The transport magnitude increases over bar crests, and decreases offshore and onshore of the crest. Under breaking conditions, it is likely that offshore transport was driven by a strong undertow [*Haines and Sallenger*, 1994; *Thornton, et al.*, 1995], which is predicted to depend inversely on depth [*Stive and Wind*, 1986].

7. Conclusions

Using bathymetric surveys, sampled monthly over a 16 year period at the Army Corps of Engineers' Field Research Facility (US Atlantic Coast), we have characterized surf zone sand bar response to changing wave conditions. Sand bars were described objectively using Gaussian-shaped profiles to identify bar position, amplitude, and length. A model of the commonly double-barred beach profiles consisted of two Gaussian bars, which were added to a planar slope. An additional Gaussian "bar" was added near the shoreline in order to fit the intertidal and subaerial portion of the beach. The profile model, comprised of only 8 parameters, accurately represented the observed, alongshore-averaged bathymetry. The rms error between alongshore-averaged bathymetry and the profile model was 0.10 m (estimated over 322 different surveys), which was small compared to the bathymetric variability associated with sand bars (rms elevation ~ 1 m).

The profile model was used to estimate sediment transport patterns associated with profile response. Transport patterns associated simply with the migration and growth of Gaussian-shaped bars was compared to the total transport in the vicinity of individual sand bars. The correlation between predicted and observed patterns was typically high (squared

correlation > 0.9). Poor correlations resulted when transport patterns over individual bars were influenced by changes in either the plane beach components or adjacent bars.

The magnitude of transport variations over a bar and the ratio of transport associated with bar migration to bar growth or decay were compared to a simple parameterization of nearshore hydrodynamics. This parameter, γ_{crest}, was the ratio of the rms wave height to water depth, estimated at bar crest locations using a simple shoaling model. The transport magnitude was estimated as the standard deviation of the transport in the vicinity of a bar crest. In 3 out of 4 cases, the transport magnitude increased monotonically as γ_{crest} increased. The ratio of transport associated with bar migration vs. bar decay was described in terms of a phase shift between bar form and transport pattern. Estimates of this phase shift were typically bi-modally distributed, corresponding to bar response dominated by onshore and offshore migration. At low values of γ_{crest}, bars migrated onshore and their amplitude tended to decay. At high values of γ_{crest}, bars migrated offshore, with relatively little change in amplitude. The value of γ_{crest} dividing onshore and offshore migration was consistent with the onset of wave breaking.

Because transport patterns were correlated to the bathymetry, and because the nature of this correlation depended on a local measure of the hydrodynamic conditions, morphologic feedback played an important role in governing bar response. However, feedback did not play the commonly assumed role of driving the profile towards an equilibrium state, which requires negative feedback. This statement is made based on the observation that the magnitude of bar response (the sediment transport magnitude) increased monotonically as γ_{crest} increased, in spite of the fact that the direction of bar migration changed. Morphologic equilibrium corresponds to bar response approaching zero, which only occurred at low values of γ_{crest}.

Under non-breaking conditions (low γ_{crest}), bar response either did not affect γ_{crest} (neutral morphologic feedback), or bar response drove γ_{crest} towards higher values. Since increasing γ_{crest} corresponded to increasing sediment transport variations over a bar, this form of response represented positive feedback. On the other hand, breaking conditions (high γ_{crest}) drove bar crests into deeper water, presumably driving γ_{crest} toward lower values (negative feedback).

Outer bars, located in relatively deep water, were potentially trapped in low γ_{crest} regimes due to neutral morphologic feedback. This provides a mechanism for outer bar demise, since low γ_{crest} conditions corresponded to significant bar amplitude decay. Inner bars may avoid being trapped, either because changes in γ_{crest} are more sensitive to changes in bar crest height in shallower water, or because wave breaking on outer bars decreases the likelihood that inner bars experience breaking conditions. Thus, inner bars are prevented from migrating into deeper water where they can become trapped in a low γ_{crest} regime.

CHAPTER VI: THESIS SUMMARY

1. Spatial and temporal scales of morphologic variability

Observations of nearshore morphology have been able to resolve variability having temporal scales ranging from days to decades and spatial scales ranging from several meters to hundreds of kilometers. Most attempts to predict morphologic variability have focused on changes over time scales associated with changes in incident wave conditions. Typically, this corresponds to cycles associated with passing storms (lasting several days) or annual cycles associated with changes in the frequency and intensity of storms. Surprisingly, analyses of long time series of nearshore bathymetry presented in this thesis and in several previous studies demonstrated that interannual variations contribute significantly to nearshore bathymetric variability. The interannual variability can not be explained by models which assume that beach morphology is correlated to changing wave conditions.

Using field observations at the FRF site, this thesis quantified the relative importance of intra-annual (temporal scales equal to or shorter than 1 year) and interannual variability. Analysis of both a 3-year time series of remotely sensed shoreline positions (Chapter 3) and a 16-year time series of conventionally surveyed bathymetry (Chapter 4) indicated that interannual variability dominated. Between the shoreline and 8 m water depths, over 70% of the bathymetric variance was attributed to interannual frequencies.

Temporal variations in nearshore morphology are associated with a range of spatial scales. Temporal variations in characteristic alongshore and cross-shore length scales have been quantified previously by classifying observed morphology within a small number of distinct morphologic states. Changes in morphologic state may be correlated to intra-annual changes in wave conditions. For example, alongshore-uniform morphology is associated

with storm conditions, while shorter scale features such as crescentic bars (O(100) m) and beach cusps (O(10 m) are associated with calm conditions. While changes in the alongshore scale of nearshore morphology can occur rapidly (e.g., within a day), variations in the alongshore-uniform component of the nearshore bathymetry explained greater than 50% of the beach elevation variability at the FRF site (Chapters 3 and 4). This justified an analysis that focused only on the alongshore-uniform component.

Interannual bathymetric variability at the FRF site was associated, in part, with the growth, decay, and cross-shore migration of nearshore sand bars. As a result, alongshore-averaged profile variability could be described with a small number of morphologic parameters. In Chapter 4, bar crest positions were the sole morphologic parameters used in a predictive model of bar migration. In Chapter 5, most of the spatial variability of alongshore-averaged profiles was represented well by a model consisting of Gaussian-shaped bars added to a plane sloping beach. The model provide objective definitions of the position, amplitude, and length of bars. Importantly, the evolution of the profile parameters was related to the cross-shore sediment transport patterns that lead to profile evolution. Resulting descriptions of sediment transport patterns provided insight into the processes driving bar and, in general, profile response.

2. Role of morphologic feedback

Aside from simply serving to describe nearshore morphology, time series of a small number of objectively defined morphologic parameters were used to quantitatively test a several assumed relationships between morphologic change and hydrodynamic conditions. Two assumptions pervade many conceptual and quantitative models used to predict changes in beach morphology. One assumption is that morphologic change depends strongly on the morphology itself. This is morphologic feedback. The other assumption is that this

dependence causes beach morphology to evolve toward a steady state morphology (i.e., equilibrium) under steady offshore wave conditions. This is negative morphologic feedback. An additional, often implicit, assumption is that the morphologic response time is short, relative to the dominant time scale of the forcing, and morphologic changes are correlated to changes in wave conditions.

In Chapter 4, changes in the position of sand bar crests were compared to a model that assumed that bars migrated toward an equilibrium position, which depended on wave height. In addition, the model included a variable response time, which also depended on wave height. The model predicted that bar response would be dominated by time scales longer than those characteristic of the forcing if the bar response time was long compared to the time scale of the forcing. The relationship between observed bar migration rates and wave heights was consistent with the model, suggesting that the negative feedback hypothesis was valid. The predicted equilibrium position was consistent with a break-point location, suggesting that processes associated with wave breaking controlled bar migration. Interannual variability of the bar position likely resulted from the dependence of response time on wave height (wave height cubed), which drove bars that formed near the shore toward the outer extent of the surf zone. The model did not explain or incorporate changes in bar amplitude, which was certainly significant at times of bar formation and decay.

Morphologic equilibrium, as defined in the previous model, corresponded to a steady bar position. Alternatively, morphologic equilibrium could be defined by steady bar position, bar amplitude, and length. The evolution of the profile was adequately described by these parameters, implying that, at morphologic equilibrium, the sediment transport must vanish across the bar. In Chapter 5, observed profile evolution was described by changes in bar position and amplitude, while the bar length was held constant. Changes in bar position and amplitude were used to estimate the sediment transport magnitude across a bar. The

transport magnitude was simply the standard deviation of the spatial variation of transport over a bar length. A transport magnitude of zero corresponds to morphologic equilibrium.

Sediment transport patterns responsible for changes in bar position and amplitude were related to hydrodynamic conditions at bar crests. The ratio of wave height to water depth at the bar crest (γ_{crest}) was used to parameterize the hydrodynamic conditions. A value of γ_{crest} corresponding to the onset of wave breaking divided conditions associated with onshore migration from offshore migration. Bar migration tended to drive γ_{crest} toward the value associated with the onset of wave breaking, consistent with the results of Chapter 4 which suggested an equilibrium bar position corresponding to a "break point". Surprisingly, the sediment transport magnitude did not vanish or even decrease when the bar migration direction changed from onshore to offshore. Instead, the transport magnitude increased monotonically as γ_{crest} increased. Thus, the feedback mechanism associated with the observed bar response differed from the hypothesized mechanism, which was expected to lead to zero transport magnitude.

Changes in bar amplitude played an important role in the feedback mechanism driving outer bar response. Bar amplitude decay was associated with onshore migration and non-breaking conditions. As a result, the crest depth of an outer bar located in relatively deep water changed little and bar response potentially had little affect on γ_{crest}. This implies neutral morphologic feedback governed bar response. Outer bars, unable to change their hydrodynamic regime, could become trapped in non-breaking conditions. This may have been responsible for the demise of outer bars, since non-breaking conditions were associated with amplitude decay. Inner bars did not appear to become "trapped", perhaps a result of a reduced wave height climate due to breaking on outer bars.

3. Implications

Previous attempts to predict nearshore morphologic behavior have used empirical-statistical models which simply describe correlations between measurements of assumed forcing parameters (e.g., wave height, period, etc.) and measured morphologic response. These models have not been used to predict new morphologic behavior because the predicted response is linearly related to the forcing. The model presented in Chapter 4, although not necessarily valid for describing all aspects of profile response, predicted a nonlinear relationship between forcing and response, a result of including a variable response time. This resulted in, for instance, "saw tooth" time series of bar crest positions ("saw tooth" time series of profile elevations were observed, as well). A variable response time is likely to be an important characteristic of all surf zone environments. Interestingly, different beaches could exhibit similar relationships between wave height and response time, yet different wave climates would yield different characteristic response times (e.g., the seasonally averaged response times could differ). The model suggests that the response time is an important descriptive parameter of dynamic morphology, which has not been recognized explicitly in previous attempts to classify beaches and beach response.

If wave conditions, averaged over an annual time scale, are constant then interannual profile variability represents unsteady response to effectively steady forcing. Assuming that the profile is described adequately by a small number of morphologic parameters, the nature of the unsteady interannual response can be characterized in terms of the evolution of the morphologic parameters alone. In particular, for fixed parameterizations of the forcing, the evolution of the morphology at any time will depend only on the current morphologic state. This suggests that future analysis of long bathymetric time series could be used to identify direct relationships between morphologic state and morphologic response, exposing the feedback mechanisms responsible for interannual profile response. An analysis of

interannual morphologic response, where it exists, should answer the unresolved question: Why do some beaches exhibit interannual behavior and others do not?

REFERENCES

Aubrey, D. G., Seasonal patterns of onshore/offshore sediment movement, *Journal of Geophysical Research, 84*, 6347-6354, 1979.

Aubrey, D. G., D. L. Inman and C. D. Winant, The statistical prediction of beach changes in southern California, *Journal of Geophysical Research, 85*, 3264-3276, 1980.

Bagnold, R. A., *The physics of blown sand and desert dunes*, 265 pp., Mathuen, London, 1941.

Bagnold, R. A., Mechanics of marine sedimentation, in *The Sea*, Edited by M. N. Hill, pp. 507-528, Wiley-Interscience, New York, 1963.

Bailard, J. A., An energetics total load sediment transport model for a plane sloping beach, *Journal of Geophysical Research, 86*, 10938-10954, 1981.

Bascom, W., *Waves and beaches*, pp., Anchor Books, Garden City, N.Y., 1954.

Battjes, J. A., Surf similarity, in *Proceedings 14th Int. Conf. Coastal Engineering*, pp. 446-480, ASCE, 1974.

Birkemeier, W. A., Time scales of nearshore profile change, in *Proc.19th International Conference on Coastal Engineering*, pp. 1507-1521, ASCE, New York, 1985.

Birkemeier, W. A. and C. Mason, The CRAB: A unique nearshore surveying vehicle, *Journal of Survey Engineering, 110*, 1-7, 1984.

Bowen, A. J., Simple models of nearshore sedimentation: beach profiles and longshore bars, in *The Coastline of Canada*, pp. 1-11, Geol. Surv. Can., 1980.

Bowen, A. J. and D. A. Huntley, Waves, long waves and nearshore morphology, *Marine Geology, 60*, 1-13, 1984.

Bowen, A. J., D. L. Inman and V. P. Simmons, Wave 'set-down' and 'set-up', *Journal of Geophysical Research, 73*, 2569-2577, 1968.

Dally, W. R., Longshore bar formation - surf beat or undertow?, in *Coastal Sediments '87*, pp. 71-86, ASCE, 1987.

Dean, R. G., Heuristic models of sand transport in the surf zone, in *Conference on Engineering Dynamics in the Surf Zone*, pp. 209-214, ASCE, Sydney, N.S.W., 1973.

Drake, T. G., Shreve, R.L. , Dietrich, W.E. , Whiting, P.J., and L.B. Leopold, Bedload transport of fine gravel observed by motion-picture photography, *Journal of Fluid Mechanics, 192*, 193-217, 1988.

Gallagher, E. L., W. Boyd, S. Elgar, R. T. Guza and B. Woodward, Performance of a sonar altimeter in the nearshore, *Marine Geology, 133*, 241-248, 1996.

Guza, R. T. and E. B. Thornton, Wave set-up on a natural beach, *Journal of Geophysical Research, 86*(C5), 4133-4137, 1981.

Guza, R. T. and E. B. Thornton, Observations of surf beat, *Journal of Geophysical Research, 90*(C2), 3161-3172, 1985.

Haines, J. W. and A. H. Sallenger, Jr., Vertical structure of mean cross-shore currents across a barred surf zone, *Journal of Geophysical Research, 99*(C7), 14,223-14,242, 1994.

Holland, K. T. and R. A. Holman, The statistical distribution of swash maxima on natural beaches, *Journal of Geophysical Research, 98*(C6), 10,271-10,278, 1993.

Holland, K. T., R. A. Holman and A. H. Sallenger, Jr., Estimation of overwash bore velocities using video techniques, in *Coastal Sediments, '91*, Edited by N. C. Kraus, pp. 489-497, ASCE, New York, 1991.

Holland, K. T., B. Raubenheimer, R. T. Guza and R. A. Holman, Runup kinematics on a natural beach, *Journal of Geophysical Research, 100*(C3), 4985-4993, 1995.

Holman, R. A. and A. J. Bowen, Bars, bumps and holes: Models for the generation of complex beach topography, *Journal of Geophysical Research, 87*(C1), 457-468, 1982.

Holman, R. A. and R. T. Guza, Measuring run-up on a natural beach, *Coastal Engineering, 8*, 129-140, 1984.

Holman, R. A., T. C. Lippmann, P. V. O'Neill and K. Hathaway, Video estimation of subaerial beach profiles, *Marine Geology, 97*, 225-231, 1991.

Holman, R. A. and A. H. Sallenger, Jr., Setup and swash on a natural beach, *Journal of Geophysical Research*, *90*(C1), 945-953, 1985.

Holman, R. A. and A. H. Sallenger, Jr., High energy nearshore processes, *EOS Transactions, American Geophysical Union*, *67*(49), 1369-1371, 1986.

Holman, R. A. and A. H. Sallenger, Jr., Sand bar generation: A discussion of the Duck experiment series, *Journal of Coastal Research*, *SI*(15), 76-92, 1993.

Howd, P. A., A. J. Bowen and R. A. Holman, Edge waves in the presence of strong longshore currents, *Journal of Geophysical Research*, *97*(C7), 11,357-11,371, 1992.

Howd, P. A. and R. A. Holman, A simple model of beach foreshore response to long period waves, *Marine Geology*, *78*, 11-22, 1987.

Hulscher, S. J. M. H., De Swart, H.E., and H.J. De Vriend, The generation of offshore tidal sand banks and sand waves, *Continental Shelf Research*, *13*, 1183-1204, 1993.

Hulscher, S. J. M. H., Tidal-induced large-scale regular bed form patterns in a three-dimensional shallow water model, *Journal of Geophysical Research*, *101*, 20,727-20,744, 1996.

Jenkins, G. M. and D. G. Watts, *Spectral analysis and its applications*, 525 pp., Holden-Day, San Francisco, 1969.

Komar, P. D., *Beach Processes and Sedimentation*, 429 pp., Prentice-Hall, Englewood Cliffs, N.J., 1976.

Komar, P. D., *Beach processes and sedimentation*, 2nd ed., 544 pp., Prentice-Hall, New Jersey, 1998.

Komar, P. D. and D. L. Inman, Longshore sand transport on beaches, *Journal of Geophysical Research*, *75*, 5914-27, 1970.

Larson, M. and N. C. Kraus, Dynamics of Longshore bars, in *Proc. 23rd Int. Conf. Coastal Engineering*, pp. 2219-2232, 1992.

Lippmann, T. C. and R. A. Holman, Quantification of sand bar morphology: A video technique based on wave dissipation, *Journal of Geophysical Research*, *94*(C1), 995-1011, 1989.

Lippmann, T. C. and R. A. Holman, The spatial and temporal variability of sand bar morphology, *Journal of Geophysical Research*, *95*(C7), 11,575-11,590, 1990.

Lippmann, T. C., R. A. Holman and K. K. Hathaway, Episodic, non-stationary behavior of a two sand bar system at Duck, NC, USA, *Journal of Coastal Research*, *SI*(15), 49-75, 1993.

Mardia, K. V., Distribution theory for the von Mises-fisher distibution and its application, in *A modern course on statistical distributions in scientific work*, pp. 113-130, D. Reidel, Dordecht, 1975.

McLean, S. R., The stability of ripples and dunes, *Earth-Science Review*, *29*, 131-144, 1990.

Nelson, J. M., The initial instability and finite-amplitude stability of alternate bars straight channels, *Earth-Science Reviews*, *29*, 97-115, 1990.

Ooyama, K. V., Scale-controlled objective analysis, *Monthly Weather Review*, *115*, 2479-2506, 1987.

Osborne, P. D. and B. Greenwood, Frequency dependent cross-shore suspended sediment trasport. 1. A non-barred shoreface, *Marine Geology*, *106*, 1-24, 1992a.

Osborne, P. D. and B. Greenwood, Frequency dependent cross-shore suspended sediment trasport. 2. A barred shoreface, *Marine Geology*, *106*, 25-51, 1992b.

Plant, N. G. and R. A. Holman, Intertidal beach profile estimation using video images, *Marine Geology*, *140*, 1-24, 1997.

Plant, N. G., R. A. Holman and M. H. Freilich, Observations of interannual sandbar behavior at Duck: how relevant is equilibrium thinking?, *Journal of Geophysical Research, in review*,

Raubenheimer, B., R. T. Guza and S. Elgar, Wave transformation across the inner surf zone, *Journal of Geophysical Research*, *101*(C10), 25,589-25,597, 1996.

Roelvink, J. A. and M. J. F. Stive, Bar-generating cross-shore flow mechanisms on a beach, *Journal of Geophysical Research*, *94*(C4), 4785-4800, 1989.

Ruessink, B. G. and A. Kroon, The behavior of a multiple bar system in the nearshore zone of Terschelling, the Netherlands, 1965-1993, *Marine Geology*, *121*, 187-197, 1994.

Sallenger, A. H., Jr. and R. A. Holman, Wave energy saturation on a natural beach of variable slope, *Journal of Geophysical Research*, *90*, 11,939-11,944, 1985.

Sallenger, A. H., Jr. and P. A. Howd, Nearshore bars and the break-point hypothesis, *Coastal Engineering*, *12*, 301-313, 1989.

Sallenger, A. H., Jr. and B. M. Richmond, High-frequency sediment-level oscillations in the swash zone, *Marine Geology*, *60*, 155-164, 1984.

Shepard, F. P., *Submarine Geology*, 338 pp., Harper and Brothers, New York, 1948.

Short, A. D., Three-dimensional beach stage model, *Journal of Geology*, *87*, 553-571, 1975.

Smith, J. D., Stability of a sand bed subjected to a shear flow of low Froude number, *Journal of Geophysical Research*, *75*, 5928-5940, 1970.

Sonu, C. J., Collective movement of sediment in littoral environment, in *Proc. of the11th Int. Conf. Coastal Engineering*, pp. 373-400, ASCE, 1969a.

Sonu, C. J., Collective movement of sediment in the littoral environment, in *Proc. of the 11th Conference of Coastal Engineering*, pp. 373-400, ASCE, 1969b.

Sonu, C. J., Three-dimensional beach changes, *Journal of Geology*, *81*, 42-64, 1973.

Stive, M. J. F. and H. G. Wind, Cross-shore mean flow in the surf zone, *Coastal Engineering*, *10*, 325-340, 1986.

Thevenot, M. M. and N. C. Kraus, Longshore sand waves at Southampton Beach, New York: observation and numerical simulation of their movement, *Marine Geology*, *126*, 249-269, 1995.

Thornton, E. B. and R. T. Guza, Energy saturation and phase speeds measured on a natural beach, *Journal of Geophysical Research*, *87*(C12), 9499-9508, 1982.

Thornton, E. B. and R. T. Guza, Transformation of wave height distribution, *Journal of Geophysical Research*, *88*, 5925-5938, 1983.

Thornton, E. B., R.T. Humiston and W. Birkemeier, Bar/trough generation on a natural beach, *Journal of Geophysical Research*, *101*, 12,097-12,110, 1995.

Trowbridge, J. H., A mechanism for the formation and maintenance of shore-oblique sand ridges on storm-dominated shelves, *Journal of Geophysical Research*, *100*(C8), 16071-16086, 1995.

Wijnberg, K. M., Morphologic behavior of a barred coast over a period of decades, Ph.D. Thesis, 245 pp., Utrecht University, Utrecht, NL, 1995.

Wijnberg, K. M. and R. A. Holman, Shoreward propagating accretionary waves in the nearshore, *Marine Geology*, *in review*,

Wijnberg, K. M. and J. H. J. Terwindt, Extracting decadal morphological behavior from high-resolution, long-term bathymetric surveys along the Holland coast using eigenfunction analysis, *Marine Geology*, *126*, 301-330, 1995.

Winant, C. D., D. L. Inman and C. E. Nordstrom, Description of seasonal beach changes using empirical eigenfunctions, *Journal of Geophysical Research*, *80*(15), 1979-1986, 1975.

Wright, L. D. and J. D. Boon, Kim, S.C. and J.H. List, Modes of cross-shore sediment transport on the shoreface of the Middle Atlantic Bight, *Marine Geology*, *96*, 19-51, 1991.

Wright, L. D., R. T. Guza and A. D. Short, Dynamics of a high-energy dissipative surf zone, *Marine Geology*, *45*, 41-62, 1982.

Wright, L. D. and A. D. Short, Morphodynamic variability of surf zones and beaches: A synthesis, *Marine Geology*, *56*, 93-118, 1984.

Wright, L. D., A. D. Short and M. O. Green, Short-term changes in the morphodynamic states of beaches and surf zones: An empirical predictive model, *Marine Geology*, *62*, 339-364, 1985.

APPENDICES

APPENDIX A. SUB-OPTIMAL INTERPOLATION SCHEME

The optimal interpolation scheme employed the following equations.

$$Z_i^t = \overline{Z_i} + \sum_{j=1}^{J}\{W_{ij}^t (\hat{Z}_j^t - \overline{Z_j})\}, \tag{A1}$$

where $Z_i^t = Z(x_i,y_i,t)$ and $\hat{Z}_j^t = \hat{Z}(x_j,y_j,t)$ denote interpolated and observed elevations. The cross-shore direction corresponds to x, the alongshore direction to y, and time is t. The interpolated elevations were calculated as corrections to a smooth estimate of the time-averaged elevation:

$$\overline{Z_i} = \sum_{j(i)=1}^{J} \sum_{t=1}^{N} \hat{Z}_j^t /(N\,J), \tag{A2}$$

such that $-L_x \le (x_i-x_j) \le L_x$ and $-L_y \le (y_i-y_j) \le L_y$ (L_x=50, L_y=200). Interpolation weights, W_{ij}^t, depended on the distance between the observation and interpolation locations via an assumed Gaussian spatial covariance model

$$W_{ij}^t = \sum_{j'=1}^{J}([\hat{R}_{jj'}^t]^{-1}\, R_{ij'}^t), \tag{A3}$$

where $R_{ij'}^t$ is the spatial covariance between observed elevations and unknown grid elevations, $\hat{R}_{jj'}^t$ is the covariance between observations, and $[]^{-1}$ refers to the matrix inverse. The imposed covariances were

$$\hat{R}_{jj'}^t = \hat{S}_j^2\, \hat{S}_{j'}^2\, C_{ij} - (\varepsilon_j^t)^2\,(1-\delta_{jj'}), \quad \delta_{jj'} = \begin{matrix} 0 \text{ if } j \neq j' \\ 1 \text{ if } j = j' \end{matrix} \tag{A4}$$

and

$$R_{ij'}^t = \hat{S}_i^2\, \hat{S}_{j'}^2\, C_{ij} - (\varepsilon_j^t)^2, \tag{A5}$$

where $\hat{S}_j^2$ is a smooth estimate of the temporal elevation variance

$$\hat{S}_j^2 = \sum_{k(j)=1}^{K} \sum_{t=1}^{N} (\hat{Z}_k^t - \overline{Z_j})^2 /(N\,K), \tag{A6}$$

such that $-L_x \le (x_k-x_j) \le L_x$ and $-L_y \le (y_k-y_j) \le L_y$. The Gaussian form of the covariance function is represented by

$$C_{ij} = \exp[-(x_i-x_{j'})^2/L_x^2 - (y_i-y_{j'})^2/L_y^2], \quad \text{(A7)}$$

which imposes a spatial filter that significantly damps cross-shore length scales < $L_X/2$, and alongshore length scales < $L_y/2$. $(\varepsilon_j^t)^2$ is an estimate of the unresolved component of the observed bathymetric variability, operationally defined as

$$(\varepsilon_j^t)^2 = \sum_{k(j)=1}^{K}(Z_k^t - \hat{Z}_k^t)^2/K, \quad \text{(A8)}$$

such that $-L_x \le (x_k-x_j) \le L_x$ and $-L_y \le (y_k-y_j) \le L_y$. The delta function in (A4) maps the unresolved component of variance to "white noise".

Because matrix inversions were computationally demanding, overlapping subsets of limited sample size (typically, J<300) were used. Also, to alleviate inconsistencies between the true covariance structure and the Gaussian form, the matrix inverse was approximated using singular value decomposition to recover at least 99% of the covariance [*Ooyama*, 1987]. Initially $(\varepsilon_j^t)^2$ was unknown, since it depends on interpolated elevations, and was estimated iteratively. The iterations were initialized with $\varepsilon_j^t(n=1) = 10$ cm were halted after 10 iterations or when $[(\varepsilon_j^t(n)]^2 - [\varepsilon_j^t(n-1)]^2)/\hat{S}_j^2 < 0.1$, where the index n counts the iteration step.

Interpolation errors resulted from measurement error, unresolved morphology (e.g. mega-ripples), and the mismatch between the Gaussian and true covariances. Over a smooth bottom, the vertical accuracy of each elevation observation was about 10 cm [*Birkemeier and Mason*, 1984]. This error estimate does not account for unresolved bed forms, such as mega-ripples (O(1 m) wavelengths and 0(10 cm) amplitudes, e.g. *Gallagher et al.* [1996]). The expected mean square interpolation error was estimated as

$$(E_i^t)^2 = \hat{S}_i^2 - (\varepsilon_i^t)^2 - \sum_{j=1}^{J}(W_{ij}^t R_{ij}). \quad \text{(A9)}$$

This represents the expected rms deviation of the interpolated surface from the smooth version of the actual beach surface. This is the square root of the difference between the total variance of the smooth surface (the first two terms on the right hand side of A9) and the variance actually recovered by the interpolation process (the last term).

APPENDIX B. SIGNIFICANCE OF CORRELATION ESTIMATES

Consider two time series that are uncorrelated. We wish to estimate a critical correlation value, $\rho_{crit}(\alpha, n^*)$, such that probability is α that an estimate of the correlation would exceed this level by chance, due to sampling errors in the sample statistics. This statistic depends on n*, the number of independent samples associated with the estimate. Thus, if a correlation estimate exceeds the critical value, we may reject, with 100 (1-α) percent confidence, the hypothesis that the true correlation is in fact zero. Using knowledge of the distribution of correlation estimates, we can estimate the critical value. In applications to real observations, the number of observations, n, usually exceeds the true degrees of freedom, n*, because observations are serially correlated (i.e., not statistically independent) [*Jenkins and Watts*, 1969, p. 340]. We present a simple scheme for estimating the true degrees of freedom associated with tests for significance of correlation estimates.

Let $\hat{\rho}$ be a sample correlation estimate between time series x_i and y_i:

$$\hat{\rho} = \sum_{i=1}^{n}(x_i - \overline{x})(y_i - \overline{y}) / \{ \sum_{i=1}^{n}(x_i - \overline{x})^2 \sum_{i=1}^{n}(y_i - \overline{y})^2 \}^{1/2}, \qquad \text{(B1)}$$

where n is the number of observations and the over bar indicates an average over n. In the case of zero true correlation between x and y, $\hat{\rho}$ is normally distributed with zero mean and variance of 1/n* [*Jenkins and Watts*, 1969, p. 187]. Thus, we can define the random variable

$$\hat{q} = \{\hat{\rho}^2 n^*\}, \qquad \text{(B2)}$$

which is chi-squared distributed with one degree of freedom (χ_1^2). The critical correlation value can be calculated from the (1-α) percentage point of the chi-squared distribution:

$$\rho_{crit}^2{}_{(\alpha,n^*)} = \chi_1^2(1-\alpha) / n^* \qquad \text{(B3)}$$

Since $\hat{q}$ is chi-squared distributed with one degree of freedom, the mean (expected value: $<\hat{q}>$) is 1. We use this relationship to estimate n* by assuming a constant proportionality factor such that

$$n^* = \nu\, n. \tag{B4}$$

Inserting A4 into A2 yields ν, which can be used to estimate n* required in A3:

$$\nu = 1 / <\hat{\rho}^2\, n>. \tag{B5}$$

In an application to the time-lagged correlation estimate, there are many estimates of $\{\hat{\rho}^2\, n\}$ (one at each lag) so we replace the expectation operator (< >) with the average over 2 M lags (positive and negative lags):

$$\hat{\nu} = 2\, M / \sum_{m=M_{min}}^{M_{max}} \{\hat{\rho}^2(m)\, n(m) + \hat{\rho}^2(-m)\, n(-m)\}. \tag{B5}$$

The limits, M_{min} and M_{max}, are the range of lags ($M = M_{max} - M_{min}$) over which the true correlation ought to be zero. For our purposes, we have chosen (somewhat arbitrarily) $M_{min} = 24$ (lag of 2 years) and $M_{max} = 60$ (lag of 5 years). Note that n(m) is a function of lag. Since we expect that $\hat{\nu} < 1$, n* is set to n (the number of observations) if $\hat{\nu} > 1$. Simulations have shown that this scheme is valid for $\hat{\nu} > 0.1$.